Development of Graphene-based Microelectromechanical Systems for Acoustic Sensing

XU Jing

Doctor of Philosophy

The University of Edinburgh

2021

To my parents

And in memory of my grandparents
and my dogs

Abstract

Graphene has been considered to be a desirable material in the application of semiconductor devices for the next generation due to its outstanding electrical and mechanical properties. In this thesis, the research focuses on the realization of graphene-based acoustic microelectromechanical systems (MEMS). The applications of acoustic MEMS include microphones, hearing aids and ultrasound identification and non-contact testing. Apart from acoustic technology, the graphene-based MEMS designs can be applied in areas for sensing and actuation purpose, such as pressure detectors, micro-drums and ultrasensitive mass sensors. The performance of the devices is determined by the structures of devices, materials properties, dimensions, and the spacing between the membranes and the substrate.

In this project, for the first time, the resonant frequency of graphene-based acoustic sensors has been extended to lower ultrasonic frequency range (20 kHz to 200 kHz). Additionally, a modified dry transfer method with Kapton tape and a novel graphene transfer method with silicon dioxide sacrificial layer have been developed for millimetre-size graphene membranes. To be more specific, three types of devices′ structures, including open cavity, closed cavity and partly open cavity, have been developed, in order to detect the frequency for both audio and ultrasound range (from 11 kHz to 200 kHz). 450 nm polymethyl methacrylate (PMMA) layer has been laminated onto 6-layer graphene to support and form millimetre-size bi-layer membrane. The open cavity resonator for ultrasound sensing has been fabricated with graphene wet transfer process. For closed cavity resonators, a modified dry transfer method with the use of Kapton tape frame has been developed. Using the modified dry transfer method, it is the first time that the millimetre-size graphene/PMMA have been transferred and suspended over the closed cavity. Due to good gas encapsulation of graphene/PMMA closed cavity devices, the vibration of membrane has been prevented due to the air damping when the air gap is decreasing. For the purpose of increasing the capacitance between membrane and substrate and improving the electrical output signal, the air gap should be optimized and decreased. Thus, the partly open structure has been designed for the realization of the graphene/PMMA electrostatic sensors. The graphene/PMMA membrane has been released by etching silicon dioxide sacrificial layer. The air gap of 2 μm of between the millimetre-size graphene-based membrane and the substrate has been achieved for the first time and reported to be minimum among the literature. Furthermore, the dynamic behaviour of the devices have been characterized with laser Doppler Vibrometer (LDV), the confirmation of graphene has been detected by Raman spectroscopy. Finite element analysis has been applied for the simulation of membranes′ dynamic behaviour. The static deformation of graphene after modified dry transfer method has been measured by white light interferometry (WLI). The realization of graphene/PMMA acoustic devices paves the way to the integration of graphene with MEMS to achieve sensors with high sensitivity.

Lay Summary

Acoustic sensors for the frequency of audio range (20 Hz to 20 kHz) and ultrasound range ($>$ 20 kHz) are used to convert a mechanical signal to electrical output. For example, microphones, hearing aids and ultrasound identification are the acoustic sensors which could been found in daily life. In order to improve the performance of devices, integrating new materials with excellent properties to existing technology is interesting for researchers in industry and academia. Since its discovery in 2006, graphene, an allotrope of carbon consisting of a single layer of atoms, has been under intensive research for its outstanding electrical and mechanical properties and is considered to be a desirable material in the application of acoustic sensors.

In this project, three designs of graphene-based acoustic sensors have been illustrated. The designs have been developed for sensing different ranges of frequency. The sensors could be used to measure frequency from 6 kHz to 200 kHz, which covers the audio and ultrasound frequency ranges. The fabrication process and dynamic behaviour of the devices have been illustrated in the thesis. The development of the graphene-based acoustic sensors promises a prospective future for reliable acoustic sensors with advanced performance.

Acknowledgements

I would like to express my gratitude to all the help I have received during my doctoral program. First of all, I would like to thank Professor Rebecca Cheung, for the encouragement, the constructive guidance and immense support. Her passion in research always inspires me during my PhD study. Additionally, I would like to thank Dr Michael Newton for his valuable recommendations, discussion and technical advice on my research. I would like to acknowledge Dr Enrico Mastropaolo of blessed memory, for the design of transistors and technical suggestions on device fabrication.

My genuine gratitude goes to Dr Graham Wood for the instructions on the GMAAT project, the training on the laser Doppler vibrometer (LDV), white light interferometry and the help of FEA (Finite element analysis) simulation probe station. I am grateful Dr Asa'ad Al-masha'al for the guidance and advice on my PhD project I received. I would like to thank Dr Andrew Bunting, Dr Camelia Dunare, and Dr Peter Lomax for their technical advice on device fabrication and the training on the cleanroom equipment. I also would like to thank Mr Richard Blair, Mr Stewart Ramsay, Mr Ewan Macdonald, Mr Kevin Dodds for the technical support, training and help. I am grateful to Dr Andrey Gromov for his assistance in Raman spectroscopy. I would like thank Dr Tony O'Hara from Memsstar Ltd. for developing the oxide etching process. I also acknowledge the help, encouragement and peer pressure from my fellow colleagues and group members, Yulin Geng, Stephen Mbisike, Ammar Bin Che Mahzan, Dr Karina Jeronimo Martinez and Dr Rui Zhang. I would like to thank my officemates, Dr Rui Song, Mingrui Zhao, Aliyu Dala, Amin Rigi, Andrew Mugisha, Stefan Brennsteiner. I would also be grateful to Yuanyuan Hua for the encouragement

and technical help in Cadence. I would like to thank Ashna Gopal for the support and encouragement.

Last but not least, I would like to thank my parents, my grandparents and my dogs for their love.

Declaration

I declare that this thesis was composed by myself, that the work contained herein is my own except where explicitly stated otherwise in the text, and that this work has not been submitted for any other degree or professional qualification except as specified.

XU Jing

Contents

Appendices

Figures and Tables

Figures

Tables

Chapter 1

Introduction

In this chapter, a brief introduction to microelectromechanical systems (MEMS) is given in Section 1.1. The properties of graphene are illustrated briefly in section 1.2. Then the goal and objectives of this research are shown in section 1.3 and the outline of this thesis is provided in section 1.4.

1.1 Introduction to Microelectromechanical systems (MEMS)

The first resonant gate transistor (RGT), as shown in Figure 1.1, has been published in 1967, which is also the first MEMS device [1]. The operating principle of RGT is that as the gate has been actuated by its resonant frequency, the gate capacitance has been changed with the distance between vibrating gate and channel. Thus, the I-V characteristics of the transistor have been shifted by dynamic behaviour of gate electrode. MEMS have integrated the electrical and mechanical elements at the dimensions of micrometres[2–5]. MEMS has been commercialized and produced a wide range of devices, namely, microphones, accelerometers, gyroscopes, pressure sensors, display sensors, switches and biosensors[6–9]. The actuation mechanisms of MEMS sensing include piezoelectric method, capacitive method, electromagnetic method, electro-thermal method. MEMS sensors have been used widely in consumer electronics, industrial manufacture, medical equipment and telecommunication[10].

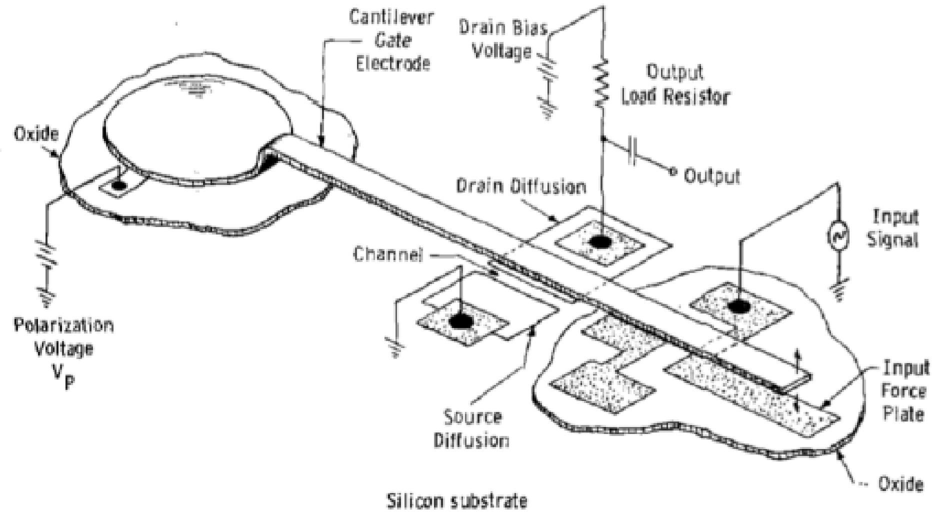

Figure 1.1: The schematic of resonant gate transistor [1]

1.2 Introduction to graphene

Graphene is a two-dimensional sheet of sp^2 hybridized carbon. A single layer of graphene is a hexagonal structure with each atom at the vertex forming 3 covalent bonds with each of its nearest neighbours [11]. The covalent bounds give graphene superior mechanical and thermal properties, like diamond. The fourth valance electron in the $2p_z$ state oriented perpendicular to the planar structure of graphene sheet forms a conducting π band [12]. The π band has been attributed to the remarkable electron properties of graphene. The honeycomb shape on a single layer graphene topography has been observed under scanning tunnelling microscopy (STM) [13], which is shown in Figure 1.2.a. Multilayer graphene and graphite are formed by the stack of graphene layers due to van der Waals forces and the image of five layers thick graphene measured under STM is illustrates in Figure 1.2.b. The asymmetry observed in the Figure 1.2.b suggests the A-B stacking in multilayer graphene [13, 14].

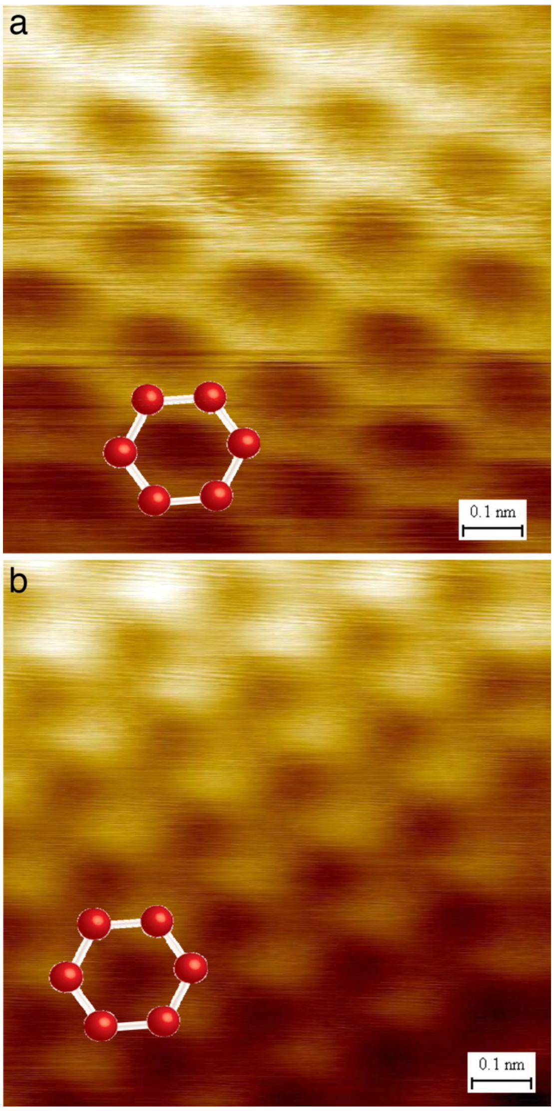

Figure 1.2: STM topographic image of single layer (a) and five-layer thick (b) of graphene [13]

1.2.1 Mechanical properties of graphene

As mentioned above, the covalent bonds play an important role in the mechanical properties of graphene. The strongest $C-C$ chemical bond has been reported to be in sp^2 carbon [15]. The three-fold $C-C$ chemical bond in graphene indicates the excellent mechanical properties [12], including the superior intrinsic mechanical strength (∼130 GPa) [16], the remarkable Young's Modulus (∼1 TPa) [17] and the ultra-low mass density (∼2200 kg/m^3) [18]. The outstanding mechanical properties of graphene hold the promise of acoustic applications and flexible electronics with good performance.

1.2.2 Thermal properties of graphene

Like other carbon allotropes, graphene has remarkable thermal properties [12]. The thermal conductivity has been measured to be between 2000 to 5300 W/mk, which has been the largest thermal conductivity detected so far [19, 20]. In addition, a negative coefficient of thermal expansion (TCE) of around $-7 \times 10^{-6}/K$ has been measured in graphene [19, 21], which means graphene layer shrinks as the temperature increases. The unique TCE has been applied to tuning the resonant frequency upshift of graphene resonators by electro-thermal actuation [22]. The thermal properties of graphene show the potential of electro-thermal applications.

1.2.3 Electrical properties of graphene

The lattice of graphene is described as two interspersed triangular sub-lattices, named A and B, as shown in Figure 1.3, which is firstly used to calculate the band structure of mono-layer graphene in [24]. Using a simple nearest neighbouring tight-binding approach considering a single π electron per atom [23, 25, 26], the band structure of mono-layer graphene has been calculated by[12]

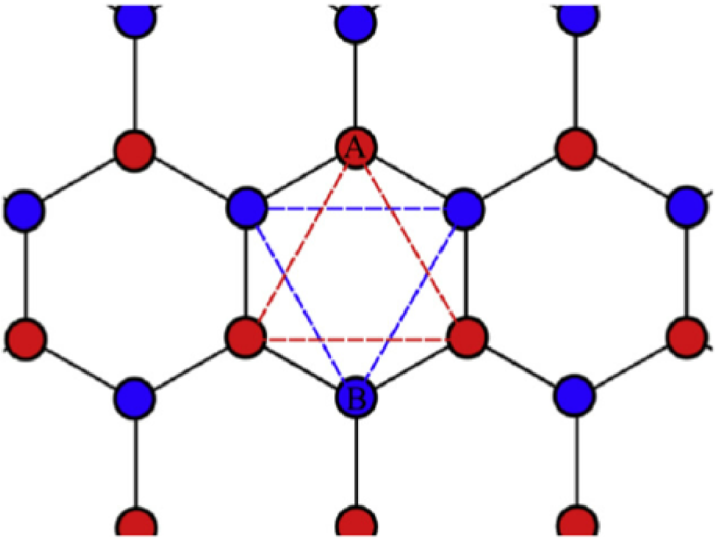

Figure 1.3: Sub-lattice description of graphene. Each atom on the A sub-lattice is surrounded by three B sub-lattice atoms and vice-versa. [12]

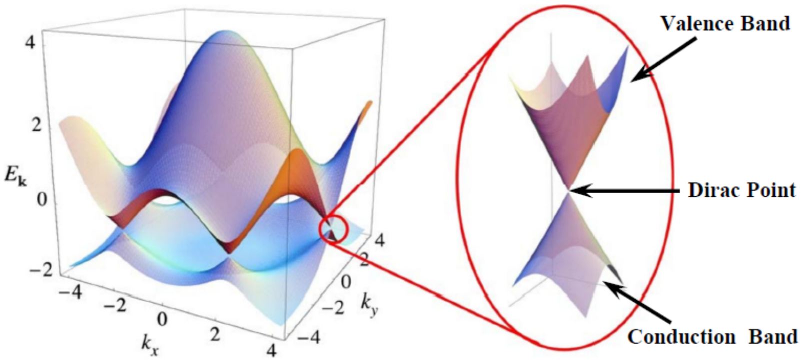

Figure 1.4: Left:Band structure of graphene showing the conductance and valence bands meeting at the Dirac points. Right: zoom-in of the energy bands close to the Dirac points. [23]

$$E^{\pm}(k_x, k_y) = \pm\gamma_0\sqrt{1 + 4\cos\frac{\sqrt{3k_x a}}{2}\cos\frac{k_y a}{2} + 4\cos^2\frac{k_y a}{2}}, \tag{1.1}$$

where $a = \sqrt{3}a_{c-c}$, a_{c-c} denoted by the distance of two atoms in the hexagonal graphene lattice, γ_0 refers to the nearest neighbour overlap integral.

The band structure calculated by the equation (1.1) is shown in Figure 1.4, In the Dirac points, which are defined by where the conduction and valence bands meet, each carbon atom in intrinsic graphene contributes one electron filling the valence band and empty the conduction band. Thus, graphene is called as a zero-gap semiconductor. The unique band structure of graphene results in the remarkably high intrinsic charge mobility up to 250,000 cm^2/Vs [19].

1.2.4 Biocompatibility of graphene

The cytotoxicity of graphene-based material differs in the dimension, number of layers, carbon-to-oxygen ratio atomic ratio and functionalisation degree[27]. After exposure to graphene-based materials, the decrease or slight decrease of bacterial and mammalian cell viability has been reported in 2013[28]. However, the effect of the particle dimension on the cell viability were lacking. In another study, hemolysis in red blood cells caused by pristine and functionalised graphene has been reported to be negligible [29]. Additionally, more studies have shown that the chemical vapor deposition (CVD) graphene on copper foils has been used as substrates for neuronal and other mammalian cells with no cytotoxic effects[30, 31]. Recently, using a non-animal test, graphene-based materials prepared with non-irritant exfoliations agents have been reported not to induce skin irritation, which suggests the safety of applying graphene-based materials in direct skin contact[32]. The cytotoxicity of graphene-based materials should be investigated dependent on the different biomedical applications.

In a word, the biocompatibility of graphene-based materials should be categories according to their physico-chemical characteristics instead of a single type of materials. The biocompatibility has been demonstrated to be improved after surface modification both performed *in vitro* and *in vivo* [33]. More research on the biocompatibility of graphene-based materials would eventually develop safer graphene-based biomedical applications.

1.3 Literature Review

1.3.1 Acoustic MEMS sensors

Acoustic application plays an important role in MEMS sensor, which includes sensing the frequencies of infrasound (0 - 20 Hz), sound (20 Hz – 20 kHz) and ultrasound (higher than 20 kHz). The infrasound sensors can be used to detect earthquakes, volcanos or meteorites [34–36]. For audio sensing, MEMS sensor has been applied to microphones [37–39], speakers[40, 41] and hearing aid [42]. The ultrasound detection can be applied to non-destructive testing[43] or medical imaging[44]. The resonant frequency of mechanical components, such as membrane, plates or cantilever, can be used for the detection of the target frequency. The resonant frequency has been determined by the material properties, structure of sensors and the dimensions of the resonant components. By changing the resonant frequencies of mechanical components, the target frequencies of MEMS acoustic sensors can be set to cover the acoustic frequencies from infrasound to ultrasound.

Additionally, acoustic MEMS sensors have been designed in various structures, based on different mechanisms including capacitive, piezoelectric, optical methods. To be more specific, the different designs of MEMS microphones have been shown in Figure 1.5. Capacitive structure with movable membrane or plate and a back-plate electrode has been shown in Figure 1.5.a [45]. Additionally, using planar interdigitated electrodes to replace back-plate (Figure 1.5.b) has been used to minimize air damping [46], which is an improvement of capacitive design. A bio-inspired piezoelectric microphone has been shown in Figure 1.5.c [47], as piezoelectric MEMS acoustic sensor with less power consumption compared to capacitive design. A hybrid design of capacitive and piezoelectric structure has been illustrated in Figure 1.5.d, in order to enhance the acoustic electrical response [48]. Optical MEMS microphone has been designed, which is based on the Fabry-Pérot cavity formed by fibre tip and cantilever (Figure 1.5.e) [49]. As the cantilever has been actuated by acoustic waves, the white light interferometry detects the vibration and transfers the vibration into electrical signals. The comparison of different MEMS acoustic sensors has been shown in Table 1 [10]. Capacitive structures have been selected and used in this research due to its high sensitivity, high signal to noise ratio and low noise level [10].

Capacitive MEMS microphones

The basic structure of capacitive MEMS microphone includes a flexible diaphragm and a perforated back plate, as shown in Figure 1.6. The flexible diaphragms for conventional MEMS microphones have been reported to be fabricated by silicon nitride with metal layer [50], silicon nitride with polysilicon [51], and polysilicon [38]. The diaphragm has been actuated by the applied sound pressure and the parallel-plate capacitance between the diaphragm and the back plate has been changed. Thus, the acoustic waves have been converted into electrical signal [52]. The frequency response of a MEMS microphone has been shown in Figure 1.7 [53].In order to decrease in-band noise and distortion in the MEMS microphone, the resonance of the diaphragm, has been shifted above the audio band by modifying the size of the diaphragm [54].

The use of acoustic MEMS sensors has been growing as the rapid development of the fifth-generation cellular network technology (5G), virtual reality (VR) technology and augmented reality (AR) technology [10]. To develop MEMS acoustic sensors with better performance and characteristics, the integration of conventional MEMS acoustic sensors and two-dimensional materials has raised interest from the research and industrial community.

Table 1.1: The comparison of different types of MEMS acoustic sensors

MEMS acoustic sensor types	Advantages	Disadvantages
Capacitive	High sensitivity; High signal-to-noise ratio; Low noise level	Sensitive to environment disturbances; Bias voltage required
Piezoelectric	High acoustic overload; Low power consumption; High reliability	High noise level; Low sensitivity
Optical	High sensitivity; Wide dynamic range; Immune to electromagnetic interference	External light source; Fabrication and packaging difficulties

1.3.2 Preparation and transfer method of graphene

Several methods to fabricate graphene have been developed so far. Mechanical exfoliation of graphene from graphite is the first illustrated method for graphene fabrication [56]. The 3 nm thick mechanical exfoliated graphene flake on oxidized silicon wafer has been shown in Figure1.8.a. The exfoliated graphene films are in

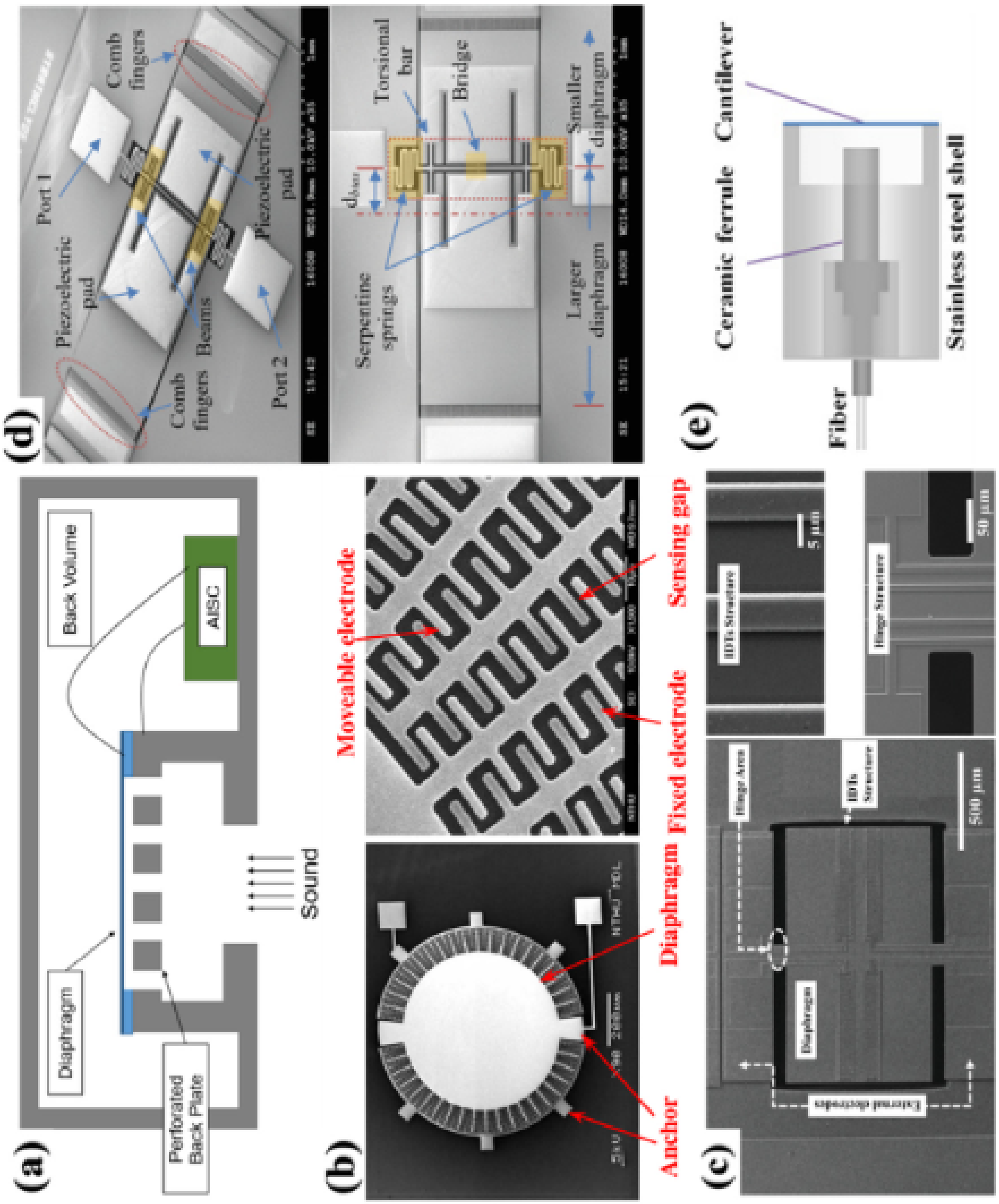

Figure 1.5: The schematic of different acoustic MEMS microphone designs: (a) capacitive MEMS microphone; (b) A no-back-plate capacitive microphone with interdigitated electrodes (IDT) structure; (c) Bio-inspired piezoelectric microphone; (d) Hybrid-mode microphone with piezoelectric and capacitive mechanism; (e)optical microphone [10]

.

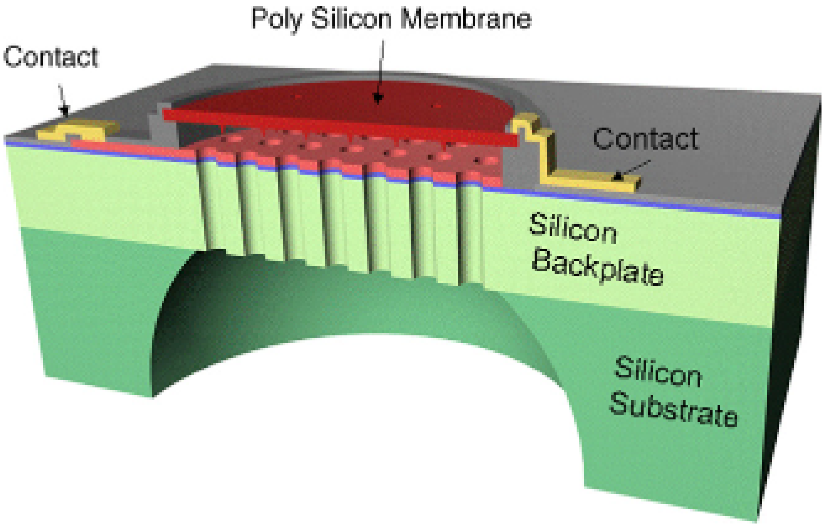

Figure 1.6: Cross-sectional view of a MEMS microphone[55]

small size, with inconsistent shape and thickness [57]. Therefore, the mechanical exfoliation of graphene is not suitable for large scale graphene production. Additionally, an epitaxial growth of graphene is reported in [58] and results from the reduction of silicon carbide (SiC) in the high temperature. The Scanning tunneling microscope (STM) image of monolayer and bilayer graphene has been shown in Figure 1.8.b [58], Alternatively, the graphene films are developed by chemical vapour deposition (CVD) synthesis of graphene on transition metal [59]. In CVD graphene(as shown in figure 1.8.c[59]), carbon precursor gas decomposes on catalyst metal, like Ni or Cu, under high temperature and low pressure [59–61].

The transfer method differs depending on the fabrication techniques of graphene. For the mechanical exfoliation method, as shown in Figure 1.9.a, the graphene flakes on the Scotch tape are rubbed on the substrate [56,62]. In the case of epitaxially grown graphene (Figure 1.9.b), mechanical support layer, like polyimide (PI) or thermal release tape is attached on the graphene/SiC. Then the graphene film with support layer is peeled off from the SiC substrate and is transferred on the target substrate. However, the transferred epitaxial graphene films are reported with defects [63–65]. As depicted in Figure 1.9.c, in the case of CVD graphene, polymer mechanical supporting layer, like Polydimethylsiloxane(PDMS) or Poly

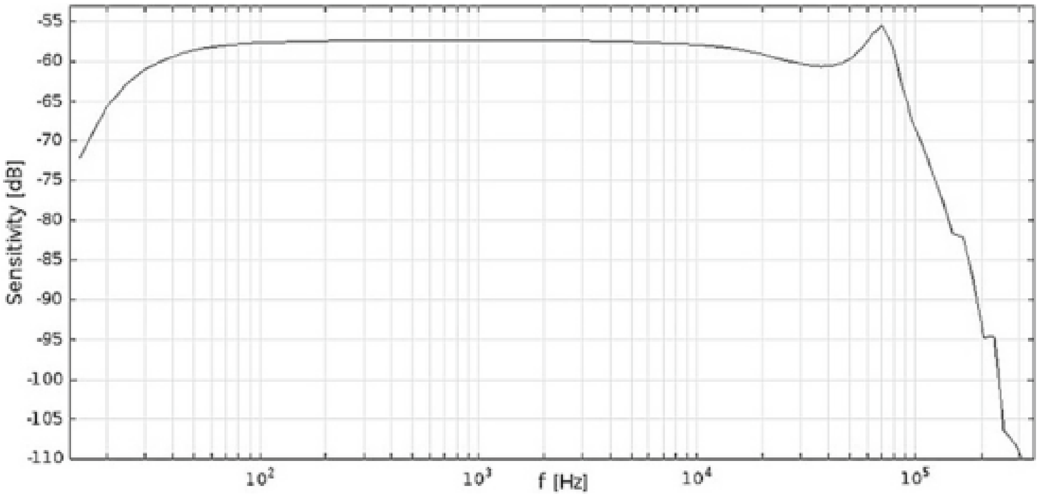

Figure 1.7: The frequency response of a MEMS microphone[53]

(methyl methacrylate)(PMMA), is attached on the graphene/ catalyst mental and graphene with supporting layer is released after the metal is etched [62, 66, 67]. Transfer methods based on CVD graphene, which have been studied and illustrated by researchers are with high percentage yield and repeatability [60,62,66,67]. Therefore, CVD graphene has been used in this research.

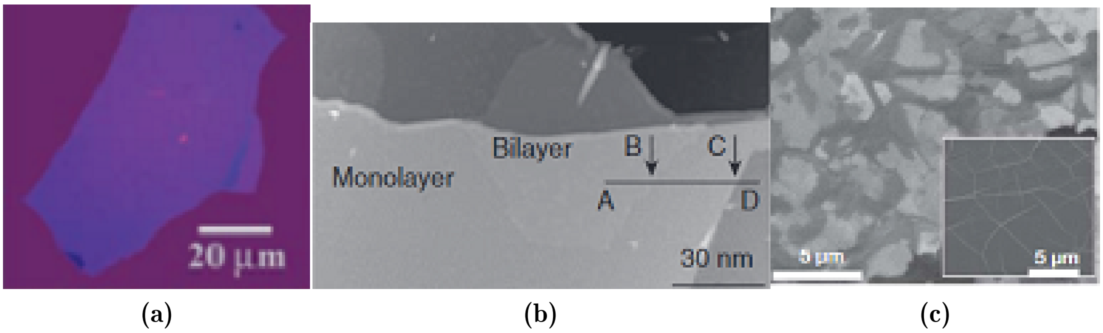

Figure 1.8: The preparation of graphene: (a) optical image of mechanically exfoliated multilayer graphene flake on oxidized silicon wafer fabrication [56]; (b) STM image of epitaxial single-layer and bilayer graphene on 6H-SiC(0001) [58]; (c) SEM image of graphene films on thin (300 nm) nickel layers and thick (1 mm) nickel foils(inset) [59]

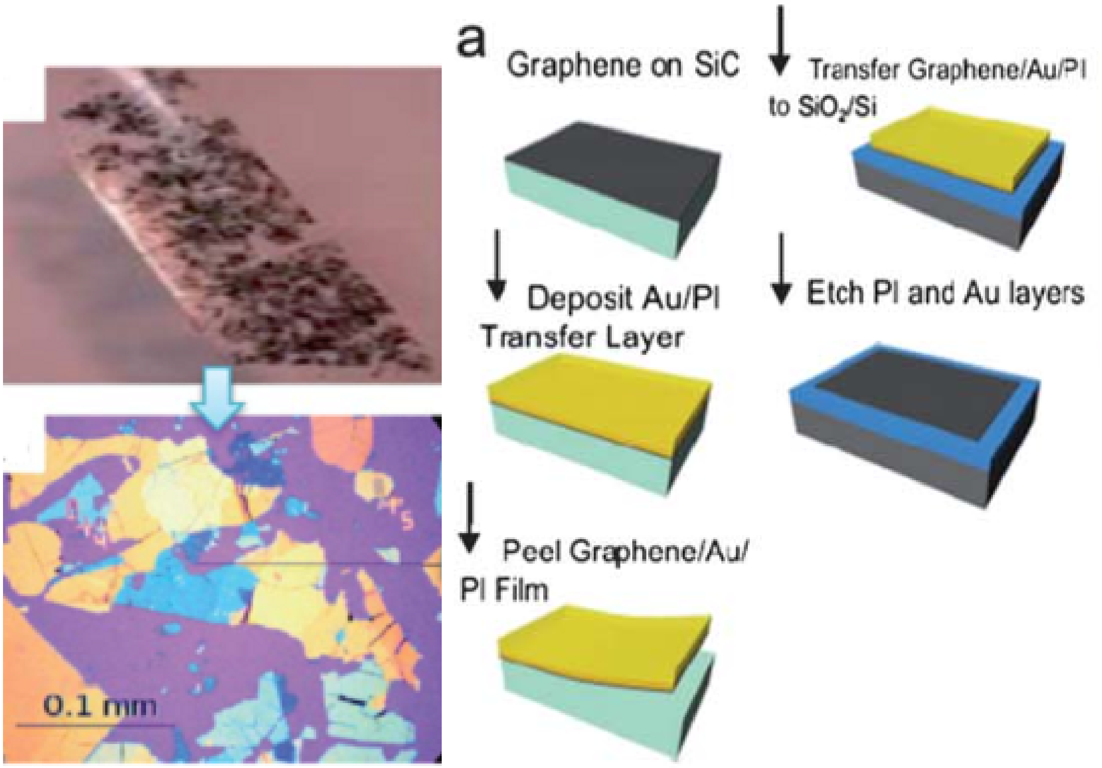

(a) (b)

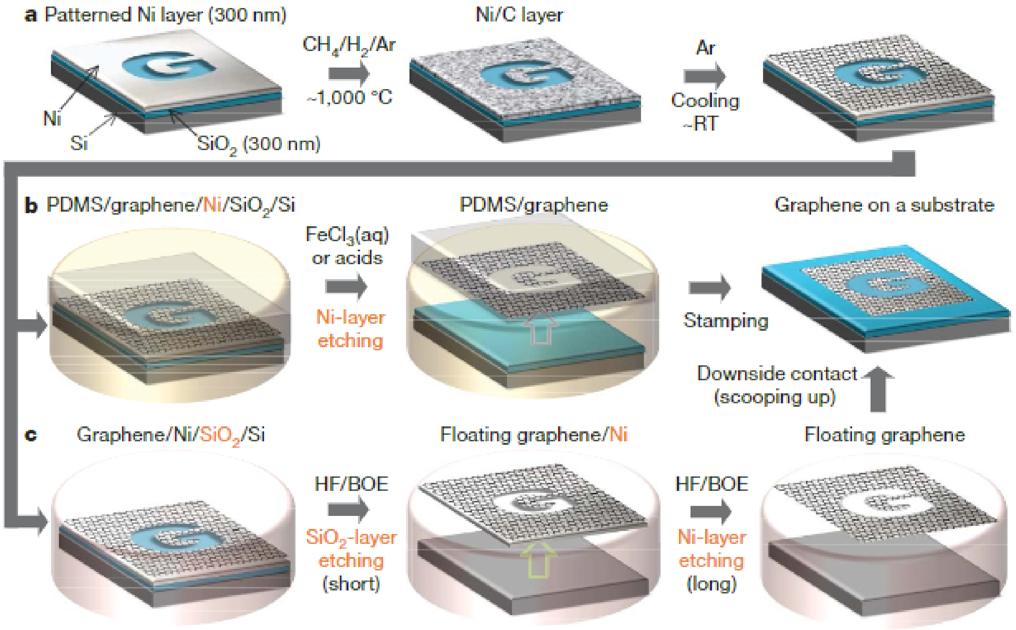

(c)

Figure 1.9: The preparation of graphene: (a) optical image of mechanically exploited multilayer graphene flake on oxidized silicon wafer fabrication [56]; (b) STM image of epitaxial single-layer and bilayer graphene on 6H-SiC(0001) [58]; (c) SEM image of graphene films on thin (300 nm) nickel layers and thick (1 mm) nickel foils(inset) [59]

1.4 Research aim

The aim of this research is to develop millimetre-sized graphene-based transducers for acoustic sensing. The transfer methods of graphene-based membrane have been modified and developed in order to transfer ultra-large size of graphene-based membranes (the aspect ratio of the membrane's diameter to thickness between 1100 and 7800) onto the substrates to form the devices. The target resonant frequencies of the devices have been designed to be audio frequency range (20 Hz to 20 kHz) and lower ultrasound frequency range (lower than 200 kHz). Design, fabrication and characterisation of the acoustic graphene-based transducers have been included in the research. The sensors for audio range can be used in the application of microphones, speakers and other acoustic transducers. The sensors for lower ultrasound frequency can be applied to non-destructive detection, ultrasound identification and ultrasonic range finding. Due to the remarkable mechanical properties, stretching ability and good biocompatibility, graphene has been considered as an ideal component for the soft electronics and biosensors. This research on graphene-based transducers have paved a path to graphene-based soft acoustic sensors for biomedical applications.

1.4.1 Research objectives

The objectives include developing process for the fabrication of and characterization of graphene-based open cavity resonator for lower frequency ultrasound detection, graphene-based closed cavity for audio and lower frequency ultrasound sensing and graphene-based electro-static transducers for audio and lower frequency, as shown in Figure 1.10. The fabrication process and graphene transfer methods have been modified and developed to achieve different structures of graphene-based sensors. By changing the size of cavity, the devices can be modified into sensing audio frequency or lower ultrasound frequency (lower than 200 kHz). The characterization of the devices, including the frequency response,

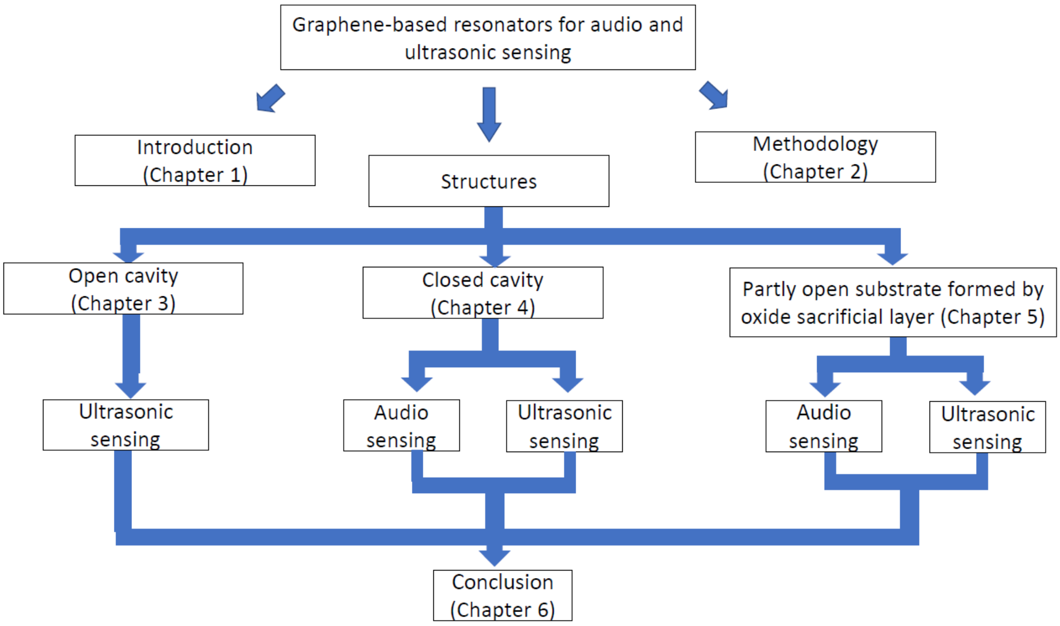

Figure 1.10: Main objectives of the thesis showing the different structures of acoustic resonators based graphene membranes.

Raman spectrum, the strain study of graphene-based membranes, will be investigated comprehensively. In addition, finite element analysis simulation has been applied. The capability of making large aspect ratio of graphene-based devices, opens a door to the development of acoustic transducers with higher sensitivity and better performance.

1.5 Thesis arrangement

The thesis includes six chapters. Chapter 1 introduces MEMS technology, briefly describes the important properties of graphene and illustrates the motivation of this project. Chapter 2 shows the graphene transfer methods which has been used widely so far and the working principles of Raman spectroscopy, white light interferometry, laser Doppler Vibrometer and finite element analysis. Chapter 3 is devoted to fabrication and characterisation of graphene-based open cavity resonator for ultrasound sensing (lower than 100 kHz). Chapter 4 is dedicated to fabrication and characterisation of ultra-large graphene-based closed cavity resonators for the detection of audio and lower ultrasound frequency. The new modified transfer method using Kapton tape as frame will be illustrated in this chapter. Chapter 5 includes fabrication and characterisation of graphene-based electro-static sensors using oxide sacrificial layer for audio and lower ultrasound frequency detection. The newly developed graphene transfer method has achieved the relatively minimum air gap of millimetre size graphene-based membrane devices, which have been reported so far. Chapter 6 concludes the main achievements of this project and suggestions for future work.

Chapter 2

Methodology

This chapter introduces the preparation and transfer method of graphene related to this research, shown in Section 2.1. The mechanism and characterization of the Raman spectrometer, white light interferometry, laser Doppler vibrometer and finite element analysis are illustrated in Section 2.2, Section 2.3, Section 2.4 and Section 2.5 respectively.

2.1 Preparation and transfer method of graphene

In this project, the 6 - 8 layers CVD graphene on copper foil produced by the ACS Material has been used. The CVD graphene transfer technique is divided into wet transfer and dry transfer, according to the structure of the target substrate. The schematic of wet transfer method and dry transfer method is shown in Figure 2.1. With the supporting frame, the membrane can easily be taken out from the enchant and dried in the air. Dry transfer method avoids the liquid from being trapped inside the closed cavity, unlike wet transfer method. A modified dry transfer method, which is developed by our group and used for fabricating acoustic sensors with large aspect ratio, is described in Chapter 4.

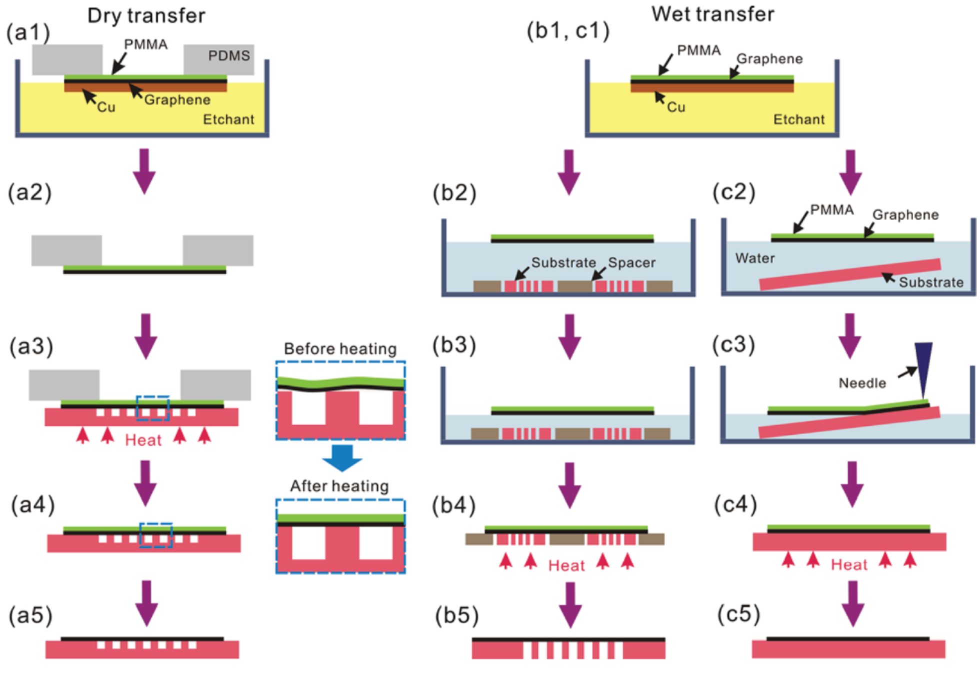

Figure 2.1: The schematic of wet and dry transfer method for CVD graphene.[66]

2.2 Raman spectroscopy

2.2.1 Principle of Raman spectroscopy

The Raman effect is considered as the inelastic scattering of electromagnetic radio, which is the basis of Raman spectroscopy. The energy is transferred between the photons and the molecular vibrations under incoming radiation (typically from the laser beam). The scattered photons have a different energy to the incident photons [68]. From Schrödinger equation under harmonic oscillation approximation, the limited number of energy levels(eigenstates) are allowed [68]:

$$E_\mathrm{v} \quad = \quad (v+\frac{1}{2})hv_\mathrm{v} \quad (v=0,1,2,\dots), \tag{2.1}$$

with v referring to the vibrational quantum number, h Planck's constant and v_v the molecular vibrational frequency.

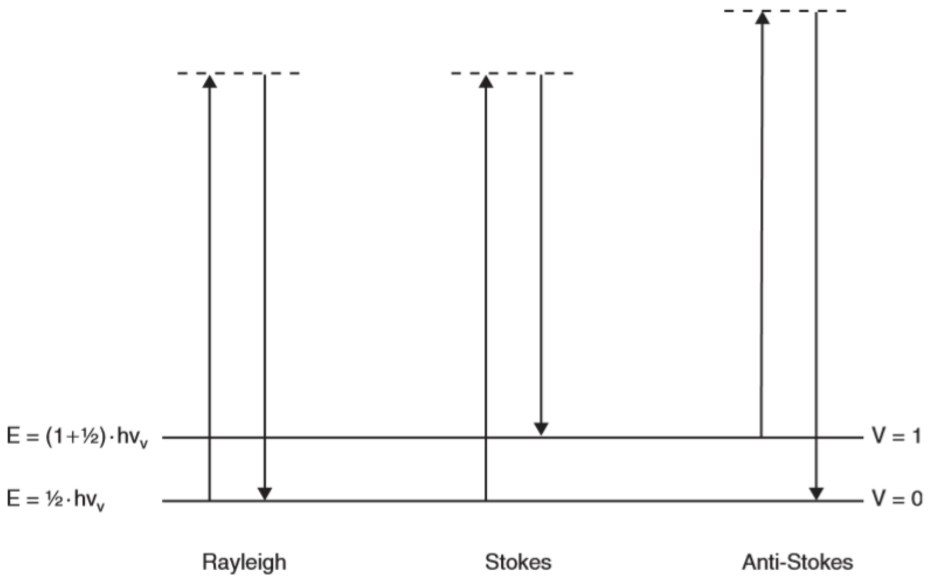

Figure 2.2: The idealised model for the dispersion of light by molecules. [68]

The quantum number (v) 0 or ± 1, during the transition between one vibration level to the next. The quantum number of 0 suggests the energy difference during the interaction is zero and this elastic process is termed as Rayleigh scattering. On the other hand, the Raman scattering is considered, where stokes or anti-stokes scattering referring to the higher or lower energy difference, respectively. The idealised energy levels of Rayleigh and Raman scattering are showed in Figure 2.2. The energy difference during the scattering determines the position a Raman band in the spectrum, which is decided by the vibrational frequency (v_v).

Additionally, the vibrational frequency (v_v) can be estimated as:

$$v_\mathrm{v} \quad = \quad \frac{1}{2\pi}\sqrt{\frac{\kappa}{\mu}}, \tag{2.2}$$

and κ is the force constant of the bond, with μ the reduced mass.

For a diatomic molecule, the reduced mass (μ) is defined as:

$$\frac{1}{\mu} \quad = \quad \frac{1}{m_1} + \frac{1}{m_2}, \tag{2.3}$$

where m_1 and m_2 represent the masses of the atoms forming the bond. More atoms are involved for the complicated systems and the equation can be expanded.

The force constant of the bond (κ) and the reduced mass (μ) are related to the type of bond or a functional group. From the equation (2.2), the Raman band position can be determined, Therefore the Raman effect are applied to the non-destructive spectroscopic technique for material characterization.

2.2.2 Raman features of graphene

Raman spectrum shows the layers number and the quality of graphene, which reflects change in electron band [69]. As shown in Figure 2.3, G peak at 1580 cm^{-1} and 2D peak at 2700 cm^{-1} can be observed in the Raman spectrum of graphene. The presence of G peak results from the doubly degenerate zone center $E_{2\mathrm{g}}$ mode [70]. 2D peak is the second order of zone-boundary phonons. D peak at 1350 cm^{-1} is generated by the zone-boundary phonons in defected graphene [70], which is absent in Figure 2.2.2.

The Raman spectra functions as the fingerprint of the graphene and shows the quality and properties of the graphene films. The layer number of graphene can be determined by the equation [71]:

$$n^{1.6} = \frac{11}{W_G - 1581.6} - 1, \tag{2.4}$$

where n refers to the number of the membrane layers, as well as W_G shows the band position in wavenumbers.

The peak intensity ratio of 2D and G bands (I_{2D}/I_G) reflects the film quality. The strain in the membrane can also be estimated from the Raman analysis. The specific analysis of Raman spectrum on our research will be illustrated in Chapter 4.

During this project, the Raman measurements have been performed in Raman

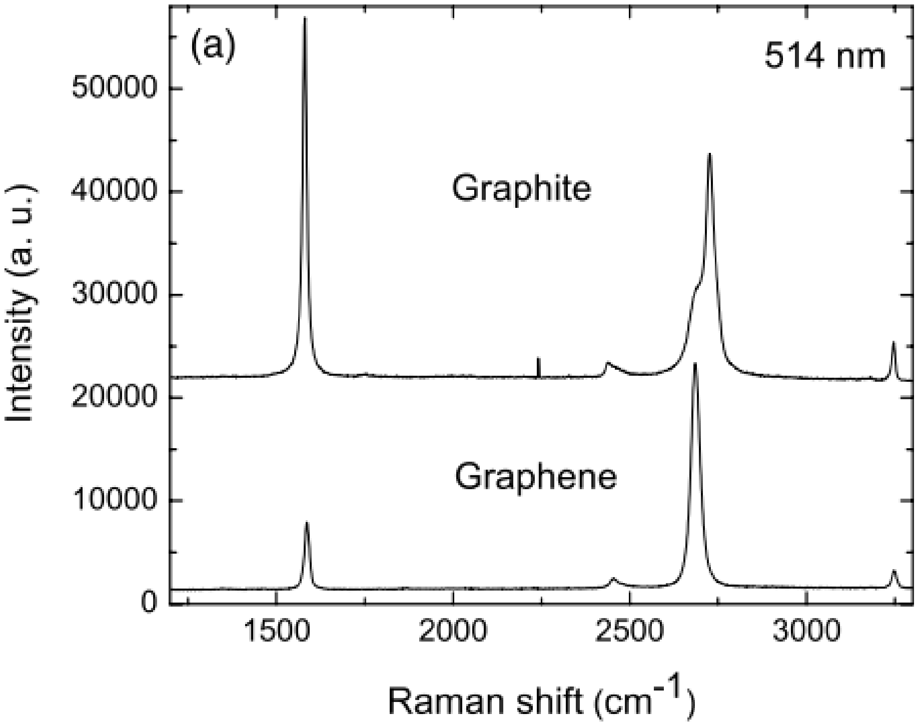

Figure 2.3: Raman spectrum at 514 nm for graphite and graphene. [69]

Spectroscopy (inVia Renishaw) using 0.8 mW laser power, with laser excitation of 514.5 nm and a 100x objective.

2.3 White light interferometry

White light interferometry (WLI) is an equipment for measuring the surface topography optically and with non-contact. The phase difference between the measurement beam and reference beam which are generated by a light source passes through a beam splitter, results in interfaces [72, 73]. The constructive interference generates from the same optical path between the measurement beam and reference beam, which is with maximum intensity of the camera pixel [72–74]. The destructive interference takes place when the optical path is different, which is with minimum intensity of the camera pixel [72–74]. The setup of interference microscope has been shown in Figure 2.4 [74] and for WLT, the white light has used as the light source. In this project, WLI(Zygo, New View 100 Interferometer) has been used for the non-contact surface profile measurement of graphene/PMMA membranes. The surface profile of graphene/PMMA resonator measured by WLI is shown in Chapter 4.

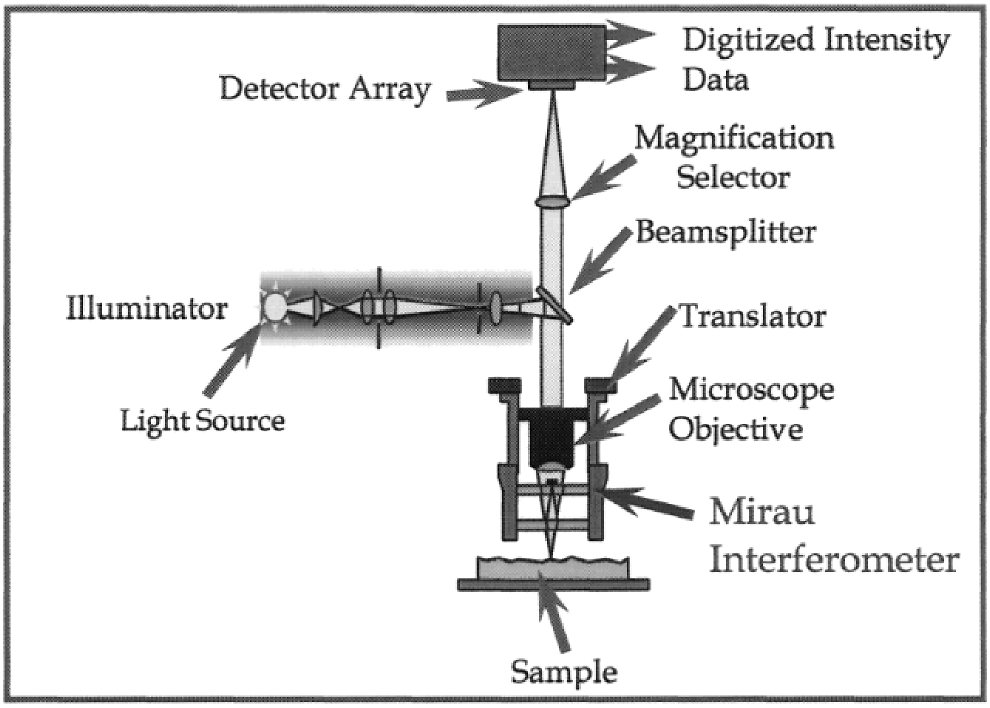

Figure 2.4: The schematic of interference microscope. [74]

2.4 Laser Doppler vibrometer

Laser Doppler vibrometer (LDV) is a technique used to measure the velocity of a moving sample by projecting it with laser beam and detecting the Doppler shift of the light scattered by the moving sample [75]. To be more specific, the frequency of the incoming light is changed by a moving object, which is termed as the Doppler effect [76]. As shown in Figure 2.5, the laser beam has been split into two beams with equal intensity via beam splitter and a fringe pattern is formed. A sample moves through the fringes and reflects light which is collected by photodetector and converted to electronic signal [77]. The Doppler shift between incident light and scattered light is proportional to the moving sample velocity. The electrical signal from the photodetector is proportional to the sample velocity [78]. With LDV, the dynamic behavior of the devices including resonant frequencies and mode shapes have been determined.

In this project, the dynamic behavior of the graphene/PMMA membranes has been characterized by Polytec NLV-OPTIK LDV and measured at room temperature and under atmospheric pressure. For the mechanical actuation, the samples have been placed on the sticky pad on the piezo-electronic disks. The piezo-disks have been mounted on the LDV station with Blu Tack. For other actuation methods, the samples have been placed on gel carrier chip boxes. The chip boxes have been mounted on the LDV station with Blu Tack.

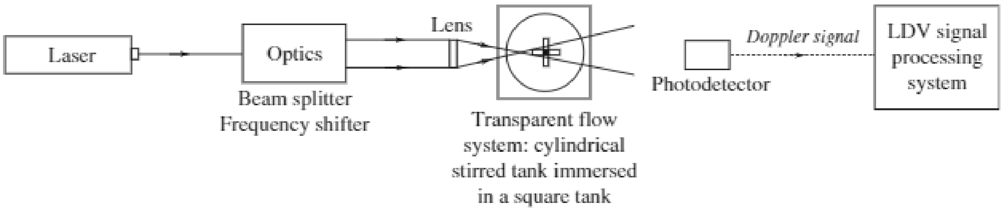

Figure 2.5: The schematic of laser Doppler vibrometer. [77]

2.5 Finite element analysis

Finite element analysis (FEA) is a numerical model to solve patrial differential equations in engineering, namely, structural analysis, heat transfer and electromagnetic filed. To solve complicated geometries, material properties, finite elements which are smaller and simpler units are divided equivalently from the body, and interconnected at nodes, boundary lines or surfaces. The equations of each fine element are formulated and combined to solve the entire body [79]. In a FEA model for structural analysis in continuous domain (Figure 2.6), the applied external forces are termed as volume force(e.g. gravity), surface force (e.g. drag force by pressure) and concentrated load (e.g. point load on subject). The external loads affect the stress distribution over the domain [77, 80].

Coventorware 10 is used for FEA simulation in this research project. The dynamic behavior of the devices including the frequency response, stress analysis and mode shape can be simulated with FEA model. During this research project, the constraints have been set to the anchor between the membranes and the substrates as well as the substrates. For the simulation of mechanical actuation, the pressure has been loaded on the back surface of the substrate. In case of the electro-thermal simulation, the voltage has been applied to the electrodes on the membrane. The properties of material used in FEA simulation have shown in Table 2.1.

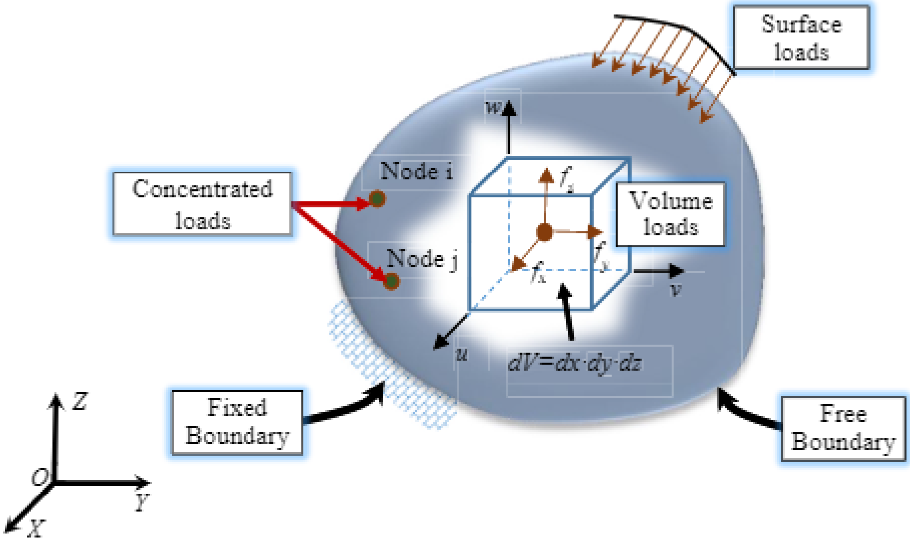

Figure 2.6: A description of a finite element analysis model for structure analysis. [80]

2.6 Summary

This chapter includes the normal fabrication and transfer of graphene developed by other groups, the working principles and characterization of Raman spectroscopy, WLI, LDV and FEA. The conventional graphene wet transfer method has been used for the graphene-based open cavity ultrasound resonator, which

Table 2.1: Parameters of the materials used in simulations of graphene/PMMA membranes

properties	value	
	graphene	PMMA
Thickness	1.8 mm	450 nm
Young's modulus	1 TPa [18]	3.8 GPa [81]
Poisson's ratio	0.16 [82]	0.4 [83]
Mass density	$2 \times 10^3 kg/m^3$ [18]	$1.1 \times 10^3 kg/m^3$ [81]
Thermal expansion coefficient	$-7 \times 10^{-6} K^{-1}$ [19, 21]	$7.7 \times 10^{-5} K^{-1}$ [81]
Thermal conductivity	$5.3 \times 10^3 W/mK$ [19, 20]	0.24 W/mK [81]

will be illustrated in Chapter 3. A modified graphene dry transfer method with Kapton tape as supporting frame has been used for graphene-based closed cavity resonators and will be illustrated in Chapter 4. The newly developed graphene transfer method using silicon dioxide as sacrificial layer to achieve around 2 μm air gap for millimeter-size graphene-based membranes and to fabricate graphene-based capacitive sensors will be presented in Chapter 5. The confirmation of graphene layers measured by Raman spectroscopy will be provided accordingly. The static deformation of the graphene-based membrane suspended over closed cavity resonator has been detected by WLI and illustrated in Chapter 4. The dynamic behaviour of the devices has been characterized by LDV and analyzed by FEA simulation.

Chapter 3

Fabrication and characterisation of graphene-based open cavity resonator for ultrasound sensing (lower than 100 kHz)

In this chapter, the experimental realization of graphene/PMMA open cavity is presented. The graphene/PMMA membrane has been wet transferred onto the square open cavity with the side length of 0.5 mm. The characterization under the mechanical and electro-thermal actuation scheme has been determined.

3.1 Introduction

The discovery of graphene[84] has granted an entrance to the new design of nanoelectromechanical systems (NEMS)[85, 86] and microelectromechanical systems (MEMS)[87–90] due to the unique mechanical and electrical properties of the graphene, including its extremely high Young's modulus (up to 1 TPa)[91], remarkably high mechanical strength (∼130 GPa)[91], super low mass density (2200 kg/m^3) and superior electro-conductivity (200,000 $cm^2V^{-1}S^{-1}$[92].

The remarkable mechanical and electrical properties of graphene also suggest graphene hold the promise of be ultrasound application with good performance[93]. Ultrasound detection has been applied to diagnostic imaging[94], non-contact and non-destructive sensors[95, 96], ultrasonic range finder[97] and ultrasound identification[98]. Due to the extremely large Young's modulus, the typical resonant frequency of the graphene resonators has been reported to be in the order of Mega Hertz[22, 93, 99–104], which shows the potential of achieving ultrasound sensors with resonant frequency up to 10-100 MHz. Thus far, the frequency response of the graphene resonators has been measured in vacuum [22,93,99–104]. Under atmospheric pressure, the vibration of graphene membrane is hard to be detected due to the presence of air damping and therefore graphene-based ultrasonic detector might not be used to measure the air-carried ultrasound. Furthermore, to detect ultrasound frequency (lower than 100 kHz), the dimension of the suspended graphene membrane should be around hundreds of micrometres. The difficulty increases to achieve a free-standing atom-scale graphene membrane with such a large aspect ratio (the membrane's diameter versus thickness).

In this work, we report a graphene/PMMA open cavity resonator for ultrasound sensing. The 450 nm thick PMMA layer has been laminated to 6-layer graphene membrane to support the multilayer graphene membrane during the graphene wet transfer and also works as protection layer. The graphene/PMMA membrane has been transferred and clamped fully over the square open cavity of the side length of 0.5 mm. The aspect ratio (the membrane's side length versus thickness) has been estimated to be around 1100. Two samples using graphene wet transfer method have been fabricated with the success rate of 100%. The wet transfer method has been widely and considered to be a reliable and simple graphene transfer method with high repeatability and success rate. The resonant frequency of the graphene/PMMA open cavity resonator has been measured to be less than 80 kHz under mechanical and electro-thermal actuation at room temperature in atmospheric pressure. The dynamic behaviour of the graphene/PMMA ultrasonic open cavity resonator has been determined for the first time.

3.2 Device design and operating principles

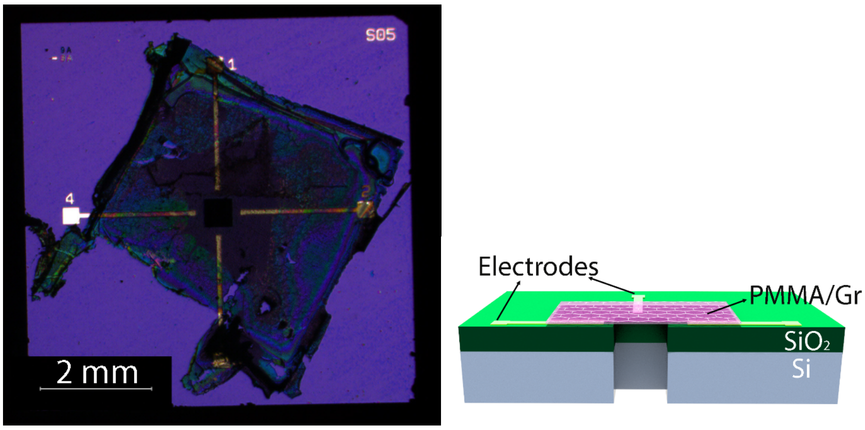

(a) (b)

Figure 3.1: The optical image (a) and cross-section schematic (b) of the graphene/PMMA open cavity resonator for ultrasonic sensing.

The optical image of the graphene/PMMA ultrasonic open cavity resonator has been shown in Figure 3.1 (a). The membrane includes 6-layer graphene and 450 nm PMMA suspended over the open cavity with a side length of 0.5 mm. The graphene layer has been attached on the silicon dioxide layer and connected to the aluminum (Al) electrodes. As the cross-section schematic shows in Figure 3.1 (b), the square open cavity has been etched through the silicon substrate with thickness of around 380 μm. The natural frequency formula for the graphene/PMMA membrane in vacuum can be expressed as[105, 106]:

$$t_{\mathrm{eff}} = t_{\mathrm{g}} + t_{\mathrm{p}}, \tag{3.1}$$

$$\rho_{\mathrm{eff}} = \frac{\rho_{\mathrm{g}} t_{\mathrm{g}} + \rho_{\mathrm{p}} t_{\mathrm{p}}}{t_{\mathrm{g}} + t_{\mathrm{p}}}, \tag{3.2}$$

$$f_{\mathrm{mn}}^{\mathrm{vac}} = \frac{1}{2\mathrm{d}} \sqrt{\frac{\mathrm{N}(\mathrm{m}^2+\mathrm{n}^2)}{\rho_{\mathrm{eff}} t_{\mathrm{eff}}}}, \tag{3.3}$$

where t and ρ are thickness and density of the material, t_{eff} and ρ_{eff} refer to the effective thickness and effective density for graphene (g)/PMMA (p) bi-layer membrane, d is the dimension of the square membrane, N represent the overall tension in the membrane, m and n describe the mode number.

Under atmospheric pressure, the air damping should be considered, using[107]

$$f_{\mathrm{mn}} = \frac{f_{\mathrm{mn}}^{\mathrm{vac}}}{\sqrt{1 + 1.34\frac{\rho_{\mathrm{air}}\mathrm{d}}{\rho_{\mathrm{eff}}t_{\mathrm{eff}}}}}, \tag{3.4}$$

where ρ_{air} is the density of the air. Despite having applied atmospheric damping correction for the circular membranes [107], a proper estimation should be obtained by applying to the square membranes in this work.

3.3 Materials and methods

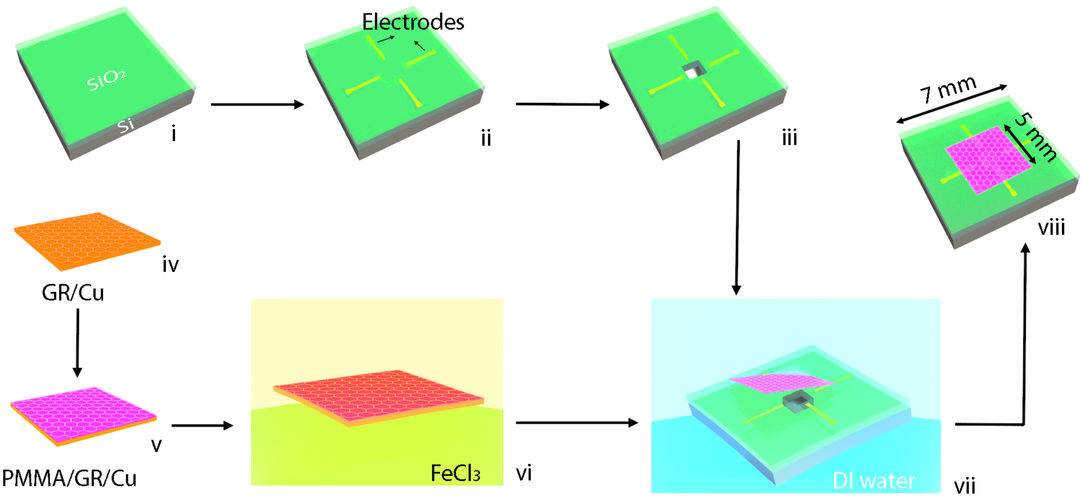

Figure 3.2: The fabrication process of the graphene/PMMA open cavity resonator for ultrasonic sensing: the preparation of the substrate: i. the deposition of silicon dioxide; ii. the deposition and patterning of electrodes on the silicon dioxide layer; iii. the etching of the square open cavity with the side length of 0.5 mm; the preparation of the graphene/PMMA membrane: iv: the graphene/Cu foil; v. PMMA spin-coated onto the graphene/Cu foil; vi. the etching of Cu by ferric chloride; the wet transfer of graphene/PMMA membrane: vii. the graphene/PMMA membrane being wet transferred onto the substrate; viii. the resonator has been cooled down to the room temperature in the open air.

As shown in Figure 3.2, the schematic of the fabrication process includes: a. the preparation of the substrate: i. The 275 nm silicon dioxide has been deposited onto the silicon substrate; ii. the aluminum electrodes with the thickness of 300nm have been deposited and patterned on the silicon dioxide layer; iii. the square hole with the side length of 0.5 mm has been patterned and etched into silicon dioxide and through silicon; b. the preparation of the graphene/PMMA membrane: iv. the chemical vapour deposition (CVD) grown 6-layer copper (Cu) foil has been cut to the square with the 5mm side length. The 5 mm side length has been chosen to decrease the difficulty of graphene wet transferred onto chip with 7 mm side length; v. 450 thick PMMA has been spin coated onto the graphene/Cu foil and then has been dried in 80 °C for 5 minutes and following in 130 °C for 20 minutes; vi. the Cu foil has been etched in the 4.5% iron chloride ($FeCl_3$) etchant and the graphene/PMMA membrane has been released from the Cu layer; vii. the graphene/PMMA membrane has been scooped from the etchant and placed into the deionized water (DI water) and transferred onto the target substrate inside the DI water; he resonator with graphene/PMMA membrane has been placed on the hot plate at the temperature of 80 °C for 5 minutes for the DI water to be evaporated and moved to the other hot plate at 140 °C for 10-20 seconds to prevent the ripples on the graphene/PMMA membrane[83]; viii. the resonator has been cooled down to the room temperature in the open air. The side length of the substrate has been designed to be 7 mm and the side length of membrane has been measured to be around 5 mm respectively.

3.4 Results and discussion

3.4.1 Dynamic actuation

To characterise the dynamic behaviour of the graphene/PMMA membrane fully clamped on the open cavity, mechanical and electro-thermal actuation have applied to the resonator. The dynamic characteristics have been detected by the

Polytec laser Doppler Vibrometer (LDV). In the case of mechanical actuation, the graphene/PMMA membrane has been placed on the piezoelectric disk. By applying voltage to the piezoelectric disk, the vibration has been transmitted from the piezoelectric disk to the substrate of the resonator. In the electro-thermal actuation, the voltage has been applied between the aluminum electrodes which are connected to the graphene layer and the membrane has been actuated by the thermal stress generated by the Joule heating. The actuation signal of frequency sweep and the square waves of the measured resonant frequency of the suspended graphene/PMMA membrane have been applied to the resonator. Compared to the signal of frequency sweep, the graphene/PMMA membrane under the actuation of the square wave function has longer time for vibration and reaches the larger amplitude. The sensitivity of amplitude under the square wave function and the related mode shape of the device actuated mechanically and electro-thermally have been measured.

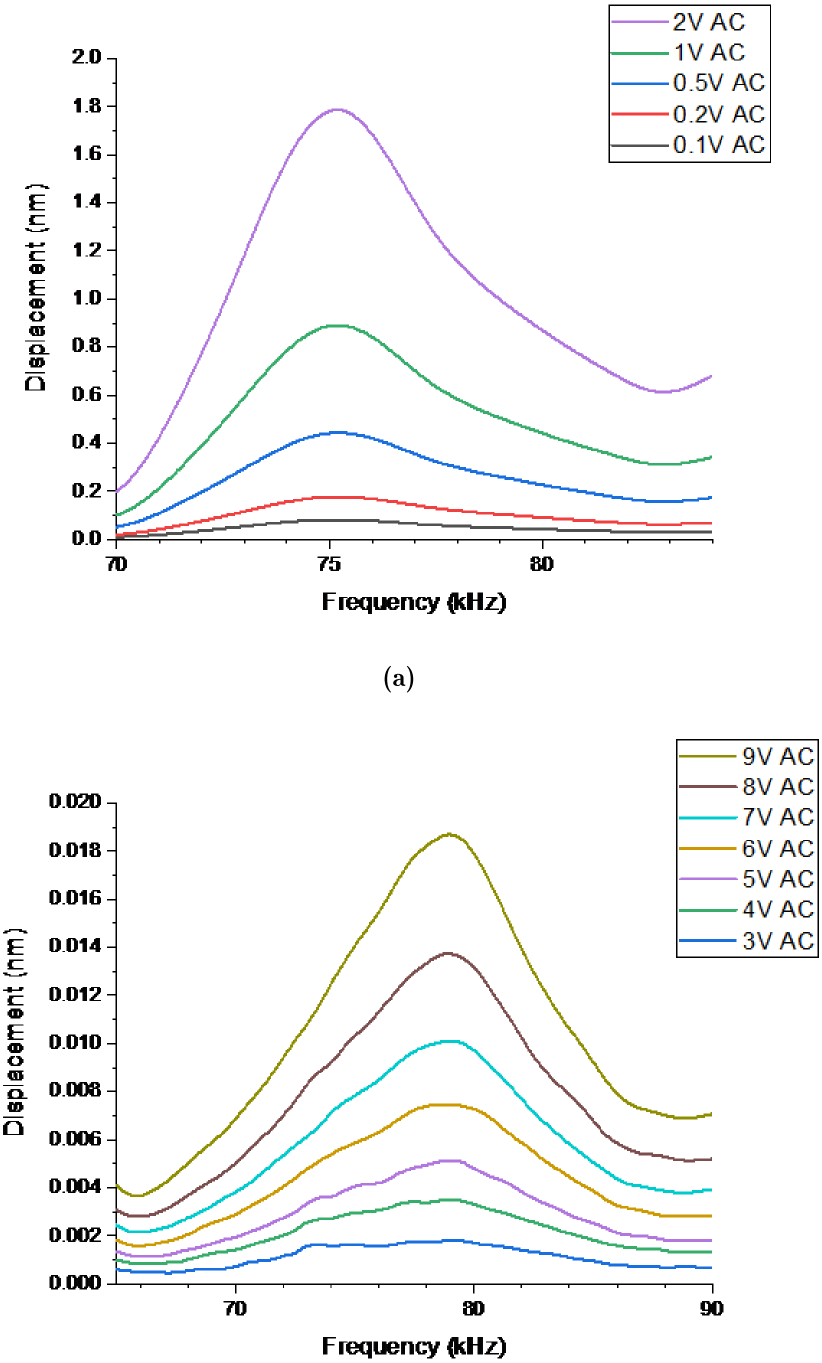

(a)

(b)

Figure 3.3: The frequency response of the graphene/PMMA open cavity ultrasonic resonator under: (a) mechanical actuation with varying AC voltage from 0.1 V to 2 V and constant DC voltage of 1 V; (b) electro-thermal actuation with the varying AC voltage from 3 V to 9 V and constant 1V DC.

Mechanical actuation

The frequency response of the graphene/PMMA membrane under mechanical actuation varying from 0.1 V AC to 2 V AC and constant 1 VDC has been shown in Figure 3.3.a. The resonance at the 0.1 V AC has been hardly observed, of which the potential explanation is the small amplitude of the membrane's displacement actuated by the vibration from the piezo-disk at the AC voltage of 0.1 V. At AC voltage from 0.2 V to 2 V, the resonant frequency has been measured to be 75.208 kHz ± 0.006%. The displacement of membrane at the resonant frequency has been detected to rise from 0.18 nm to 1.79 nm with the increasing AC voltage from 0.2 V to 2 V.. The frequency response (1 V AC, 1 V DC) on the substrate of open cavity resonator has been shown in Appendix A, which shows the frequency response has been associated with the membrane. With Equation (3.5), the quality factors of the frequency response under mechanical actuation(as shown in Figure 3.3.a) have been estimated to be 17.024 ± 2.5 % .

The quality factor has been derived by:

$$Q = \frac{f_{\mathrm{r}}}{\Delta f}, \tag{3.5}$$

where Q as the quality factor, f_{r} refer to the resonant frequency and Δf is full width at half maximum (-3 dB of attenuation).

Electro-thermal actuation

The frequency response of the membrane actuated electro-thermally has been shown in Figure 3.3.b. The frequency sweep signal with the voltage of varying 3-9 V AC and constant 1 V DC has been applied to the membrane via the electrodes. The resonant displacement has been observed to be relatively small under 3 V AC. The resonant frequency has been detected to be 79.005 kHz ± 0.14% and the displacement has been detected to rise between 3.5 pm to 18.7 pm at the range of the actuation AC voltage from 4 V to 9 V and constant 1 V DC.

With Equation (3.5), the quality factors of the frequency response (Figure 3.3.b) have been estimated to be 8.96 ± 11% at the AC voltage from 4 V to 9 V.

The increase of the resonant frequency of the device has been observed under electro-thermal actuation compared to the mechanical actuation. The possible contribution to the frequency upshift is that the different actuation mechanism between the two actuation methods and electro-thermal hardening of the graphene layer[22]. In the case of mechanical actuation, the direction of the dominant actuation stress has been out-of-plane which has been generated by the piezo-disk underneath the substrate of the resonator. In the case of electro-thermal actuation, the actuation stress has been introduced by thermal expansion of the graphene/PMMA membrane and the direction of the dominant actuation stress has been in-plane. The different direction of the dominant stress is the possible reason for the shift of the resonant frequency by the two actuation methods. Additionally, due to the negative thermal expansion coefficient of graphene[108], the frequency would increase as the graphene membrane's temperature increases[22]. The temperature graphene/PMMA has been higher under the electro-thermal actuation than under the mechanical actuation, which might be related to the upshift of the frequency.

The smaller quality factor of the device in the case under the electro-thermal actuation (8.96 ± 11%), in comparison to mechanical actuation (17.024 ± 2.5 %), can be explained by the smaller amplitude under the electro-thermal actuation, which suggests that lower power has been transferred and stored in the device by electro-thermal actuation[109].

3.4.2 Sensitivity of amplitude

By applying the square wave signal at the resonant frequencies under the different actuation methods, the displacement of the graphene/PMMA membrane has been measured to increase with the input AC voltages, as shown in Figure 3.4. The displacement has been observed to increase linearly with the enlarging AC

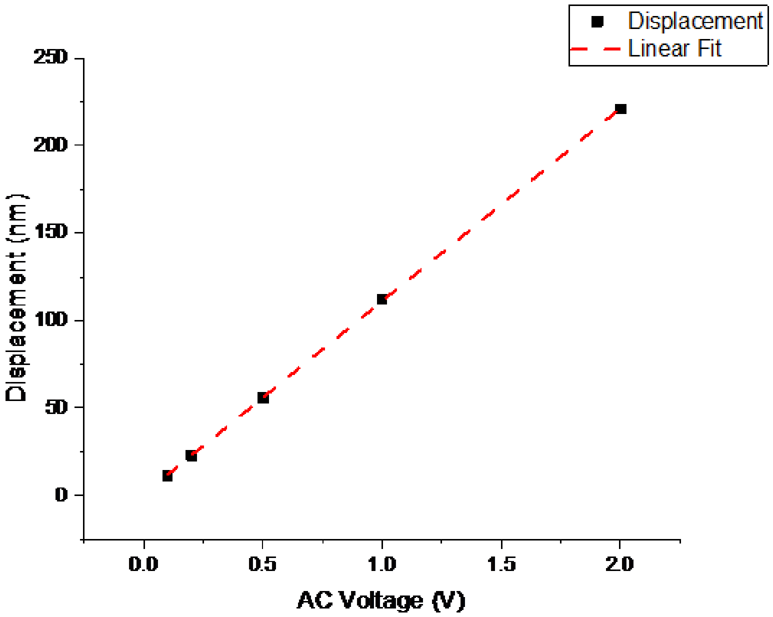

(a)

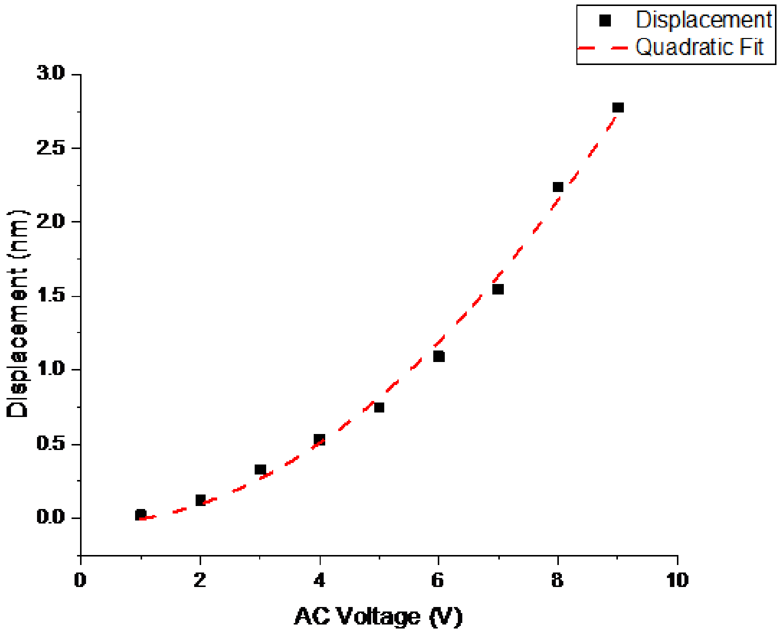

(b)

Figure 3.4: The amplitude of the open cavity resonator: (a) mechanically actuated at the frequency of 75.375 kHz and with increasing AC voltage from 0.1 V to 2 V and constant 1 V DC; (b) electro-thermal actuation at the frequency of 79.125 kHz and varying AC voltage from 1 V to 9 V and constant 1 V DC.

voltage (Figure 3.4.a), which shows the linear relation to vibration from the piezo-disk which has increased with the input AC signal. In the case of electro-thermal actuation, the displacement of the membrane has been observed to be quadratically related to the increasing AC voltage (Figure 3.4.b). The tension has been linear with Joule heat which is quadratic with the input AC voltage. The quadratic relation between the displacement and input AC voltage shows the displacement of the membrane has detected to be linear with the tension generated by the Joule heat. The linearity in displacement versus the actuation stress has been observed in both mechanical and electro-thermal actuations . The amplitude and the sensitivity of amplitude have been summarized in Table 3.1.

3.4.3 Mode shape

(0,1) mode shapes have been observed at the resonant frequencies under mechanical (0.2 V AC, 1 V DC) and electro-thermal (3 V AC, 1 V DC) actuation methods, which are shown in Figure 3.5. When the graphene/PMMA membrane has been actuated, the air is supposed to be pumped into the cavity to support the deformation of the membrane under the (0,1) mode.

Table 3.1: The amplitude and sensitivity of amplitude.

Actuation methods	Actuated resonant frequency	Input voltage	The range of amplitude	Sensitivity of amplitude
Mechanical	75.375 kHz	0.1 V AC to 2 V AC and 1 V DC	11.45 nm to 220.92 nm	110.26 nm/V
Electro-thermal	79.125 kHz	1 V AC to 9 V AC and 1 V DC	0.02 nm to 2.77 nm	0.034 nm/V^2

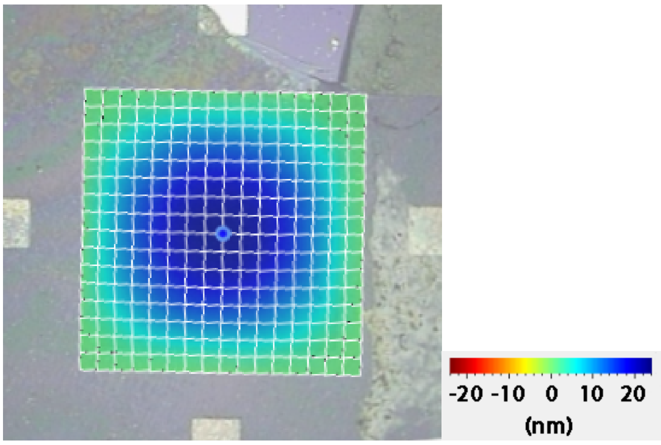

(a) scale bar

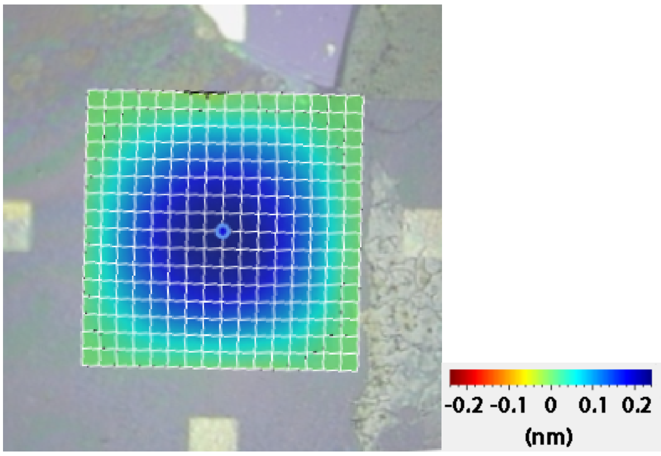

(b) scale bar

Figure 3.5: The mode shape observed under: (a) mechanical actuation at the frequency of 75.375 kHz and with the voltage of 0.2 V AC and 1 V DC; (b) electro-thermal actuation at the frequency of 79.125 kHz with voltage of 3 V AC and 1 V DC.

3.4.4 Strain analysis

The strain and tension of the graphene/PMMA membrane over the open cavity have been estimated from the Equation (3.1) to (3.4) and shown in Table 3.2. The resonant frequency has been measured to have 5% shift between the mechanical and electro-thermal actuation, which is related to the different tension in the graphene/PMMA membrane actuated by the two methods. The different tension is contributed by the different direction of the stress or the negative TCE of graphene.

3.4.5 Simulation

Finite element analysis (FEA) has been conducted on the membrane suspended over the open cavity in order to investigate the relationship between the device's dynamic behaviour and input signal in the mechanical and electro-thermal actuation. The simulation has been performed with Coventorware 10. The mechanical simulation has been conducted by applying pressure to the membrane. As illustrated in Figure 6 (a), the stress over the membrane generated has been observed to be proportional to increasing pressure (from 0.1 Pa to 1 Pa) that has been applied to the membrane. The displacement which has been actuated by rising stress has been observed to increase linearly with the input pressure. In case of electro-thermal simulation, by applying the increasing voltage from 1 V to 10 V through the electrodes of the membrane, the stress and temperature have been simulated to grow quadratically, which has been shown in Figure 6 (b). The stress has been observed to be linear with the membrane's temperature and quadratic to

Table 3.2: the strain and tension in the graphene/PMMA membrane derived from the measured frequency.

Actuation	Resonant frequency (kHz)	Tension (N/m)	Strain (%)
Mechanical	75.21	7.16	0.1940
Electro-thermal	79.01	7.90	0.2140

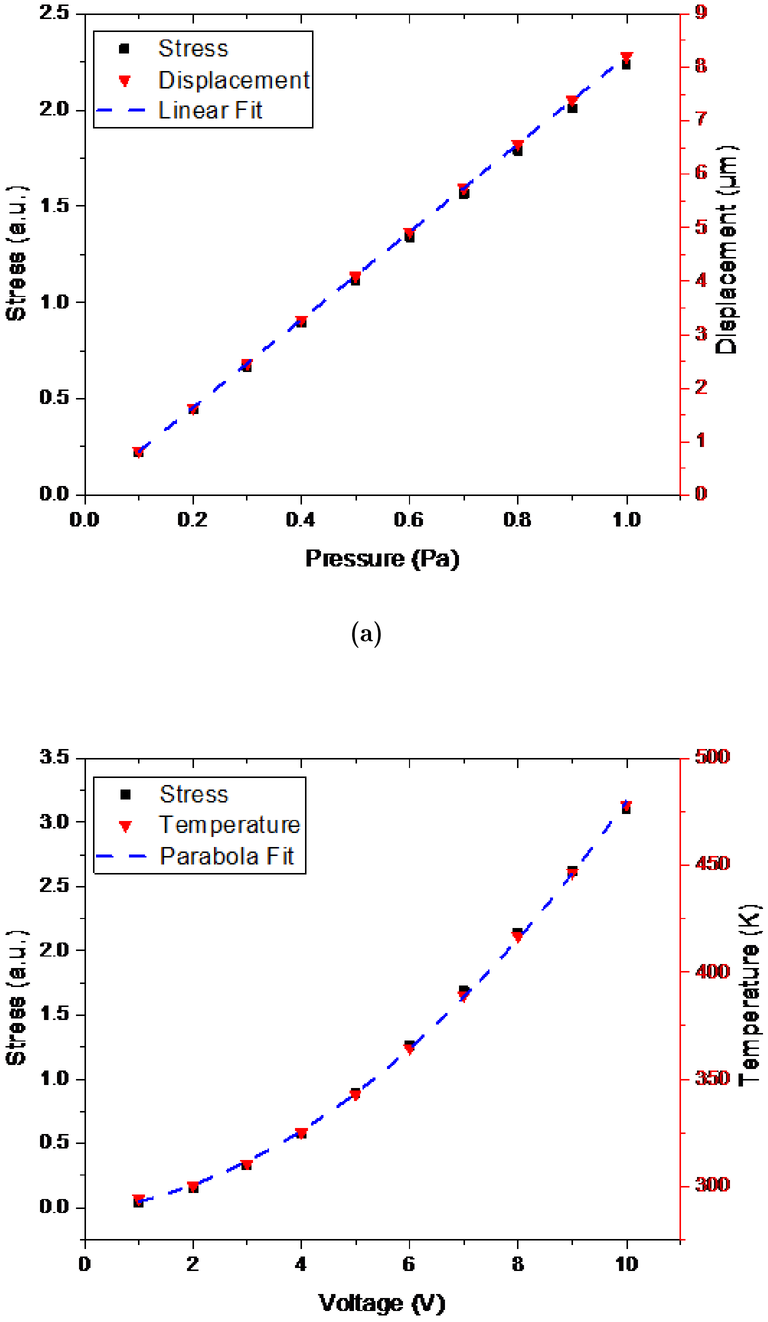

(a)

(b)

Figure 3.6: Continued

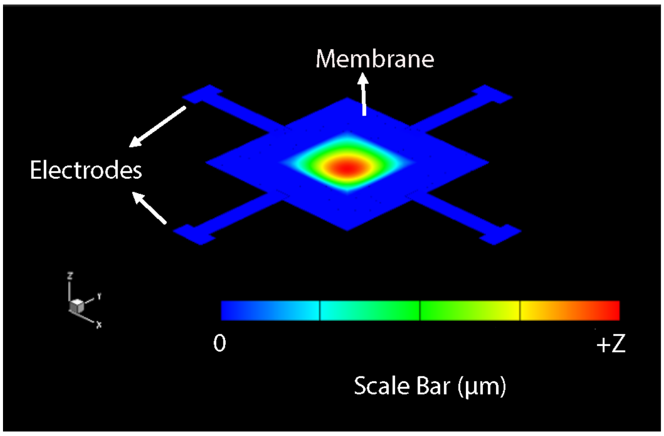

(c)

Figure 3.6: The FEA simulations: (a) the simulated stress and displacement of the membrane suspended over the open cavity versus the increasing input pressure; (b) the simulated stress and temperature with the rising voltage; (c) the simulated mode shape of the membrane under the mechanical and electro-thermal actuation.

the applied voltage. The simulated mode shape of the membrane has been (0, 1) mode and shown in Figure 6 (c) in both mechanical and electro-thermal actuation. Furthermore, in the case of the mechanical actuation, the actuation pressure has been applied to the membrane vertically, and the resonance of the membrane has simulated to be dominated by the out-of-plane stress. In the electro-thermal actuation, the voltage applied via the electrodes has produced the Joule heat and the corresponding thermal expansion over the membrane. The resonance has been simulated to be dominated by the in-plane stress. The simulated dynamic behaviour of the membrane has shown to be consistent with the experimental results.

3.4.6 Raman spectrum of graphene on open cavity ultrasonic resonator

The Raman spectrum of the graphene layer has been shown in Figure 3.7 and the positions and full width at half maximum have been summarized in Table 3.3. The Raman spectrum indicates the confirmation of graphene layer.

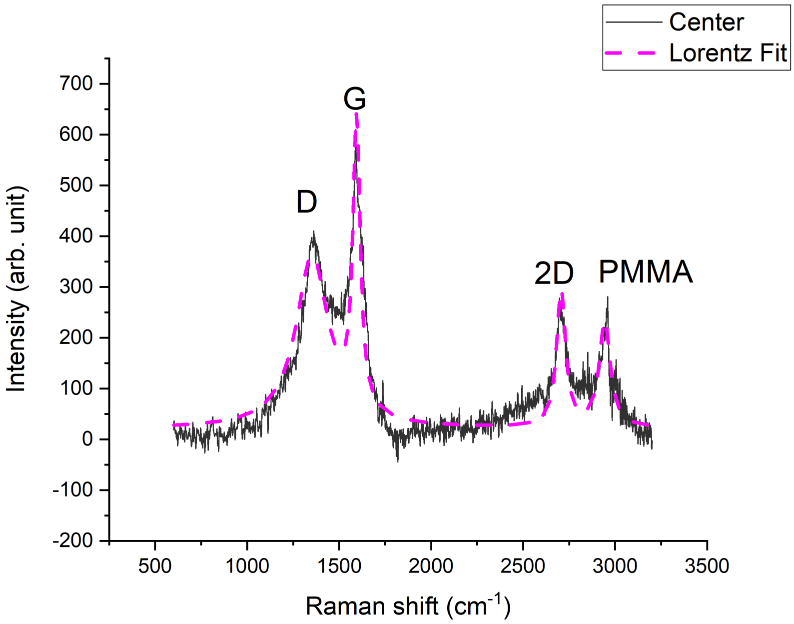

(a)

Figure 3.7: The Raman spectrum of graphene layer on the open cavity resonator for ultrasound sensing: full scan and PMMA peak at 2943.69 cm^{-1}

Table 3.3: Positions, full width at half maximum (FWHM) of the D, G and 2D peaks.

D		G		2D	
position (cm^{-1})	FWHM (cm^{-1})	position (cm^{-1})	FWHM (cm^{-1})	position (cm^{-1})	FWHM (cm^{-1})
1352.6	213.3	1594.4	49.1	2706.5	58.9

3.5 Conclusions

In conclusion, the graphene/PMMA open cavity resonator for ultrasound detection (less than 100 kHz) has been presented for the first time. The membrane consisted of 6-laye graphene and 450 nm PMMA has been fully clamped over the square open cavity with the side length of 0.5 mm. The graphene/PMMA closed cavity resonator has been actuated mechanically and electro-thermally. The resonator frequency has been measured to be around 75 kHz (mechanical actuation) and around 79 kHz (electro-thermal actuation) by applying the frequency sweep signal. The linear relationship between the membrane's displacement and applied mechanical stress has been observed. In addition, the membrane' displacement has been detected to be quadratic with input AC voltage in the case of electro-thermal actuation. The FEA simulations are in agreement with the experimental results and shows the linearity between the displacement of the membrane and actuation stress. The (0,1) mode has been observed to dominate the vibration at the resonant frequency. The overall strain in the graphene/PMMA membrane has been estimated be around 0.2 %. Our graphene/PMMA open cavity resonator shows the potential of ultrasound detection.

3.6 Summary

In this chapter, the fabrication and characterization of the ultrasound open cavity resonator have been illustrated. The substrates to form the capacitive structure and to enable electrical output signal are not included in the open cavity resonators, which is a challenge for open cavity devices to be integrated into the circuit. Thus, closed cavity graphene-based resonators for audio and ultrasound sensing are developed and will be illustrated in the next chapter.

Chapter 4

Fabrication and characterization of graphene-based closed cavity resonator

The devices in the open cavity structures could not achieve capacitive sensing and could not be used as the microphones or speakers. Thus, the closed cavity structures are designed to study the dynamic behavior of graphene-based membrane suspended over the substrates. Compared to open cavity structures, the challenges of the designing closed cavity devices are associated with how to modify the fabrication process, especially the transfer of graphene, and how to optimize the air gap and damping effect.

In this chapter, the realization of closed cavity resonators for audio sensing and ultrasound detection will be provided in Section 4.1 and Section 4.2 respectively. The chapter will illustrate a newly developed dry transfer method for millimeter scale graphene/PMMA membranes to fabricate the closed cavity resonators for acoustic sensing. Additionally, the dynamic behavior of the devices has been shown in this chapter, which reveals the potential of achieving graphene-based audio and ultrasound sensors.

4.1 For audio sensing

4.1.1 Introduction

To target the audio frequency range, processes for fabricating large aspect ratio graphene membranes around a few millimetres' diameter are necessary. Unlike the micrometre diameter graphene-based resonators [103,104,110–113], the millimetre diameter membranes are much more difficult to be suspended or clamped fully over the cavity due to the larger membranes' diameter to thickness aspect ratio. In particular, mono-layer and few layer graphene membranes could be damaged easily. Therefore, graphene-based membranes in previously reported acoustic sensors have been thickened by increasing the graphene layer number from 67 [90] to 1800 [114] or by attaching 200 nm to 3 μm thick PMMA layer [89,114], in order to increase the robustness of the membrane. The advantage of using PMMA as the supporting layer instead of increasing the graphene layer number by 1 to 3 orders of magnitude, is that lower resonant frequency can be achieved from the graphene-PMMA bilayer due to the lower density and elasticity of PMMA.

Previously, the fabrication methods developed for capacitive graphene-based microphones [87, 89, 90, 114], involve multiple steps, have been assembled manually and may have air leaking into the devices. The reported process is complex and can decrease the consistency of the devices' characteristics as a result of the manual assembling steps. Nevertheless, the devices reported exhibit relatively high sensitivity, ranging from -70 dB V to -20 dB V [87, 89, 90, 114, 115].

Recently, an ultra-large graphene-PMMA open cavity resonator [83, 105], has been reported by us. However, this design is not suitable for integration into the circuit system because the bottom electrode cannot be processed in the open cavity configuration. In addition, the open cavity device had been made using a wet transfer method. To fabricate large aspect ratio graphene-based membrane onto a closed cavity device, where electrical connections can be integrated into the substrate, it is necessary to use a dry transfer method since in the wet transfer method, liquid could be trapped inside the closed cavity.

Indeed, there are many challenges associated with suspending graphene-based membrane with large aspect ratio over a closed cavity as a device for acoustic sensing, namely, the optimization of the spacing between the membrane and the substrate, the prevention of the membrane from shorting the device by touching the substrate and the minimization of damping effects within the formed cavity. Thus far, despite the progress made in the fabrication and characterisation of graphene-based acoustic sensors, the resonance and associated dynamic deformation of the graphene-based acoustic sensors have not been studied, which are significant in understanding the membrane's characteristics and hence, improving the performance of the graphene-based acoustic sensors.

In this work, we have developed a simplified one-step reliable process for fabricating a graphene-PMMA closed cavity resonator with an optimum gap of 220 μm for acoustic sensing. The bilayer membrane, with aspect ratio of 7800 over the closed cavity, includes 6-layer graphene and 450 nm PMMA. The device has been formed by a simplified one-step graphene-PMMA dry transfer method using Kapton tape as a supporting frame. Because the graphene-PMMA membrane has been attached and sealed on the closed cavity substrate by van der Waals force, the gas encapsulation is better than the devices in which the membrane and the substrate are connected by case or cartridge via manual assembly. The static deformation of graphene-PMMA membrane suspended over the closed cavity has been measured in this study. Furthermore, the dynamic resonance characteristics of the graphene-PMMA closed cavity resonator actuated mechanically, acoustically and electro-thermally have been determined for the first time.

4.1.2 Device design and operating principles

Figure 4.1 (a) shows the structure of the graphene-PMMA closed cavity resonator which has been fabricated by transferring an ultra large area of graphene-PMMA membrane, over the closed circular cavity with 220 μm depth and 3.5 mm diameter. Figure 4.1 (b) shows an optical image of the resonator after transferring the graphene-PMMA layer over the closed cavity.

450 nm poly (methyl methacrylate) (PMMA) layer has been spin-coated on the 6 layers graphene as a supporting layer, to improve the stability of the graphene resonator and decrease the resonant frequency of the bilayer membrane. The resonant frequency formula for such a membrane [105] is:

$$f_{\mathrm{mn}} = \frac{\beta_{\mathrm{mn}}}{2\pi R}\sqrt{\frac{N}{\rho_{\mathrm{eff}} t_{\mathrm{eff}}}}, \tag{4.1}$$

where ρ_{eff} refer to the effective thickness and effective density for graphene (g)/PMMA (p) bi-layer membrane, R is the radius of the membrane, ρ is the density of the material, N is the tension in the membrane and β_{mn} is a dimensionless coefficient of the resonant mode.

The (0,1) and (1,1) modes of resonant frequency in such bilayer membrane has been estimated to be within the audio frequency range (20 Hz to 20 kHz), with the assumption of the 2.0 N/m tension in the membrane [105].

4.1.3 Materials and methods

Figure 4.2 illustrates the fabrication process of the graphene-PMMA closed cavity resonator, including the hollow substrate fabrication, modified graphene dry transfer method and the optical image of the graphene-PMMA membranes with the Kapton tape frame. Figure 4.2 (a) displays the procedure of making the hollow substrate. First, 500 nm silicon dioxide has been deposited on the silicon.

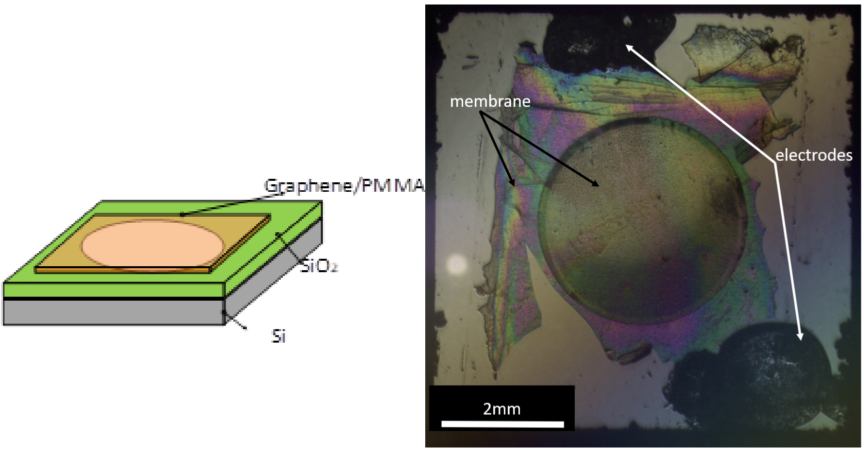

(a) (b)

Figure 4.1: The schematic (a) and the optical image (b) of the graphene-PMMA membrane closed cavity resonator with the silver paste as electrodes.

Next, 3.5 mm diameter hole has been patterned. After the silicon oxide layer on the cavity has been etched by reactive-ion etching (RIE), the silicon inside the cavity has been etched by deep reactive-ion etching (DRIE) to form a well with 220 μm depth.

Figure. 4.2 (b) shows the process of the dry transfer using the Kapton tape as a supporting frame. Firstly, 450 nm PMMA has been spin coated on the chemical vapor deposition (CVD) grown multilayer graphene copper foil. Kapton tape has been used to attach the edges of the PMMA/graphene/copper foil. Next, the copper has been etched away with 4.5% ferric chloride solution. After the membrane has been dried in the air completely, the membrane with Kapton tape frame has been transferred onto the substrate on the hot plate at a temperature of 140°C which is inside the range of PMMA glass-transition temperature (105°C-165°C) [66,67]. The membrane has been stuck on the substrate immediately when using a brush to make the membrane contact fully onto the substrate. When PMMA is heated to the glass-transition phase, the membrane area expands and the contact area enlarges. As a result, the adhesion between graphene-PMMA and silicon dioxide substrate increases [66, 67]. When the chip has been cooled down to room temperature, the frame could be peeled off easily from the sample

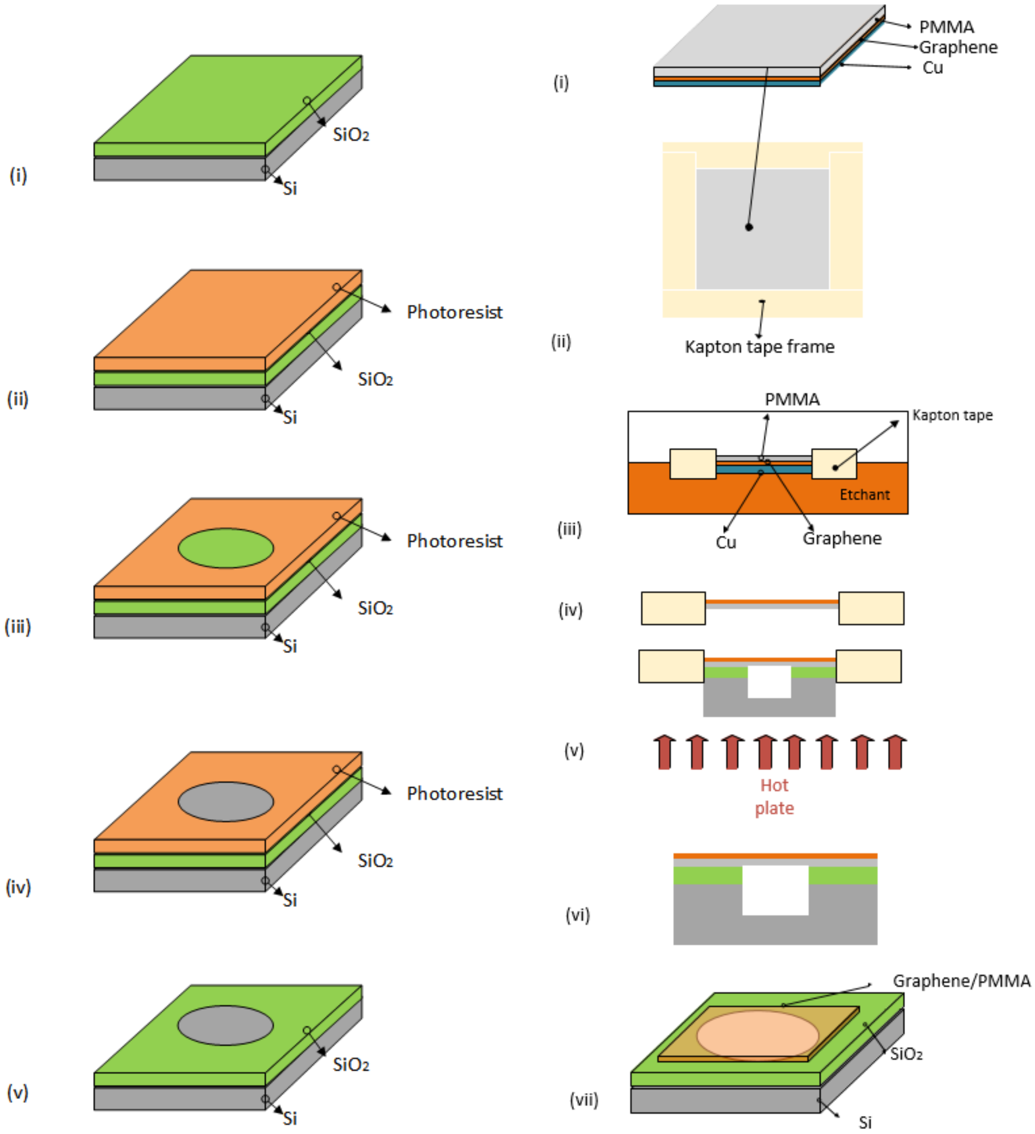

(a) (b)

Figure 4.2: Continued

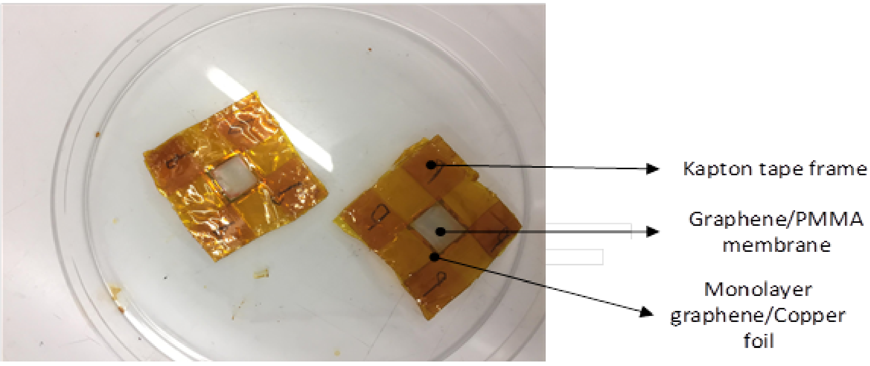

(c)

Figure 4.2: The fabrication process of the graphene-PMMA closed cavity resonator: (a) fabrication process of the substrate: (i) 500 nm oxide deposited on the silicon with PECVD; (ii) spin coat the 7 μm photoresist; (iii) pattern 3.5 mm diameter holes; (iv) etch silicon dioxide with RIE and silicon with DRIE; (v) dissolve the photoresist with acetone. (b) the modified dry transfer method process: (i) spin coat PMMA on the graphene/copper foil; (ii) use the Kapton tape to make a frame; (iii) wet etch the copper; (iv) dry the membrane in the air; (v) transfer the membrane onto the substrate on the hot plate on the temperature of 140°; (vi) peel off the frame after the substrate cooled down; (vii) the sample schematic illustration. (c) The optical image of graphene-PMMA membrane with Kapton tape supporting frame.

once the membrane has been clamped fully on the substrate.

Figure 4.2 (c) shows the optical image of the graphene-PMMA membrane with the Kapton tape supporting frame. The membrane is observed to be flat and without folding or wrinkling. The residual etchant has been cleaned by the DI water. The supporting frame has prevented the wet membrane from touching and sticking on the container surface.

In our work, the modified graphene-PMMA dry transfer method is faster and simplified for suspending ultra-large graphene-based membrane. In previous work, the graphene has been dry transferred to small features around a few microns [66,67]. The graphene with the Polydimethylsiloxane (PDMS) supporting frame requires more than 12 hours heating [66] or high temperature at around 200°C [67]. Here, for the large feature design, a brush could be used to make contact between the membrane and substrate, which replaces the long time and high temperature heating. In addition, the Kapton tape has been used to attach the edges of the membrane and work as a frame. Unlike PDMS, using Kapton tape frame does not require the step of patterning or etching the polymer, and decreases the process complexity. In previous research, the Kapton tape frame [90] with a hole in the centre has also been used as a supporting frame and spacer and has been included into the devices. Here, the Kapton tape frame can be peeled off easily once the membrane has been stuck on the substrate. This modified dry transfer method for ultra-large graphene-PMMA membrane has been conducted with 95 % success rate over 20 samples.

The graphene-PMMA closed cavity resonator has been characterized by: white light interferometry (WLI, Zygo), Polytec laser Doppler Vibrometer (LDV) and Raman Spectroscopy (inVia Renishaw). The static deformation is measured by WLI. Additionally, the dynamic behaviour actuated mechanically, acoustically and electro-thermally, is detected by the LDV. The presence of graphene is studied by Raman Spectroscopy.

4.1.4 Results and discussion

Static deformation

From the WLI measurements, the graphene-PMMA membrane has been found to deform by around 180 nm after it has been transferred over the closed cavity.

The three-dimensional image of the graphene-PMMA membrane suspended over the substrate is shown in Figure 4.3 (a). As the cross section over the membrane's diameter has been illustrated in Figure 4.3 (b), the static deformation of the membrane has been measured to be around 180 nm. The membrane's static deformation aspect ratio (the membrane's diameter over the membrane's static deformation) is about 19,500. The static measurement indicates the surface static deformation is extremely small when using the Kapton tape frame dry transfer method to transfer ultra-large graphene-PMMA membrane over the closed cavity

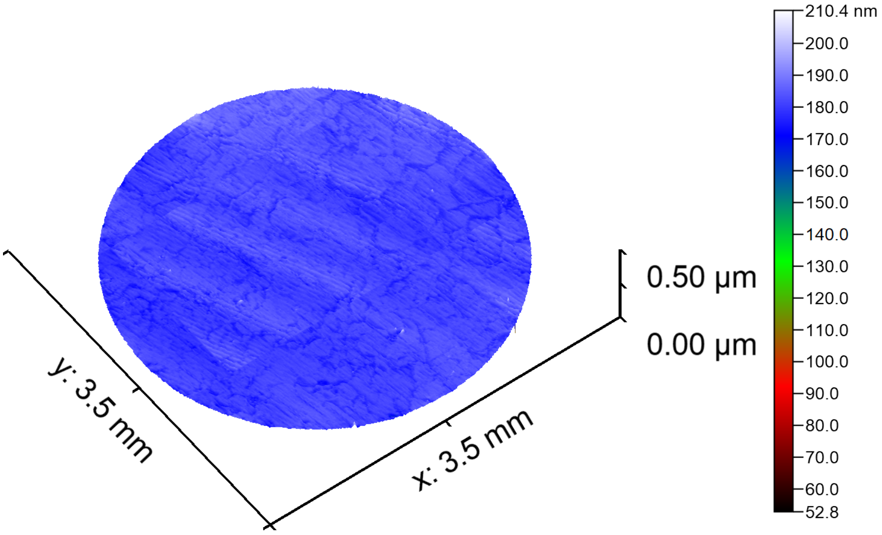

(a)

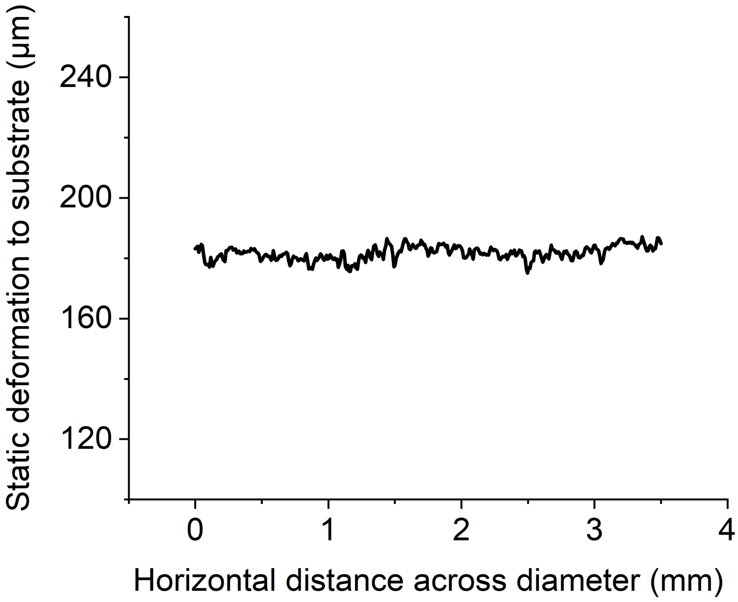

(b)

Figure 4.3: The static measurement with WLI: (a) the topography and (b) the cross section of the graphene-PMMA membrane over the diameter.

resonator [1].

Dynamic actuation

The dynamic behaviour has been performed by actuating the graphene-PMMA membrane over the closed cavity by a sweep of sine wave, mechanically, acoustically, and electro-thermally. For the mechanical actuation: the graphene-PMMA closed cavity resonator has been placed on the piezoelectric disk. The disk has been actuated by a sweep of AC voltage from 0.1 V to 2 V. For acoustic actuation: a speaker has been placed next to the graphene-PMMA closed cavity resonator. The sound pressure (sound volume) has been changed from 0.002 Pa (40 dB) to 0.04 Pa (66 dB). For the electro-thermal actuation: silver paste has been attached on the two sides of the membrane edge, serving as two electrodes. The input voltage to electrodes connected to the membrane is held constant at 1 V DC while AC voltage is varied from 1 V to 9 V. Using different actuation methods, the resonant frequency of the graphene-PMMA membrane over closed cavity is detected to be around 10.58 kHz ±10%, which is within the audio frequency range. The membrane is measured to exhibit the (1, 1) mode at the resonant frequency.

Mechanical actuation The frequency response of the graphene-PMMA membrane actuated mechanically is shown in Figure 4.4 (a). As the input AC voltage to the piezo-electric disk increases from 0.1 V to 2 V, the displacement amplitude of the graphene-PMMA membrane over the closed cavity at 11.72 kHz has been observed to rise from 12.6 nm to 237.3 nm. Around the membrane′s resonant frequency at 11.72 kHz, other peaks, at about 6 kHz and 8 kHz are observed. This is probably due to the noise caused by the piezo-disk since the peaks at the

---

[1] Considering the thickness of the membrane has been measured to be around 450 nm, the membrane has been estimated to be 270 nm deformed towards the ground. For the open cavity structure, deformation would be occurred during the graphene wet transfer process, the surface tension of DI water and the combined effect of membrane's gravity

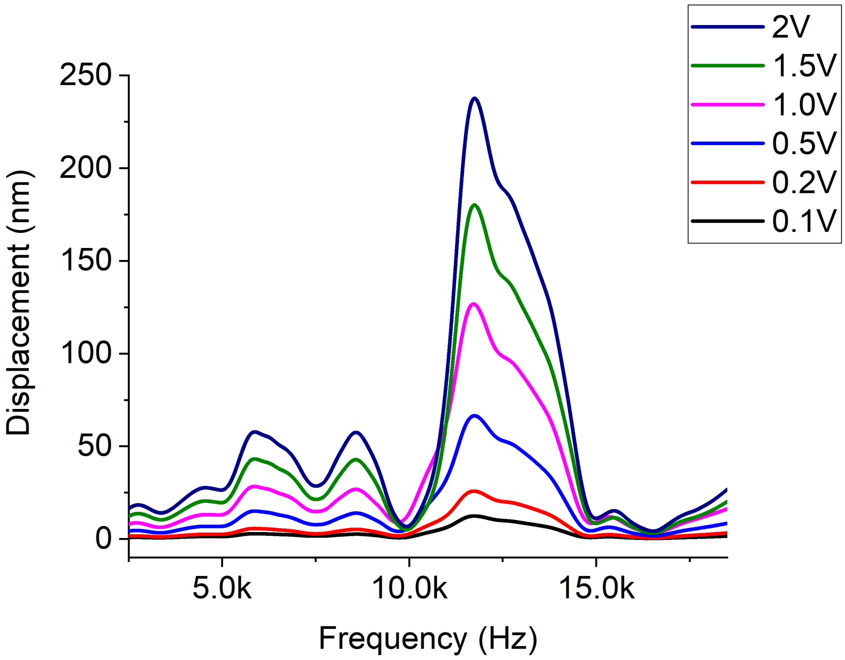

(a)

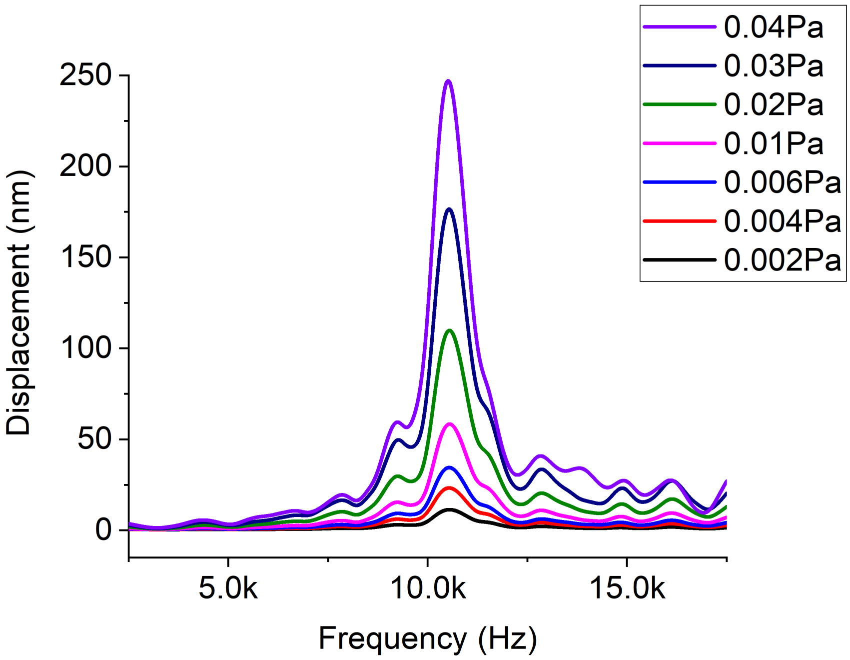

(b)

Figure 4.4: Continued

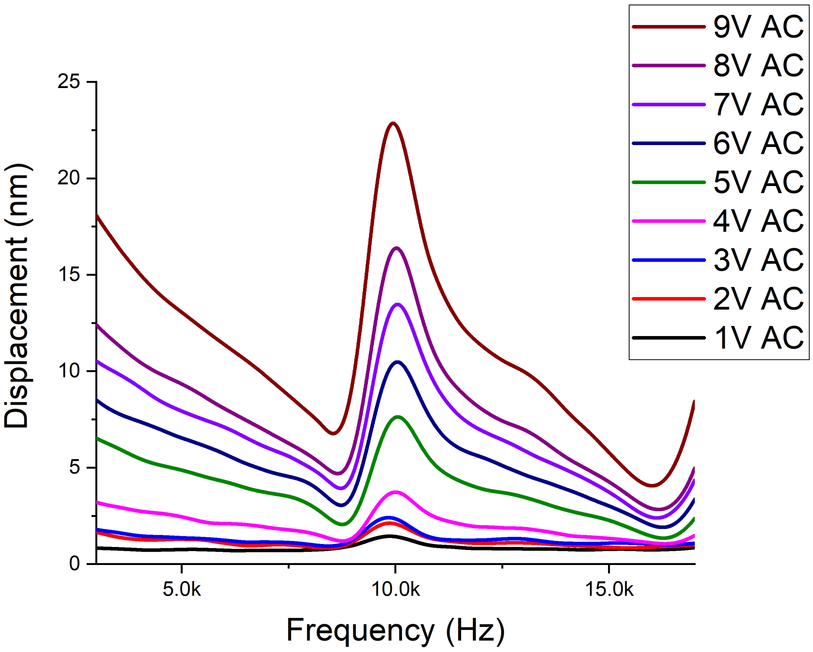

(c)

Figure 4.4: The frequency response measured at (a) mechanical actuation with input AC voltage from 0.1 V to 2 V; (b) acoustic actuation with sound pressure from 0.002 Pa to 0.04 Pa; (c) electro-thermal actuation with AC input voltage from 1 V to 9 V and constant 1 V DC voltage.

frequencies around 6 kHz and 8 kHz disappear when the membrane is actuated acoustically and electro-thermally, as shown in Figure 4.4 (b) and Figure 4.4 (c). The results from the mechanical actuation illustrate that the graphene-PMMA membrane over closed cavity is changing by varying the mechanical pressure.

Acoustic actuation The graphene-PMMA membrane's frequency response, to increasing sound pressure from 0.002 Pa (40 dB) to 0.04 Pa (66 dB) has been measured. Figure 4.4 (b) shows that the resonant displacement of the membrane increases with the sound pressure. The displacement rises from 13.3 nm to 246.8 nm with increase of the sound pressure. 10.58 kHz is the resonant frequency observed for the graphene-PMMA membrane over closed cavity by acoustic actuation. The acoustic actuation measurement shows that the graphene-PMMA membrane over the suspended cavity is sensitive to sound pressure.

Electro-thermal actuation The electro-thermal actuation experiment is conducted by keeping constant 1 V DC voltage and changing AC voltage from 1 V to 9 V. As shown in Figure 4.4 (c), the displacement of membrane increases from 1.4 nm to 21.6 nm with increasing AC input. The resonant frequency is detected to be around 10 kHz.

From the frequency response measurement, the quality factor of the membrane has been estimated to be 6.63 $\pm 0.05\%$, 13.78 $\pm 0.01\%$ and 7.51 $\pm 0.05\%$ under mechanical, acoustic and electro-thermal actuation respectively.

Sensitivity of vibration amplitude

The sensitivity of the vibration amplitude has been calculated by fitting the resonant displacement of the membrane versus the input signal. As shown in Figure 4.5, the black squares represent the experimental results and the red dash lines correspond to the fitting. In the case of mechanical and acoustical actuation, the vibration amplitude has been observed to be linear with the input signal. For the electro-thermal actuation, the vibration amplitude shows a quadratic relation with the input AC voltage.

In the case of electro-thermal actuation, the current goes through the membrane and generates heating in the graphene-PMMA membrane. The vibration of the membrane is introduced by thermal stress due to Joule Heating. The displacement is proportional to the thermal stress and therefore can be derived in the quadratic relationship with input voltage [116, 117]. The relationship between the thermal stress and input voltage has been confirmed by simulations (see section E).

As shown in Table 3.1, the vibration amplitude sensitivity of the graphene-PMMA membrane over the closed cavity is calculated to be around 120 nm/V by mechanical actuation, 6 μm/Pa by acoustic actuation and 0.3 nm/V^2 by electro-thermal actuation.

The membrane's high sensitivity by acoustic actuation indicates the potential of applying graphene-PMMA membrane over the closed cavity resonator to high sensitivity condenser microphone and loudspeaker.

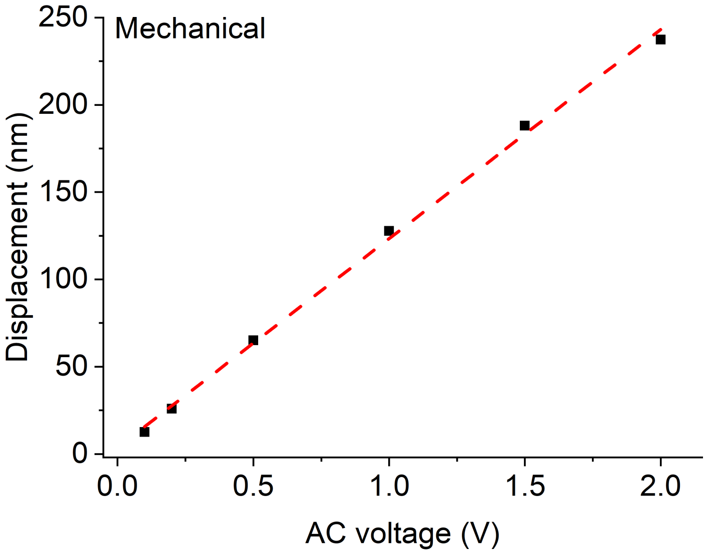

(a)

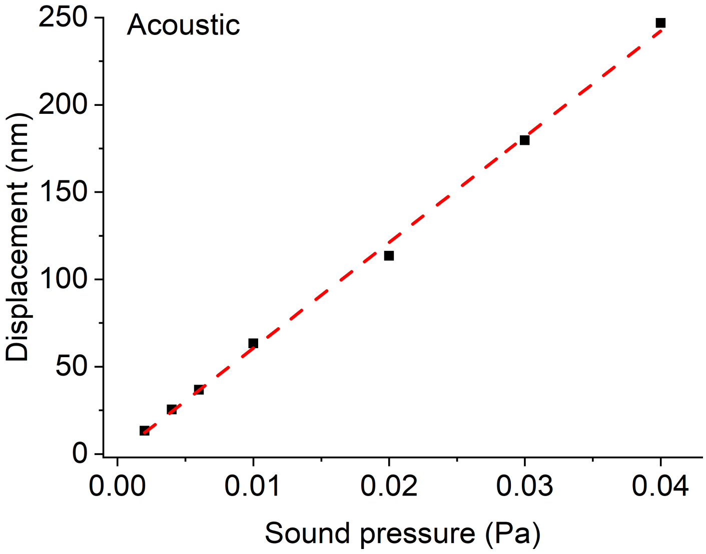

(b)

Figure 4.5: Continued

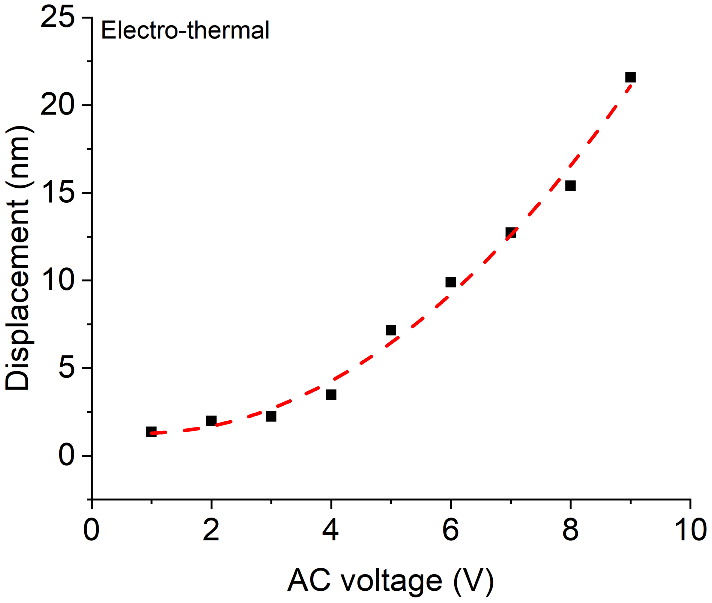

(c)

Figure 4.5: The resonant displacement vibration amplitude sensitivity versus (a) mechanical actuation with input AC voltage from 0.1 V to 2 V; (b) acoustic actuation with sound pressure from 0.002 Pa to 0.04 Pa; (c) electro-thermal actuation with AC input voltage from 1 V to 9 V and constant 1 V DC voltage.

Table 4.1: Sensitivity of vibration amplitude

Actuation methods	*Varying input signal range*	*Measured resonant frequency*	*Sensitivity of vibration amplitude*
Mechanical	0.1 V to 2 V AC	11.72 kHz	119.74 nm/V
Acoustic	0.0002 Pa to 0.04 Pa	10.58 kHz	6.06 μm/Pa
Electro-thermal	1V to 9 V AC	10.01 kHz	0.3 nm/V^2

Mode shape

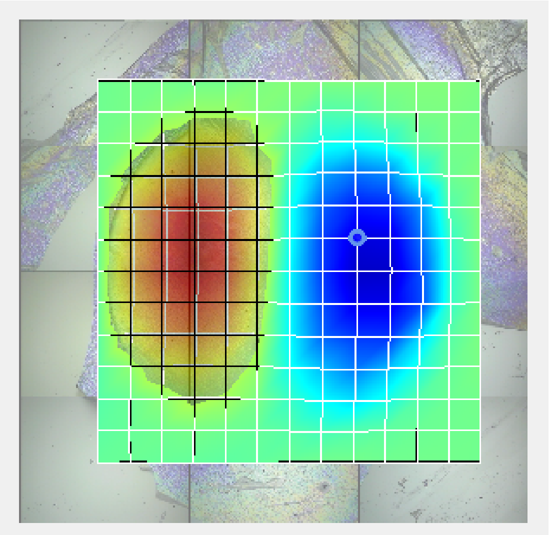

(a)

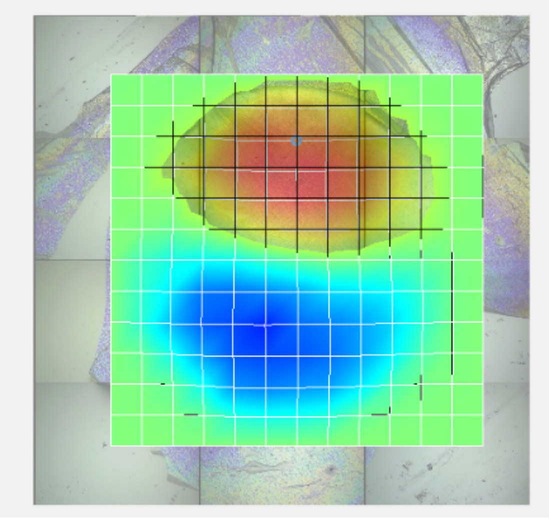

(b)

Figure 4.6: Continued

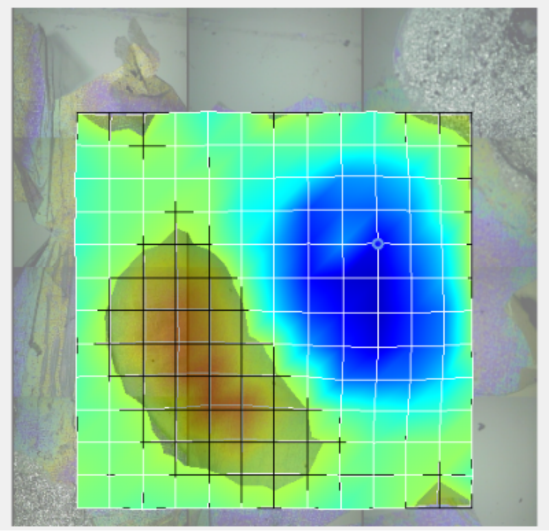

(c)

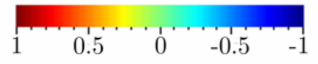

scale bar

Figure 4.6: The (1, 1) mode shape of the membrane over closed cavity substrate on resonant frequency actuated: (a) mechanically with 0.1 V AC; (b) by 40 dB sound pressure; (c) electro-thermally with 1 V AC and 1 V DC.

Figure 4.6 shows the graphene-PMMA membrane mode shapes at the resonant frequency under the three different types of actuation methods. Figure 4.6 (a) to c illustrate the mode shapes of the same membrane suspended over the closed cavity under the mechanical (0.1 V AC), acoustic (0.002 Pa/40 dB) and electro-thermal (1 V AC and 1 V DC) actuation respectively. From the mode shapes shown in Figure 4.6, it can be seen that the (1, 1) mode of the graphene-PMMA membrane has been actuated and dominates the frequency response in the closed cavity. Unlike the open cavity device, where the (0, 1) mode resonance dominates [105], and the air could flow freely through the open hole, in the case of graphene-PMMA closed cavity resonator, the impermeability of the graphene layer [118] and the closed cavity substrate seal the air inside the closed cavity. The change of gas volume inside the closed cavity is too small to support the relatively large membrane movement needed to generate the large volume change in the (0, 1) resonant mode. Therefore, in the graphene-PMMA closed cavity resonator where gas encapsulation is good, and hence only small gas volume changes, the observed (1, 1) mode resonance is dominant.

In addition, the orientation of the mode shape has been observed to change depending on the actuation methods. For mechanical actuation, the orientation has been observed to be determined by the position of the piezo-disk; for the acoustic actuation, the orientation has been detected to vary with the position of the speaker and for the electro-thermal actuation, the mode shape orientation changes with the position of the electrodes.

In order to achieve the resonance of the ultra-large graphene-PMMA membrane suspended over the closed cavity, an optimized [2] air gap distance of 220 μm has been found. In the investigation of the relationship between the air gap distance and the dynamic behavior of the membrane over the closed cavity, the resonance for the acoustic frequency range of the graphene-PMMA membrane over the closed cavity could not be observed when the air gap distance has been decreased. The disappearance of the resonance in the closed cavity device with smaller air gap distance might be due to damping effects [67,118]. Our observation suggests that in the previously reported graphene-based microphone designs [87, 89, 90, 114, 115], there might be the presence of air leaking in the connection between devices' substrates and the graphene-based membranes attached on the supporting frames.

Simulations

Finite element analysis (FEA) simulations of the device under mechanical and electro-thermal actuation have been performed with Coventorware 10, in order to investigate the relationship between the actuation stress and the input signal. To simulate mechanical actuation, pressure from 0.01 Pa to 0.1 Pa has been applied

---

[2] The resonance has not been observed at the frequency range from 20 kHz to 100 kHz in closed cavity designs where the air gap has been less than 150 µm. The threshold air gap when the resonance would occur has been not investigated. Further investigation on relationship between air gap and the dynamic behavior of graphene-based membranes should be performed.

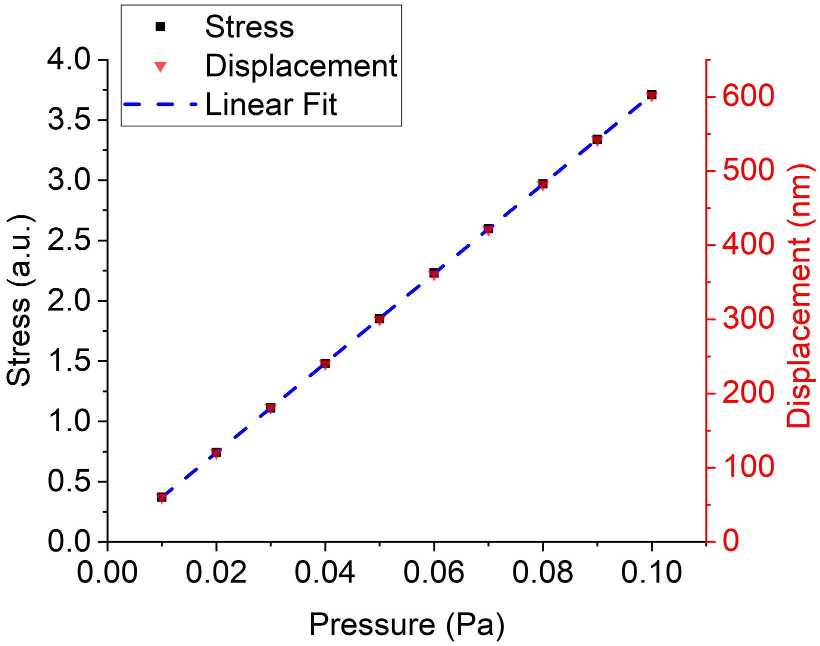

(d)

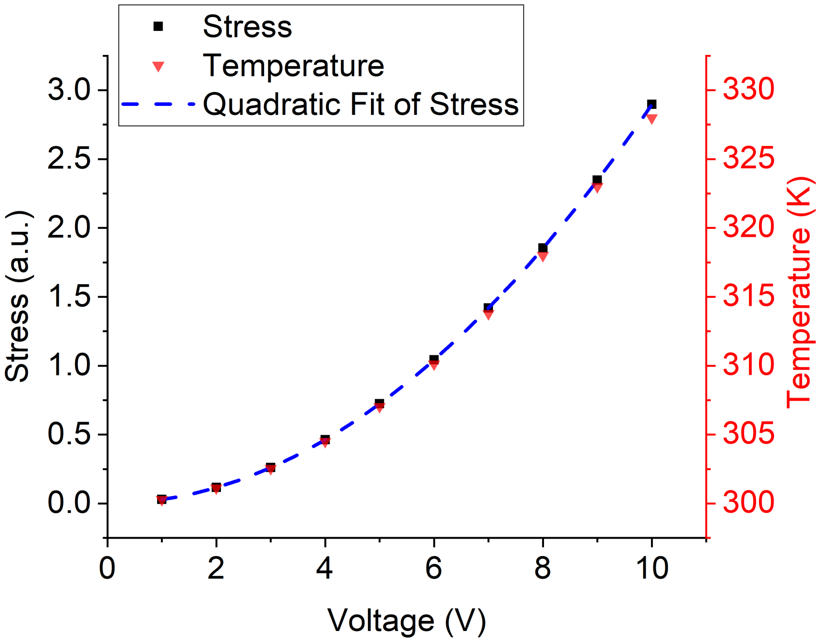

(e)

Figure 4.7: Continued

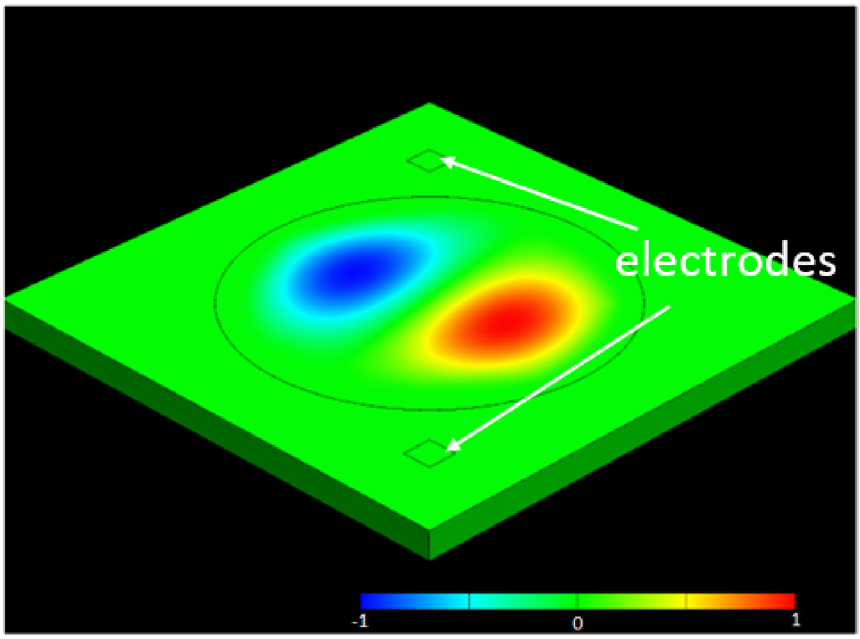

(f)

Figure 4.7: FEA simulations: (a) Simulated stress (black square) and displacement (red triangle) of the membrane versus input pressure; (b) simulated thermal stress (black square) and temperature (red triangle) of the membrane with respect to input voltage; (c) simulated mode shape of the membrane under the mechanical and electro-thermal actuation.

on the bottom surface of the silicon substrate. As shown in Figure 4.7 (a), the stress and displacement of the graphene-PMMA membrane a linear relationship with the input pressure and is consistent with the measured results. In the case of electro-thermal actuation, voltages from 1 V to 10 V have been applied to the electrodes. As Figure 4.7(b) illustrates, the thermal actuation stress over the membrane has a quadratic relationship with the input voltage for electro-thermal actuation. The temperature increase as a function of input voltage has also been plotted. As the displacement is proportional to the thermal stress, the simulations confirm the experimental results. Figure 4.7 (c) shows that the graphene-PMMA membrane suspended over the closed cavity has been observed to be under (1, 1) mode for both the mechanical and electro-thermal actuation.

Strain analysis

In addition to the actuation stress derived from simulations, the strain, including built-in strain and actuation strain, in the graphene-PMMA membrane over the closed cavity has been estimated from both the experimentally measured resonant frequency and Raman shift.

The strain can be deduced from the measured resonant frequency using

$$A_{\mathrm{m}} = \frac{\rho_{\mathrm{air}} R}{3\rho_{\mathrm{eff}} t_{\mathrm{eff}}}, \tag{4.2}$$

$$f_{\mathrm{mn}} = \frac{\beta_{\mathrm{mn}}}{2\pi R}\sqrt{\frac{N_{\mathrm{i}} + N_{\mathrm{a}}}{\rho_{\mathrm{eff}} t_{\mathrm{eff}} (1 + A_{\mathrm{m}})}}, \tag{4.3}$$

where ρ_{air} is the air density, A_{m} is the air mass, N_{i} and N_{a} represent the built-in tension and the tension caused by the dynamic actuation.

The tension and strain of the graphene-PMMA membrane have been calculated with Equation (4.3) [105]. The air mass is considered, since the resonance measurement of the sample has been conducted in air medium [119]. As shown in Table 4.2, the tension ($N_\mathrm{i} + N_\mathrm{a}$) and strain of the graphene-PMMA membrane by the three actuation methods have been calculated. As the actuated tension changes with different actuation methods, the measured resonant frequencies vary.

Table 4.2: Overall tension ($N_\mathrm{i} + N_\mathrm{a}$) and strain in the graphene-PMMA membrane deducted from the measured resonant frequency

Actuation methods	*Measured resonant frequency* (kHz)	*Tension* (N/m)	*Strain* (%)
Mechanical	11.72	2.09	0.057
Acoustic	10.58	1.74	0.046
Electro-thermal	10.01	1.53	0.041

Raman spectroscopy

Table 4.3: Positions and full width at half maximum (FWHM) of the G and 2D peaks.

	G		2D	
	position (cm^{-1})	FWHM (cm^{-1})	position (cm^{-1})	FWHM (cm^{-1})
Center	1589.7	23.2	2693.4	39.24
Substrate	1592.5	27.01	2703.4	35.03

Raman spectroscopy measurement has been taken on the suspended membrane′s center and with the membrane on the substrate respectively, using 0.8 mW laser power, with laser excitation of 514.5 nm and a 100x objective. The experiment has been conducted on four different and random points around the suspended graphene-PMMA membrane's center and on the membrane stuck on the substrate respectively. The Raman spectrum observed from the selected points have been consistent. Figure 4.8 shows the Raman spectrum of the graphene-PMMA closed

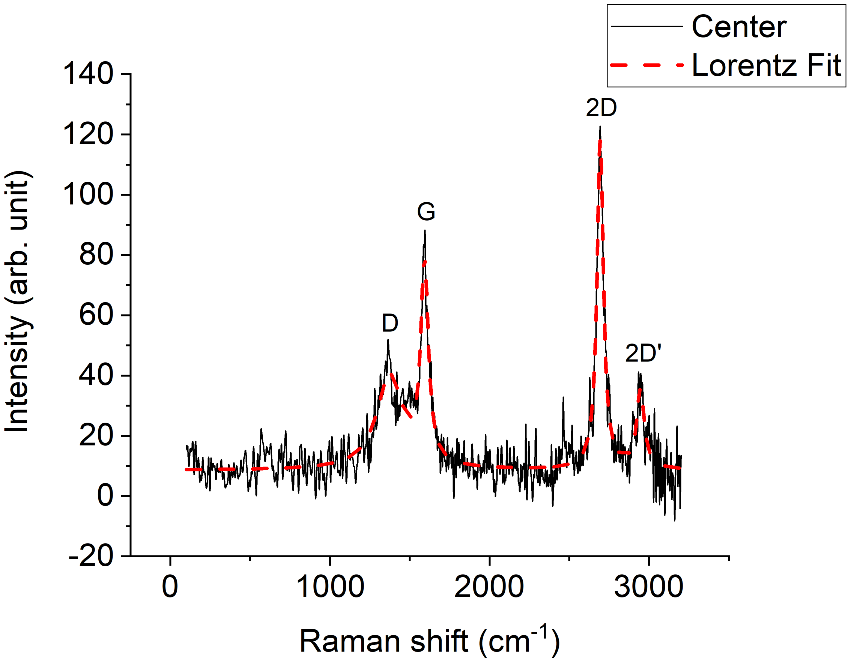

(a)

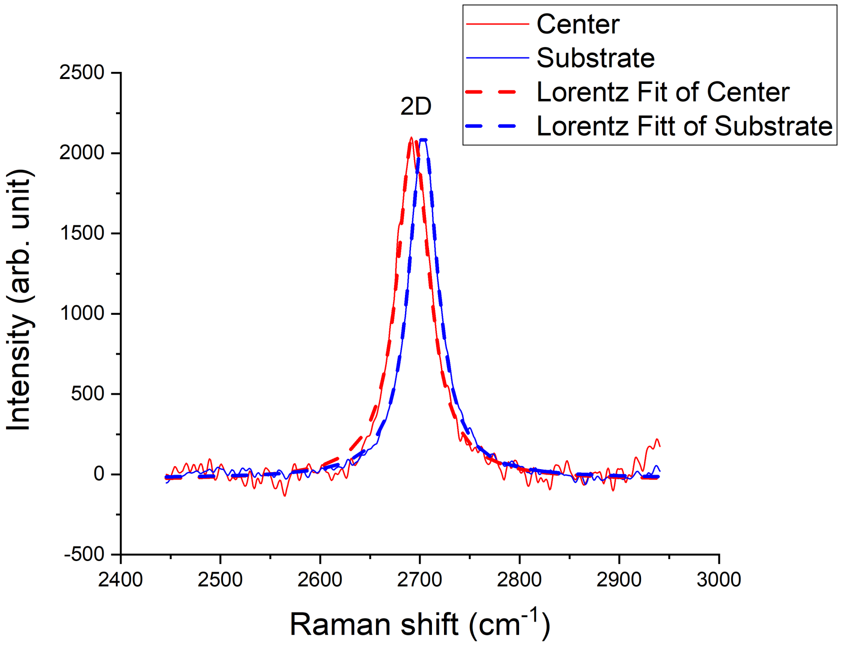

(b)

Figure 4.8: Continued

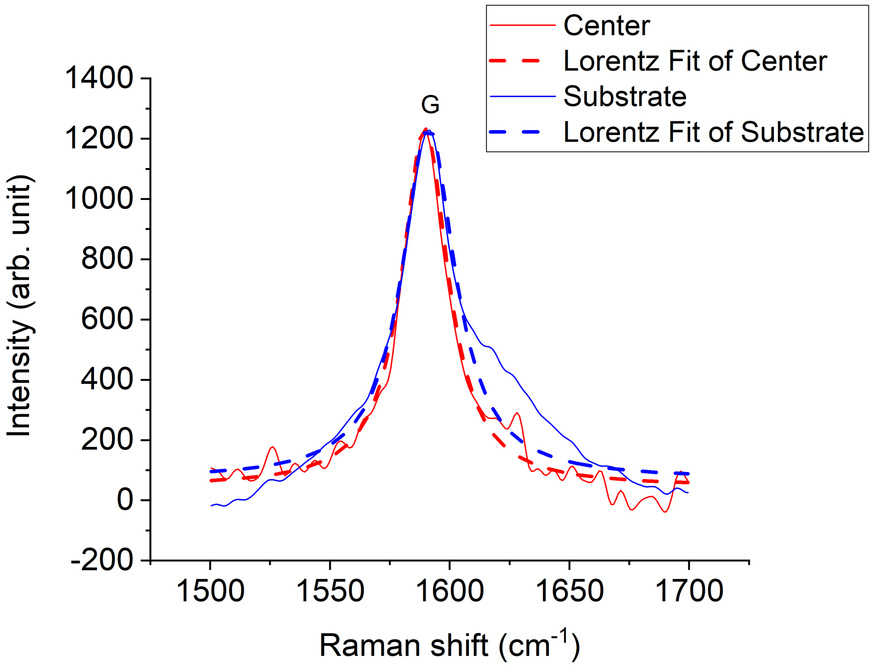

(c)

Figure 4.8: The Raman spectrum of the graphene-PMMA closed cavity resonator: (a) full scan of the Raman spectrum at the center of the suspended membrane; (b) 2D peak position shift of suspended membrane′s center (red) and the membrane stuck on the substrate (blue); (c) G peak position shift of suspended membrane's center (red) and the membrane stuck on the substrate (blue).

cavity resonator. The dash lines represent plots of the Lorentz Fitting. Figure 4.8 (a) illustrates the appearance of the D peak, G peak, 2D peak and 2D′peak, which shows the graphene-PMMA membrane is suspended over the closed cavity when using the Kapton tape dry transfer method. The narrow shape of G peak and 2D peak indicates that the graphene film is between 5 to 10 layers [120], which agrees with the fact that the graphene on copper foil is 6 layers before transfer. The intensity ratio between D peak and G peak has been estimated to be 0.51, which indicates, the graphene sample is defected [120]. However, from visual inspection, no large scale defects have been found. The appearance of D peak in the suspended structure of graphene might be due to structural disorder [121,122]. Figure 4.8 (b) and Figure 4.8 (c) show the Raman shift of 2D peak and G peak between the graphene-PMMA membrane suspended over the closed cavity and stuck on the substrate. As Table 4.3 shows, compared to the membrane on the substrate, 2D peak and G peak of suspended membrane′s center have been detected to shift by 10.0 cm^{-1} and 2.8 cm^{-1}. The shift of the 2D peak and G peak positions related to biaxial tensile strain in graphene has been measured to be -77 ± 7 $cm^{-1}/\%$ and -203 ± 20 $cm^{-1}/\%$, in the previous work [123]. With the Raman shift, the strain of the suspended graphene-PMMA membrane is estimated to be 0.04 $\pm 0.01\%$.

In the case of the electro-thermal actuation, the strain, which is deduced from the resonant frequency, in the graphene-PMMA membrane is the smallest amongst the three different actuation methods. The value of the strain in the graphene-PMMA membrane with electro-thermal actuation drops by about 24 % compared to other two actuation methods. The observation might be due to the strain softening generated by Joule Heating.

The bi-axial tensile strain estimated from the Raman shift is associated only with the built-in tension (N_{i}). The tensile strain deduced from resonant frequency is related to both the built-in tension (N_{i}) and actuation tension (N_{a}). The value of the strain in the membrane deduced from the measured resonant frequency and the one calculated from the Raman shift is similar, which suggests that the built-in tension dominates the overall in-plane tension in the three actuation methods. Therefore, the overall strain in the graphene based membrane suspended over the closed cavity, is estimated to be 0.04 $\pm 0.01\%$.

Finally, Table 4.4 shows a comparison of our work to other research on graphene-based acoustic sensors.

4.1.5 Conclusions

In summary, it is the first time that an ultra large area graphene-PMMA closed cavity resonator has been fabricated and actuated successfully. The ultra-large graphene-PMMA membrane has been dry transferred using Kapton tape as a supporting frame. The modified dry transfer method has been tested with about 95 % percentage yield over 20 samples. Raman spectrum confirms that the ultra large graphene membrane has been transferred safely using the modified graphene dry transfer method. The WLI results indicate that the dry transfer method can be used to transfer graphene-PMMA membrane over the large area closed cavity with small static deformation. The fact that (1, 1) mode resonant frequency dominates, suggests gas encapsulation is good in comparison to open cavity designs with the same suspended graphene-PMMA membrane size, in which the (0, 1) mode frequency is dominant. Furthermore, the frequency response of the graphene-PMMA membrane suspended on closed cavity resonator actuated mechanically, acoustically and electro-thermally, has been characterized in this work. In agreement with the experimental results, FEA simulations have shown that the membrane's displacement and stress during actuation vary linearly as a function of either the applied mechanical force or the applied acoustic pressure. Similarly, the quadratic relationship between the electro-thermal actuation voltage and the stress has been confirmed with FEA simulations. The overall strain in the graphene-PMMA membrane suspended over the closed cavity is

Table 4.4: Comparison of our work to other research on graphene-based acoustic sensors

	Graphene layers number	PMMA thickness	Overall membrane thickness	Aspect ratio	Fabrication process	Actuation method	Sensitivity	Resonant frequency
This work	6	450 nm	452 nm	7800	One step	Mechanical, acoustic and electro-thermal	**Mechanical**: 119.74 nm/V; **Acoustic**: 6.06 μm/Pa; **Electro-thermal**: 0.3 nm/V^2;	Around 10 k
[87]	75	0 nm	25 nm	350,000	With supporting frame and manual assemble method	Acoustic	-70 dBV	N/A
[114]	1800	1 μm	1.2 μm	3400	With supporting frame and manual assemble method	Acoustic	-20 dBV	3.2K
Our work [89]	5	198 nm	200 nm	15,000	With supporting frame and manual assemble method	Acoustic	-40 dBV	N/A
Our work [83]	8	370 nm	373 nm	9,400	Wet transfer on open cavity	Electro-thermal	3.4 nm/V	4k

estimated to be 0.04 ±0.01%. The metric acoustic vibration amplitude sensitivity of the multilayer graphene-PMMA membrane over the closed cavity indicates the promise of achieving high quality graphene-PMMA microphones with high sensitivity.

4.2 For ultrasound sensing

4.2.1 Introduction

In this work, a fully clamped graphene/PMMA closed cavity resonator for ultrasonic detection will be presented. To avoid the membrane being transferred on the supporting ring and assembled onto the substrate afterwards, a one-step graphene dry transfer process, has been developed by our group[124]. The 6-layer graphene reinforced by 450 nm thick PMMA has been transferred directly onto the substrate and suspended fully over a closed circular cavity with a diameter of 0.5 mm and formed an air gap of 105 μm. The thin PMMA layer functions not only as the attachment between the graphene and the anchor of the substrate but also the supporting layer for the graphene to be suspended over the closed cavity. The air gap of 105 μm has been designed to minimize the effect of air damping. Two devices have been fabricated with the success rate of 100% and with this fabrication method, decrease the complexity of fabricating closed cavity samples. As mention in previous section, the success rate of modified dry transfer method to fabricate closed cavity resonator has been over 95%. The sensor has been actuated mechanically, electro-statically and electro-thermally in atmosphere. It is the first time that the dynamic resonant characteristics of the graphene/PMMA closed cavity resonator for ultrasound detection have been determined.

4.2.2 Materials and methods

The optical image of the graphene/PMMA ultrasonic closed cavity resonator is shown in Figure 4.9.a. The graphene/PMMA membrane has been transferred onto the silicon dioxide on silicon substrate with the closed cavity, of which an air gap has been designed to be 105 μm. The squares at the corners of the chip have been patterned and etched into silicon to serve as electrodes. As the cross-section schematic of the device shown in Figure 4.9.b, an air gap of 105 μm has been formed by the suspended membrane and the silicon substrate, which has been measured by Leica 150x optical microscope. The capacitance between the membrane and the substate has been calculated to be 16.5 fF. The graphene/PMMA membrane and the silicon substrate work as two plates for the capacitive structure. The natural frequency formula for the graphene/PMMA membrane can be determined by Equation (4.2)

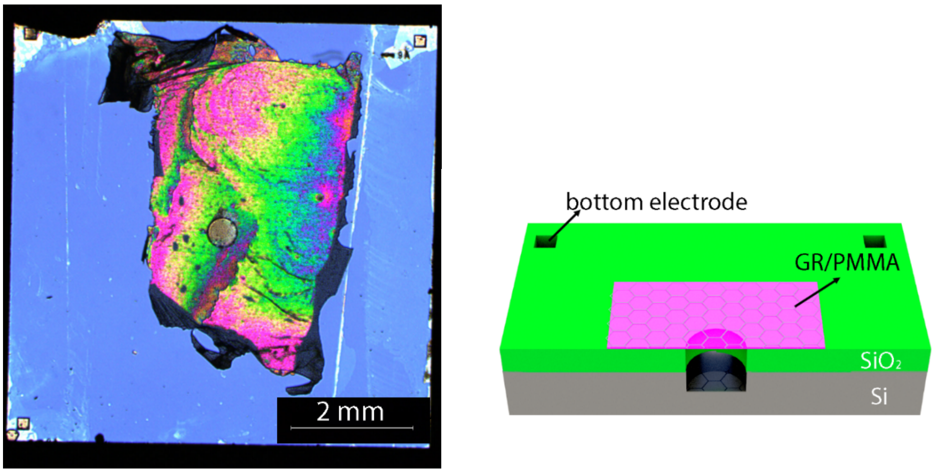

(a) (b)

Figure 4.9: The optical image (a) and cross-section schematic (b) of the closed cavity resonator with 105 µm gap.

The fabrication process of the graphene/PMMA closed cavity ultrasonic sensor has been shown in Figure 4.10. The preparation of the device's substrate has been shown in Figure 4.10.i & ii, the 500 nm silicon dioxide has been deposited onto the silicon substrate. The circular cavity with the diameter of 500 μm, together with three square holes with 100 μm width that serve as electrodes have

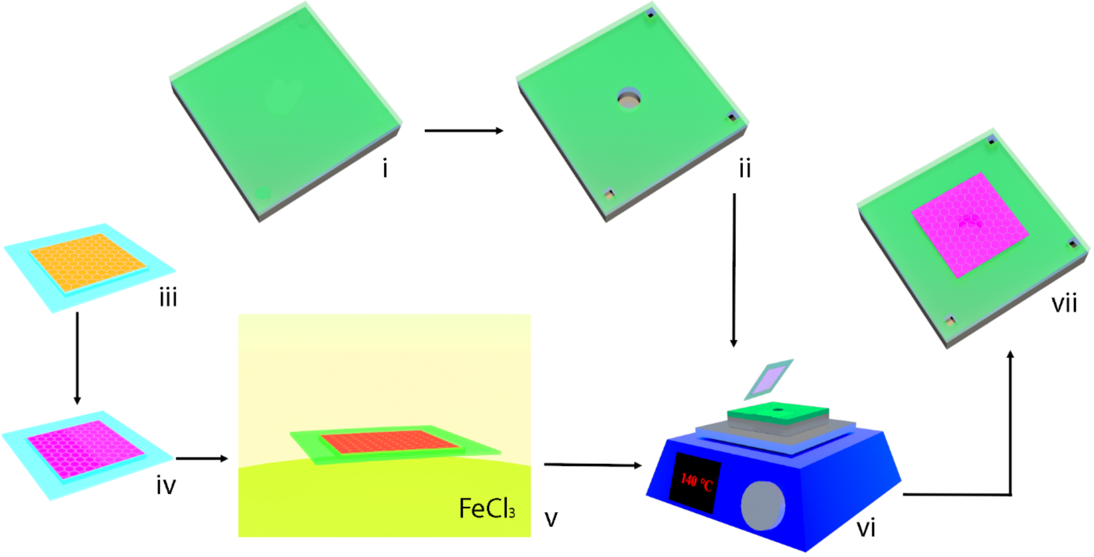

(a)

Figure 4.10: The fabrication schematic of the graphene/PMMA closed cavity ultrasonic sensor. The preparation of the substrate: (i) 500 nm silicon dioxide deposited on the silicon; (ii) the cavity and the electrodes patterned and etched into the silicon; The preparation of the graphene/PMMA membrane: (iii) the Kapton tape frame attached on the copper CVD graphene; (iv) PMMA spin-coated on the CVD graphene; (v) the copper foil etched by ferric chloride; The dry transfer of the graphene/PMMA membrane: (vi) graphene/PMMA membrane dry transferred on the substrate at the temperature of 140°C; (vii) the device cooled down in the air.

been patterned and etched into the silicon dioxide and silicon. The preparation and dry transfer of the graphene/PMMA membrane onto the substrate using Kapton tape as frame: (iii) the Kapton tape frame attached on the copper CVD graphene; (iv) PMMA spin-coated on the CVD graphene; (v) the copper foil etched by ferric chloride; The dry transfer of the graphene/PMMA membrane: (vi) graphene/PMMA membrane dry transferred on the substrate and the Kapton tape frame peeled off from membrane at the temperature of 140°C; (vii) the device cooled down in the air.

4.2.3 Results and discussion

Dynamic actuation

The graphene/PMMA ultrasonic resonator has been actuated mechanically, electrostatically and electro-thermally to characterise its dynamic behaviour. For the mechanical actuation, the graphene/PMMA ultrasonic resonator has been placed on the piezoelectric disk. The ultrasound vibration has been actuated by the voltage applied to the piezo-disk. For the electro-static actuation, silver paste has been attached on the graphene layer to work as the top electrodes. The patterns etched into the silicon with the resistivity of 1-10 Ωcm has been used as the bottom electrodes. The electro-static stress between the graphene membrane and the substrate has been generated by the voltage applied to the top and bottom electrodes. For the electro-thermal actuation, the thermal expansion of the membrane has been actuated by the voltage applied to the silver paste on the graphene layer. The dynamic characteristics have been measured by Polytec Laser Doppler Vibrometer (LDV). In addition to actuating the resonator by the signal with the frequency sweep, the sine-function signal of the membrane's resonant frequency has also been applied in order to provide the larger response time for the membrane to be actuated and to improve the accuracy of the displacement of the membrane which has been measured. All the measurements have been conducted on one device at room temperature and in atmosphere.

Mechanical actuation For mechanical actuation, the varying AC voltage from 0.2 V to 3 V and constant 1 V DC voltage with the frequency sweep from 150 kHz to 220 kHz has been applied to the piezo-disk. The frequency response of the membrane has been shown in Figure 4.11.a. The resonant frequency of the membrane has been measured to be around 163.15 kHz ±0.2 % with a side band of around 169.487 kHz. The side band can be explained by the coupling between the membrane and substrate. The frequency peak at around 169 kHz has been observed with the graphene/PMMA membrane stuck on the silicon dioxide substrate anchor. The amplitude of the graphene/PMMA at the resonant frequency of around 163 kHz has been measured to be 0.05 nm to 1 nm. The frequency response measured under the frequency sweep at 0.1 V AC and 0.2 V AC seems to be similar, which is due to the response time at an ultrasonic frequency of around 163 kHz being too small for the membrane actuated at the lower AC voltages to respond and reach its maximum value. The quality factor at the resonant frequency has been estimated to be 49.45 ±6.8 %.

Electro-static actuation For electro-thermal actuation, the voltage of constant 1 V DC and varying AC voltage from 4V and 9V with frequency sweep between 120 kHz to 200 kHz have been applied between the membrane and substrate. The frequency response of the graphene/PMMA membrane has been shown in Figure 4.11.b. The resonant frequency has been measured to be 158.337 kHz ±0.4 % with the side band observed at 169.265 kHz. The side band can also be related to the coupling between the membrane and substrate. Like the mechanical actuation, the actuation stress (electro-static stress) has been vertical to the membrane. In addition, the side band frequency at the electro-static actuation has been observed to be similar to the side band frequency observed from the mechanical actuation (Figure 4.11.a). The displacement of the membrane actuated from 4 V to 9 V from the electro-thermal actuation has been measured to be between 0.64 pm to 1.45 pm. The possible explanation of the small amplitude measured in the frequency sweep is the air gap of around 105 μm, which forms a small capacitance between the membrane and substrate. The quality factor has been observed to be 25.64 ±5.8 % at the resonant frequency.

Electro-thermal actuation For electro-thermal actuation, the frequency response of the resonator actuated by increasing 1 V to 9 V AC and 1 V DC voltage applied to the silver paste on the graphene/PMMA membrane with the frequency range from 140 kHz to 220 kHz, has been illustrated in Figure 4.11.c. The resonant frequency has been observed to be around 158.965 kHz ±1.9 % and with the side band of around 187.851 kHz. The side band has been generated by the transition between the (1,1) mode and (0,2) mode. Under the electro-thermal actuation, the membrane has been heated when the AC voltage has been applied and the transition between the (1,1) mode and (0,2) mode results from thermal stress over the membrane. The transition has not been observed in mechanical and electrostatic actuation. Instead, the side band of around 169 kHz, which has been detected in the other two actuations, has been related to the coupling between the membrane and substrate. Unlike the other two actuation methods where the actuation stress has been out-of-plane, in the case of electro-thermal actuation, the thermal expansion generated by the Joule heating has been in-plane. The in-plane actuation stress through the membrane might not generate the coupling between the membrane and substrate. Under the other two actuation methods, the coupling between the membrane and substrate dominates and the transition with smaller amplitude has not been observed. The displacement under electro-thermal actuation has been measured to be from 1.2 pm to 8.4 pm. At the resonant frequency, the quality factor has been detected to be 34.42 ±15.8 %.

Sensitivity of vibration amplitude

The vibration amplitude of graphene/PMMA membrane over the closed cavity has been shown in Figure 4.12. The membrane has been actuated by sinusoidal signal at the resonant frequencies corresponding to different actuation methods. The amplitude of the membrane has been observed to be linear with the increasing AC voltage under the mechanical actuation, as illustrated in Figure 4.12.a. The electrostatic force (F_{el}) between the suspended graphene membrane and the substrate:

$$F_{\mathrm{el}} \approx \frac{1}{2} C'_{\mathrm{g}} (V_{\mathrm{g}}^{\mathrm{dc}})^2 + C'_{\mathrm{g}} V_{\mathrm{g}}^{\mathrm{dc}} V_{\mathrm{g}}^{\mathrm{ac}}, \tag{4.4}$$

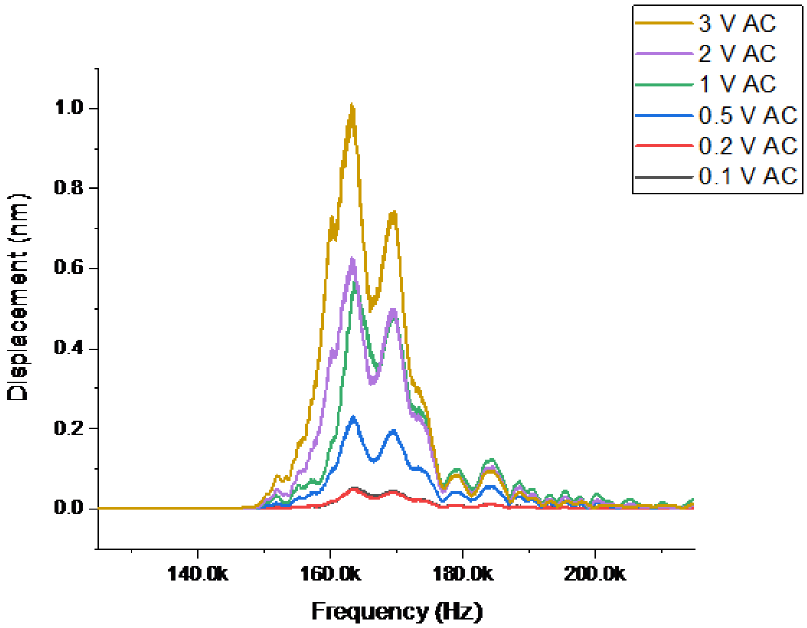

(a)

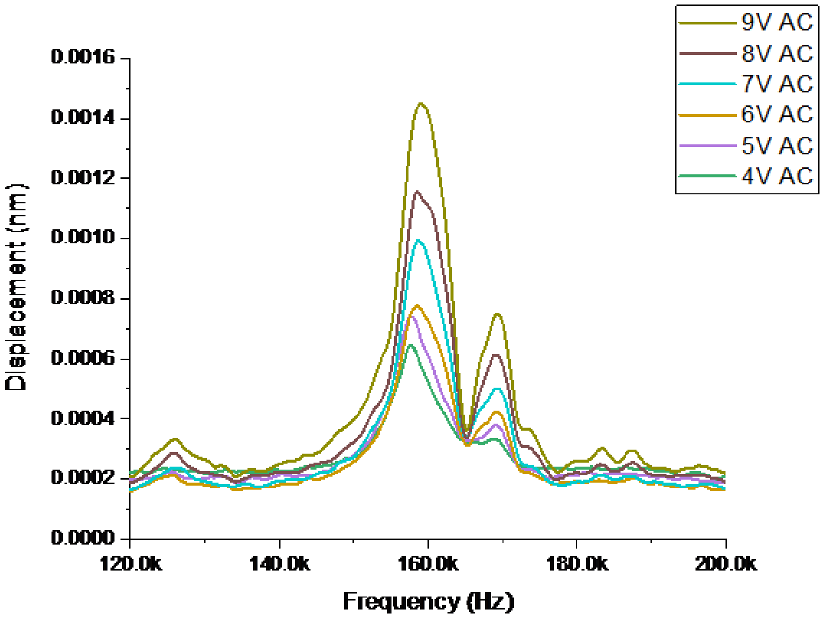

(b)

Figure 4.11: Continued

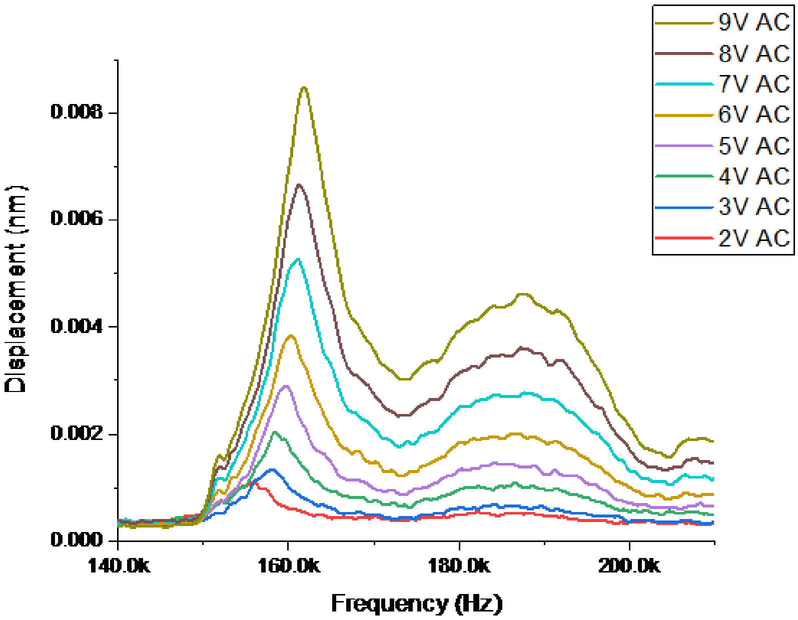

(c)

Figure 4.11: The frequency response of the membrane under: (a) mechanical actuation with the input voltage from 0.1 V to 3 V AC and 1 V DC as well as by the frequency sweep from 150 kHz to 220 kHz; (b) electro-static actuation with the voltage of constant 1 V DC voltage and varying AC from 4 V to 9V with the frequency sweep between 120 kHz and 200 kHz; (c) electro-thermal frequency sweep signal with 2-9 V AC and 1 V DC between 140 kHz and 210 kHz.

where C'_{g}represents the derivative of the capacitance between the graphene and substrate with respect to the air gap, $V_{\mathrm{g}}^{\mathrm{dc}}$ and $V_{\mathrm{g}}^{\mathrm{ac}}$ refer to the DC voltage and AC voltage applied to the membrane and substrate respectively.

Equation (4.4) [99] shows the linear relationship between the electrostatic force and AC voltage, with the assumption of constant DC voltage. As shown in Figure 4.12.b, derivations in the linear relation between the AC voltage and the membrane's displacement would be caused by the relatively large spacing between the membrane and substrate and air damping inside the closed cavity. The linear relation has been observed more evident in devices with smaller air gap (Figure 5.3 and Figure 5.7). In the case of the electro-thermal actuation, the graphene/PMMA membrane has been actuated by the thermal stress which has been generated by Joule heating. The thermal stress is linear with the Joule heating and thus is quadratic with the input AC voltage. As shown in Figure 4.12.c, the quadratic relation between the amplitude and input AC voltage from 1 V to 8 V has been observed. At a voltage of 9 V AC, the amplitude which has not been shown to fit with the parabola function is due to the membrane's resonant frequency being shifted by the increasing AC voltage. At 9 V AC, the resonant frequency of the membrane over the closed cavity has been measured to be 161.914 kHz, with the frequency shift of around 5 kHz away from the actuated sinusoidal signal at frequency of 156.914 kHz (Figure 4.12). The amplitude at the frequency with around 5 kHz shifted from the resonant frequency has been smaller than the amplitude measured at the resonant frequency.

The dynamic behavior of graphene/PMMA closed cavity ultrasonic sensor is summarized in Table 4.5. The measured resonant frequency has been observed to change with the actuation methods. In the cases of electro-static and electro-thermal actuation, the measured resonant frequency is smaller compared to the mechanical frequency, which can be due to capacitive softening[125–127] and electro-thermal softening[128].

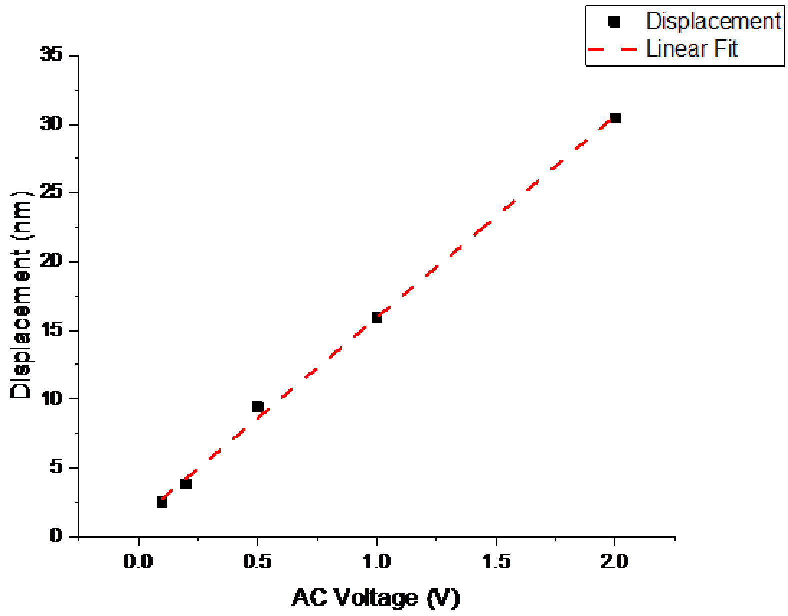

(a)

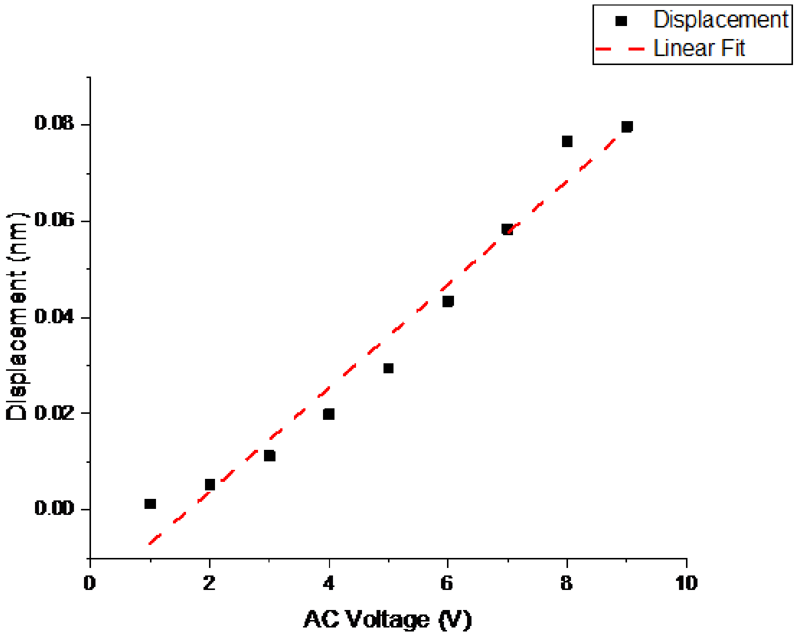

(b)

Figure 4.12: Continued

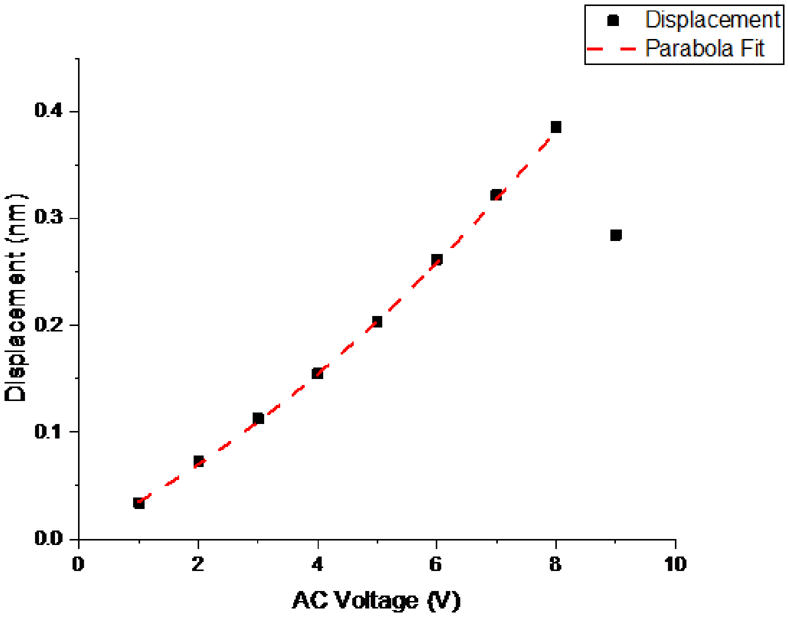

(c)

Figure 4.12: The amplitude of the membrane under: (a) mechanical actuation (0.1 V AC to 2 V AC and constant 1 V DC) at 163.156 kHz with linear fitting; (b) electro-static actuation at 158.64 kHz with signal of the AC voltage changing from 1 V to 9 V and constant 1 V DC, with linear fitting; (c) under electro-thermal actuation at 156.914 kHz with the voltage of 1-9 V AC and 1 V DC along with parabola fitting.

Table 4.5: The dynamic characteristics of graphene/PMMA closed cavity ultrasonic sensor.

Actuation methods	Measured resonant frequency	Quality factor	Actuated sinusoidal signal frequency	Varying input signal range of sinusoidal signal	Sensitivity of vibration amplitude actuated by sinusoidal signal
Mechanical	163.150 kHz ±0.2%	49.45 ±6.8%	163.156 kHz	0.1 V to 2 V AC	14 nm/V
Electro-static	158.337 kHz ±0.4%	25.64 ±5.8%	158.64 kHz	1 V to 9 V AV	0.01 nm/V
Electro-thermal	158.965 kHz ±1.9%	34.42 ±15.8%	156.914 kHz	1 V to 9 V AV	0.002 nm/V^2

Frequency shift and quality factor

In mechanical and electro-static actuation, change in the quality factor versus the input signal has been detected to be relatively small compared to the electro-thermal case as shown in Figure 4.13.a and b.

In the case of the electro-thermal actuation, the change in quality factor has been temperature-related. The frequency shift at resonance is evident in the frequency response (Figure 4.11.c). The relationship between the frequency shift and the AC voltage has been plotted in Figure 4.13.c. The resonant frequency at 9 V AC has been upshifted to be 3.8 % from the frequency at 2 V AC. The upshift of the resonant frequency as the AC voltage increase could be a result of the negative thermal expansion coefficient of graphene[129]. Graphene shrinks as its temperature rises and therefore, the resonant frequency increases with rising AC voltage[22]. The fitting (red dash) of the frequency shift corresponds to $V_{ac}^{\frac{2}{3}}$ .The nonlinearity of the frequency shift can be related to the air damping inside the perfectly sealed closed cavity.

As shown in Table 4.5, the quality factor when the membrane is actuated mechanically has been observed to be the maximum among the three actuation methods. The piezo-electric disk has been directly in contact with the substrate during mechanical actuation and therefore the input ultrasonic energy has been the largest among the three actuation methods. The quality factor of the electro-static actuation has been measured to be the minimum among the three actuation methods, which can be related to the smallest displacement observed compared to the other two actuation methods. The air gap of 105 μm results in a capacitance of 16.5 fF and the signal generated by the electro-static stress between the membrane and substrate can be relatively small compared to the other two actuation methods.

The change in the quality factor has been studied in the resonator under the electro-thermal actuation. The quality factor has been measured to increase from around 36 to 40 when the AC voltage rises from 2 V and 3 V. The decrease of the quality factor has been observed when the AC voltage changes from 3 V to 8 V. A small increase of the quality factor has been measured when the AC voltage increased from 8 V to 9 V, as shown in Figure 5.c. Unlike the mechanical and electro-static actuation, frequency upshift has been observed in the resonator under electro-thermal actuation. The decrease in the quality factor suggests that the energy dissipated in the resonator is larger than the energy stored at resonant frequency[109], which can be due to the higher damping[22] or more surface loss[130] of the energy as higher AC voltage is applied to the membrane. The boost of thermal gradient in the membrane with increasing AC voltage might enhance the thermoelastic damping, which increases the dissipation[109]. Additionally, the possible surface stress increase with rising temperature might enlarge the surface loss, which results in energy dissipation[130, 131].

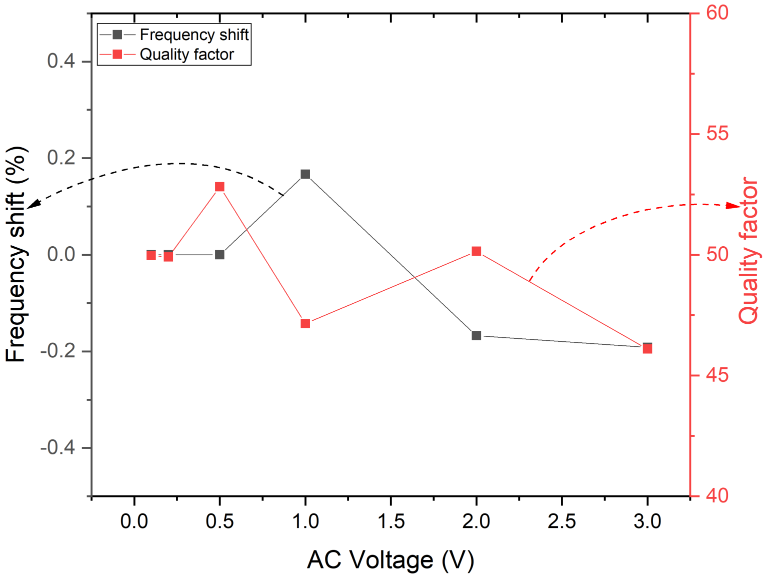

(a)

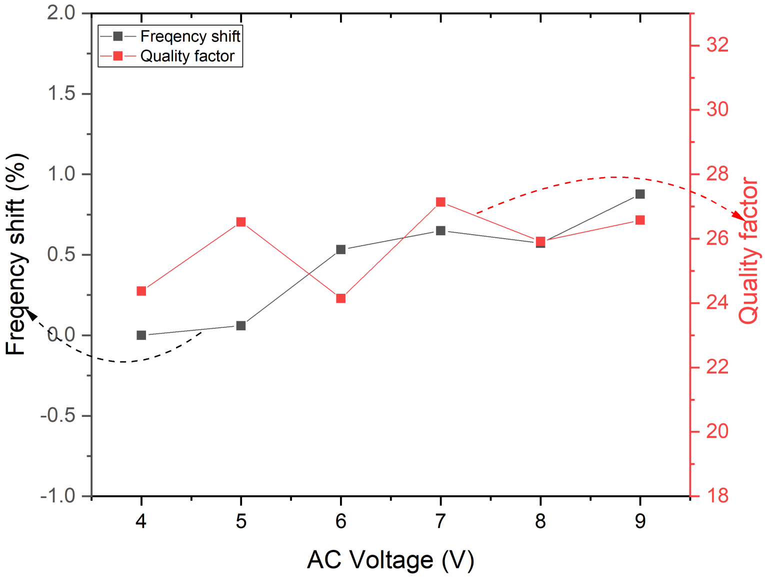

(b)

Figure 4.13: Continued

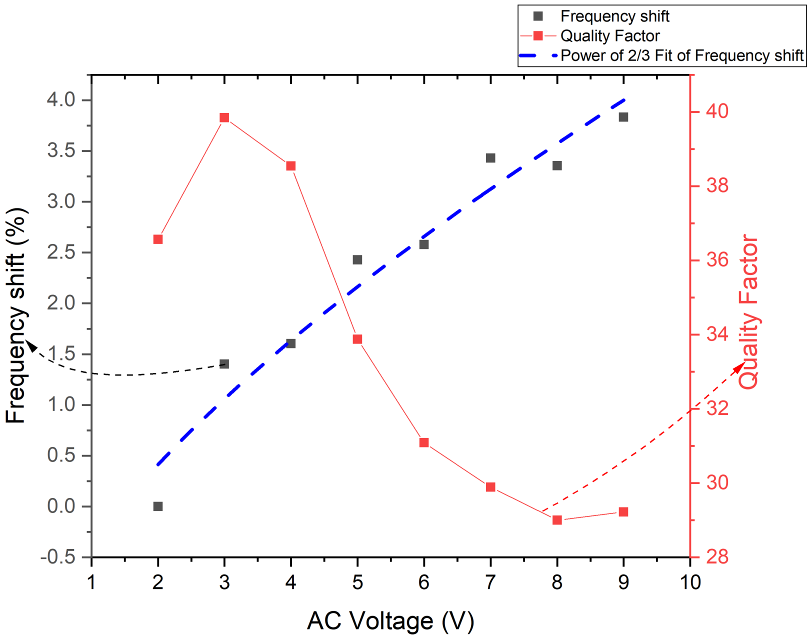

(c)

Figure 4.13: The frequency shift and quality factor of graphene/PMMA resonator under: (a) mechanical actuation (b) electro-static actuation; (c) electro-thermal actuation.

Mode shape

The mode shapes at the resonant frequencies by different actuation methods have been shown in Figure 4.14. The observation of (1,1) at the resonant frequencies by the three actuations methods can be caused by the closed cavity design and the impermeability of graphene[132]. The air leakage should be extremely small as the graphene/PMMA membrane has been sealed the closed cavity perfectly. Thus, the (0,1) mode which requires the large change of the air volume inside the cavity has been prevented and not been observed. Figure 4.14 (a) to (c) are placed at the same x-y plane to compare the orientations under different actuation schemes. The orientation of (1,1) mode shape has been observed to be similar in the mechanical and electrostatic actuation, which is possibly because the direction of the mechanical stress and electro-static stress has been vertical. In the case of electro-thermal actuation, the orientation of the (1,1) mode shape can be related to the position of the membrane electrodes. In the case of electrothermal actuation, the effect of the silver paste's mass loading on (1, 1) mode shape orientation should be negligible, due to force balance of the substrate. In the Figure 4.14, the measurements have been performed without silver pastes and the orientation of (1,1) mode, as shown in Figure 4.14.c, has been observed to be changed with position of electrodes (two electrodes placed on the top left and bottom right respectively). The direction of thermal stress on the membrane, which is related to the position of electrodes, shows more significant than the mass load of the silver paste.

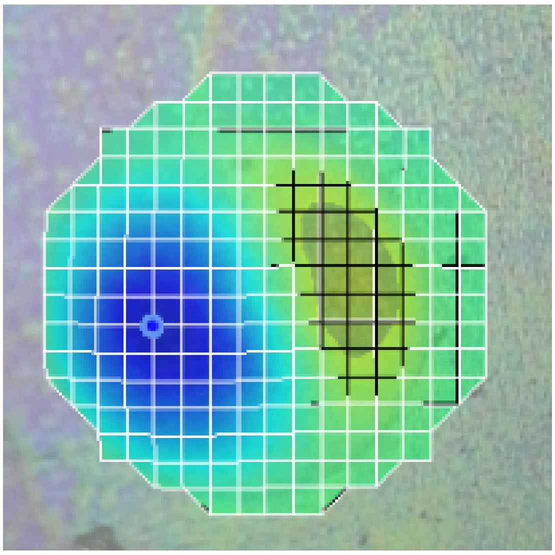

(a)

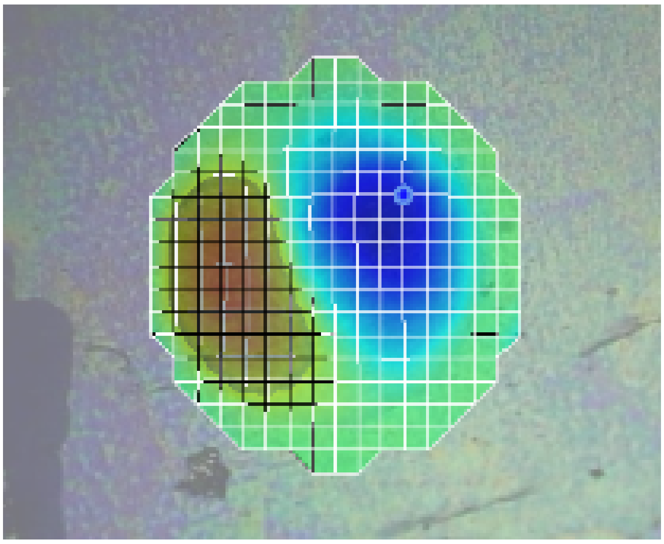

(b)

Figure 4.14: Continued

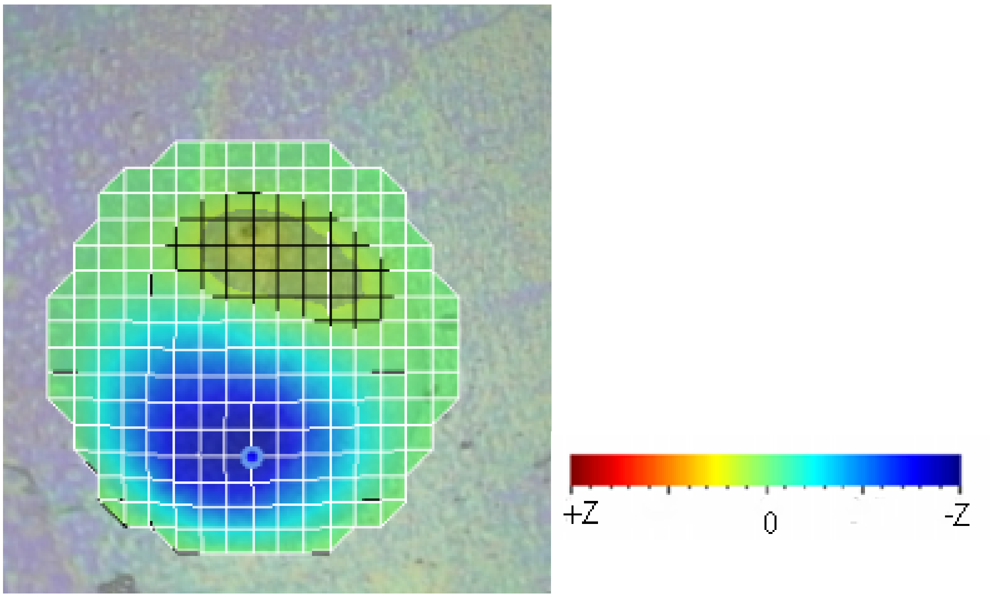

(c) scale bar

Figure 4.14: The (1, 1) mode shape of graphene/PMMA resonator under: (a) mechanical actuation (b) electro-static actuation; (c) electro-thermal actuation.

Strain analysis

The overall tension and strain can be derived from equation (4.3) and results are shown in Table 4.6. In the case of the mechanical actuation, the tension has been estimated to be the largest among the different actuation methods.

Raman spectrum

4.2.4 Conclusions

It is the first time that graphene-based closed cavity resonator for ultrasonic detection has been fabricated and actuated in atmosphere successfully. Using graphene dry transfer method with Kapton tape as the supporting frame developed by our group, the graphene/PMMA closed cavity sensor at a resonant frequency of around 160 kHz has been fabricated. The graphene/PMMA closed cavity resonator has been actuated mechanically, electro-statically and electro-thermally. The amplitude of the membrane has been observed to be linear with AC voltage for the mechanical and electro-static actuation and quadratic with AC voltage for the electro-thermal actuation. The membrane has been observed to exhibit (1,1) mode at the resonant frequencies. The membrane has been be tuned up to 4% by varying AC voltage between the membrane and nonlinearity in the frequency shift under electro-thermal actuation has been detected. The strain in the membrane under the three actuation methods has been estimated to be around 0.08%. The devices show the possibility of applying graphene as

Table 4.6: Overall tension and strain in the graphene/PMMA membrane deducted from the measured resonant frequency.

Actuation methods	Frequency (kHz)	Tension (N/m)	Strain (%)
Mechanical	163.150	3.00	0.0813
Electro-static	158.384	2.83	0.0766
Electro-thermal	158.965	2.85	0.0772

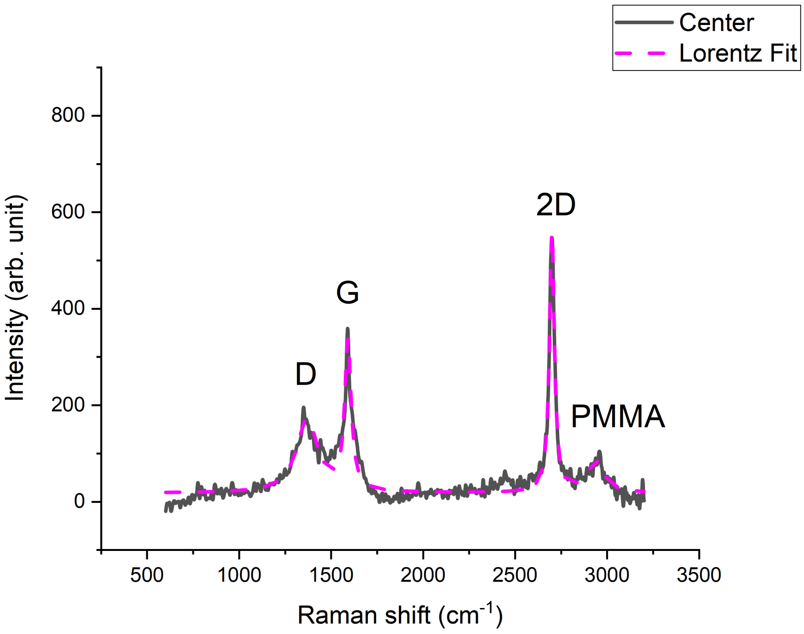

(a)

Figure 4.15: The Raman spectrum of graphene layer suspended over the closed cavity resonator and PMMA peak at $2958.33cm^{-1}$

ultrasonic detectors and opens a door to fabricating graphene-based ultrasonic sensors at the lower ultrasonic frequency of less than 200 kHz.

4.3 Summary

The design, fabrication and dynamic characterization of millimeter scale closed cavity resonators for audio and ultrasound sensing have been illustrated in this chapter. The characterization of graphene/PMMA resonators with the resonant frequency of around 11 kHz and 160 kHz has been determined for the first time. A modified graphene/PMMA transfer method using Kapton tape as supporting frame to fabricate closed cavity resonators for audio and ultrasound sensing. With the modified transfer method, the millimeter scale graphene/PMMA membranes have been transferred over the closed cavity with 3.5 mm and 0.5 mm diameters. In order to improve the capacitive sensitivity of graphene/PMMA closed resonators, the air gap between and membrane and the substrate should

Table 4.7: Positions, full width at half maximum (FWHM) of the D, G and 2D peaks.

The Raman spectrum has been measured on the center of the graphene/PMMA membrane using 0.8 mW laser power and with laser excitation of 514.5 nm. As shown in Figure 4.15, The Raman spectrum has been fitted with Lorentz function. The Raman shift and with of D, G and 2D peaks have been shown in Table 4.7. The Raman shift of PMMA has been measured at 2958.33 cm_{-1}.

D		G		2D	
position (cm^{-1})	FWHM (cm^{-1})	position (cm^{-1})	FWHM (cm^{-1})	position (cm^{-1})	FWHM (cm^{-1})
1369.9	141.17	1591.5	42.2	2699.6	32.46

be decreased. However, for the fully sealed closed cavity design, the displacement of the suspended graphene/PMMA membrane decreases when the air gap is decreased due to the effect of air damping. Thus, even though the air gap between the membrane and substrate decreases, the performance of the device can not be improved. For the conventional MEMS microphones, the vent holes can be etched in the thick and rigid materials, namely, silicon nitride and polysilicon. In the case of graphene, either holes etched in the membrane or the transfer of graphene onto partly open substrate should be challenging. In the next chapter, a novel fabrication method developed by our group will be presented to address this problem.

Chapter 5

Fabrication and characterization of graphene-based electro-static sensors using oxide sacrificial layer

This chapter illustrates the electrostatic sensors for audio sensing (section 5.1) and ultrasound sensing (Section 5.2), The devices have been fabricated by the oxide sacrificial layer. It is the first time, the silicon oxide has been used as the sacrificial layer to fabricated millimetre size graphene-based membrane. The characterization of the graphene/PMMA electro-static microphone under electro-static and audio actuation has been determined. The frequency response of the graphene-based ultrasonic sensor will be presented.

5.1 For audio sensing

5.1.1 Introduction

For acoustic sensors, graphene is also a desirable material. Compared to polysilicon or silicon nitride membranes used in the commercial microphones, graphene-based membranes possess the potential of achieving high sensitivity microphones due to its small thickness and low mass density. However, for sensing audio frequency (20 Hz to 20 kHz), the diameter of graphene-based membrane reported in graphene-based acoustic sensors has been required to be a few millimeters (3.5 mm to 7 mm)[87, 89, 90, 114, 133]. Considering multi-layer graphene membrane is about a few atoms' thick, it is challenging to transfer graphene due to the large aspect ratio of the membrane. So far, there have been a few acoustic applications based on graphene [83,87,89,90,114,115,124,133]. In recent research, the graphene membrane has been thickened by increasing the graphene layer number ranging from 67 [90] to 1800 [114] or by attaching 200 nm [89] or micrometer thick PMMA [114], in order to increase the stability of the devices. A 10-layer graphene diaphragm with up to 4 mm diameter has been fabricated but with complex vacuum-assisted sublimation transfer method [133]. Additionally, unlike the precise process of fabricating the commercial capacitive microphones where the diaphragm and backplate electrode have been fabricated onto one substrate[134], the graphene-based acoustic sensor has been processed with two-step method: the flexible graphene-based membrane has been transferred firstly onto a ring or a spacer to serve as a diaphragm with the support; then the supported membrane has been assembled manually into the case or cartridge [87, 89, 90, 114, 133] with backplate electrode inside to form the capacitive microphone. The two-step fabrication method increases the complexity and decreases the consistency of the sensors, which limits its application in the further minimization of the air gap. The air gap of the sensors with a few millimeter diameter in the literature has been reported to be from 8.8 μm to 172 μm [87, 89, 90, 114, 133]. The air gap of the devices is a variable parameter which could not be controlled due to the manual assembly. Furthermore, the bias voltage of the graphene-based acoustic sensors with more than 100 μm have been reported to be 50 V DC and 200 V DC [90, 133] to boost the sensitivity of acoustic response, which limits the potential of integrating the graphene-based devices on the smart phone, hearing aid or other wearable electronic devices. To improve the acoustic sensors' sensitivity, it is critical to minimize the air gap distance between the membrane and the substrate, thus maximizing the variable capacitance generated by sound pressure and accordingly, the capacitance of the static graphene-based microphone. Therefore, the development of a new process for minimizing the air gap between the membrane and the substrate is essential in improving the performance of the graphene-based acoustic sensors.

Releasing the graphene by etching the silicon dioxide underneath with HF acid has been reported to form cantilever[135] or bridge [136–138] devices in graphene nanomechanical systems. The length of the graphene membrane in the nanomechanical devices has been shown to be a few micrometers, and the thickness of the silicon dioxide has been designed to be around 300nm[135–138]. Using HF acid to etch silicon dioxide sacrificial layer for the development of the micrometer size graphene-based fully-clamped microphone could be difficult. The diameter of the graphene-based membrane over the thickness of the silicon dioxide layer should be designed to be around 1000 to achieve the relatively large capacitance and improved performance of the graphene-based microphone, which can increase the complexity of releasing the graphene-based membrane by etching the silicon dioxide. Additionally, unlike the cantilever and bridge structure, the etchant could flow from the sides of the graphene to etch the oxide. The fully-clamped design increases the difficulty to etch the silicon dioxide.

We have developed a process involving the etching of a silicon dioxide sacrificial layer to form an ultra-large graphene/ PMMA membrane microphone. The sacrificial layer can be used to control the distance of the air gap between the membrane and the substrate with electrode. It is the first time an ultra-large graphene/PMMA has been suspended fully over a closed cavity by sacrificing a silicon dioxide layer. The thickness of the silicon dioxide layer can be changed with a view to optimize the capacitance of the device and the total acoustic/mechanical (i.e. vibroacoustic) damping. The diameter to the thickness ratio of the sacrificial silicon dioxide in our work is about 1750. The difficulties in the method are to etch the thin silicon dioxide layer under the fully clamped large area of graphene/PMMA membrane and to prevent the membrane from being attached to the substrate. Henceforth, around 1500 square holes with 50 μm diameter have been designed and etched into the silicon substrate from the back. Then, the sacrificial layer is etched from the back side of the substrate, by HF vapour in the oxide etcher(Xeric Oxide Etch, memsstar). HF vapour has been used instead of HF liquid in order to decrease the humidity and to prevent stiction between the membrane and substrate.

In this work, with the new transfer method, an air gap of 2 μm has been achieved, which is the minimum spacing that has been reported, as shown in Table 5.1, giving a capacitance of 26.3 pF estimated from Equation (5.1):

$$C = \frac{\mathcal{E} A}{d}, \tag{5.1}$$

where, C is the capacitance of the device, $\mathcal{E}$ refers to the permittivity of dielectric, A is the area of plate overlap in square meters and d is the distance between plates in meters.

The device has been actuated electro-statically and the resonant frequency under electro-static actuation has been measured to be around 8.96 kHz $\pm 2\%$, which is within the audio frequency range (20 Hz to 20 kHz). In the case of the acoustic actuation, the device has been connected to the gate of a MOSFET with relatively small bias voltage of 2.6 V DC. The acoustic sensitivity of the sample has been measured to be around -47.5 dB V. The sensitivity of graphene-based microphone has been reported to be from -60 dB V to -20 dB V [87,89,114,133]. The sensitivity of the device reported here is comparable with other work.

Table 5.1: Comparison of our work to other research on graphene-based acoustic sensors

Membrane type	Reference	Air gap	Fabrication	Bias voltage	Sensitivity
300-layer graphene	[87]	18.6 μm	Dry transfer with PET support ring	200V	-60 dB V
1800-layer graphene and 2 μm PMMA	[114]	10 μm	Dry transfer with gold support ring	N/A	-20 dB V
Monolayer graphene and 200 nm PMMA	Our work [89]	8.8 μm	Dry transfer with silicon support ring	1 V	-60 dB V
10-layer graphene	[133]	172 μm	Vacuum-assisted sublimation transfer on the partly open substrate	200 V	-60 dB V
6-layer graphene and 450 nm PMMA	This work	2 μm	Silicon dioxide as sacrificial layer	2.6 V	-47.5 dB V

5.1.2 Experimental section

Operating principles and methods

Figure 5.1.a shows the optical image of the graphene/PMMA electro-static microphone. The graphene-based membrane consists of 450 nm PMMA and 6-layer graphene. The silver paste has been used to make contact to the graphene/PMMA membrane for electro-static actuation. The membrane has been suspended over a 3.5 mm diameter cavity. As shown in Figure 5.1.b, the graphene/PMMA membrane has been clamped fully over the silicon dioxide anchor on the silicon substrate. The air gap between the membrane and the substrate has been measured to be around 2 μm under Leica 150x optical microscope. The graphene/PMMA membrane and the silicon substrate work as two plates for the capacitive structure. The natural frequency formula for the graphene/PMMA membrane can be determined by Equation (4.3).

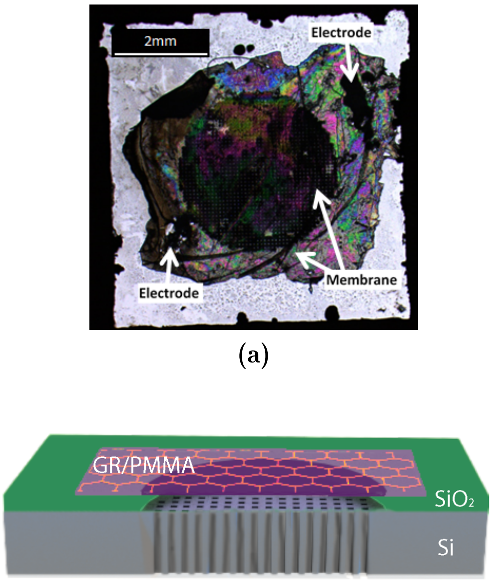

(a)

(b)

Figure 5.1: The optical image (a) and cross section schematic (b) of the graphene-based electro-static microphone.

Fabrication

The fabrication schematic has been depicted in Figure 5.2.a. First, 2.3 μm thick silicon dioxide has been deposited on the p-type silicon substrate of which the resistivity is 1-10 Ωcm. The silicon substrate has been used as the bottom electrode in the electrostatic actuation configuration. After around 1500 square vent holes with 50 μm width have been patterned within 3.5 mm diameter circle and then etched into the silicon from back side of the substrate. The membrane consisting of 6-layer graphene and 450 nm PMMA has been dry transferred on the silicon dioxide substrate and the details of the dry transfer method are shown in ref [19] [1]

. Lastly, the graphene/PMMA membrane has been released with HF vapour

---

[1] as shown in Figure 4.2.b, the preparation and dry transfer of the graphene/PMMA membrane onto the substrate using Kapton tape as frame: (i) the Kapton tape frame attached on the copper CVD graphene; (ii) PMMA spin-coated on the CVD graphene; (iii) the copper foil etched by ferric chloride; The dry transfer of the graphene/PMMA membrane: (iv) graphene/PMMA membrane dry transferred on the substrate and the Kapton tape frame peeled off from membrane at the temperature of 140°C; (v) the device cooled down in the air.

flowing through the partly etched silicon substrate to remove the silicon dioxide. In this way, the graphene-based membrane has been suspended over the silicon dioxide anchor, with an air gap of around 2 μm. The cross section of sample in each fabrication process has been illustrated in Figure 5.2.b I – IV accordingly.

Figure 5.2.c and d show the optical image before and after the silicon dioxide sacrificial layer has been etched. The thickness of the silicon dioxide changes the reflectivity of the visible light under the microscope. Therefore, the colour of graphene-based membrane seems to be changed when the silicon dioxide has been etched. With silicon dioxide as the sacrificial layer, the ultra large graphene-based membrane can be transferred over the air gap of 2 μm. The use of HF vapour reduces the humidity of the membrane in order to avoid the membrane being stuck on the substrate. The vent holes are designed for allowing the HF vapour to flow in to perform the etch release and also for reducing the damping of a device with such a small air gap.

The PMMA laminated layer has supported the graphene layer in the dry transfer method and the process of silicon dioxide etch release. The interface of graphene/PMMA membrane and silicon dioxide allows the millimeter-size membrane to be suspended fully over the closed cavity. The silicon dioxide on silicon has been designed to be the substrate for the graphene/PMMA membrane to be transferred onto. In addition, the silicon dioxide has worked as a sacrificial layer to control the air gap between the membrane and substrate.

5.1.3 Results and discussion

The graphene/PMMA closed cavity resonator has been characterised by Polytec laser Doppler Vibrometer (LDV). The Raman spectroscopy measured by Raman Spectroscopy (inVia Renishaw) has been shown in supplementary information. All measurements have been conducted on one device at room temperature and under atmospheric pressure.

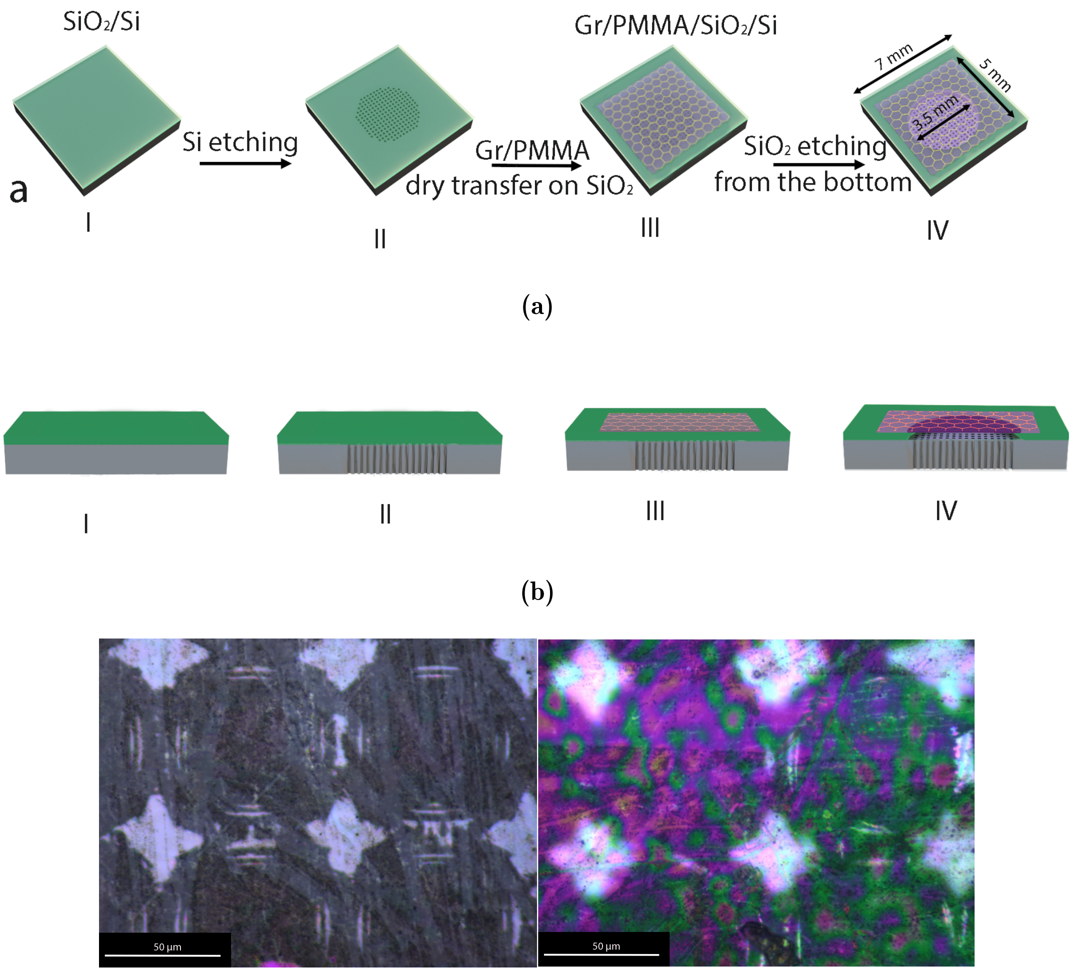

(a)

(b)

(c) (d)

Figure 5.2: a. I. deposit 2.3 µm silicon dioxide on the p-type substrate; II. pattern and etch the 50 µm width vent holes into the silicon from the back; III. dry transfer graphene-based membrane on the silicon dioxide layer; IV. Etch the silicon dioxide sacrificial layer via HF vapour (the diameter of the substrate, graphene/PMMA and the partly open cavity has been designed to be around 7 mm, approximately 5 mm and 3.5 mm respectively); b. the cross section of graphene/PMMA microphone during the process respectively; Suspended graphene-based membrane before (c) and after(d)the sacrificial silicon dioxide etch.

Capacitance

As mentioned above, the capacitance between the membrane and the substrate is calculated to be 26.3 pF. Under the measurement of HP 4280A 1 MHz CV meter, the capacitance is measured to be 26.2 pF. From the capacitance measurement, the air gap of the sample is estimated to be around 2.03 μm. Considering the sacrificial silicon oxide layer is measured to be 2.3 μm thick, the average deformation of the membrane has been estimated to be about 270 nm when using this transfer method. The aspect ratio of the membrane$'$s diameter over its static deformation is estimated to be around 4500. Therefore, the ultra large graphene-based membrane has been transferred to the substrate with small static deformation.

Electro-static actuation

The graphene-based membrane has been actuated electro-statically by the bottom silicon substrate (of which the resistivity is 1-10 Ωcm) with AC voltage ranging from 6V to 10V and constant 0.01V DC voltage. The frequency response and mode shape of the membrane have been measured by LDV. As shown in Figure 5.3.a, the resonant frequency has been measured to be around 8.96 kHz $\pm 2\%$. The quality factor of the device is estimated to be 1.53 $\pm 5\%$. The wide shape of the frequency response might be due to the large damping generated by the small air gap. The velocity of the graphene/PMMA membrane at the resonant frequency of be around 8.96 kHz has been observed to change from 5.79 μm/s to 17.56 μm/s with increasing AC voltage. The sensitivity of the velocity is shown in Figure 5.3.b. The black squares represent the measured velocity of the membrane with 6 V to 10 V actuation AC voltage, while the red dash line indicates the linear fitting. No resonance has been observed below 6 V AC which might be due to the effect of damping and the relatively large resistance of the p-type silicon and the silver paste used to contact the sample. The sensitivity of the resonant vibration velocity has been estimated to be 2 μm/s by the scope of the linear fitting. The

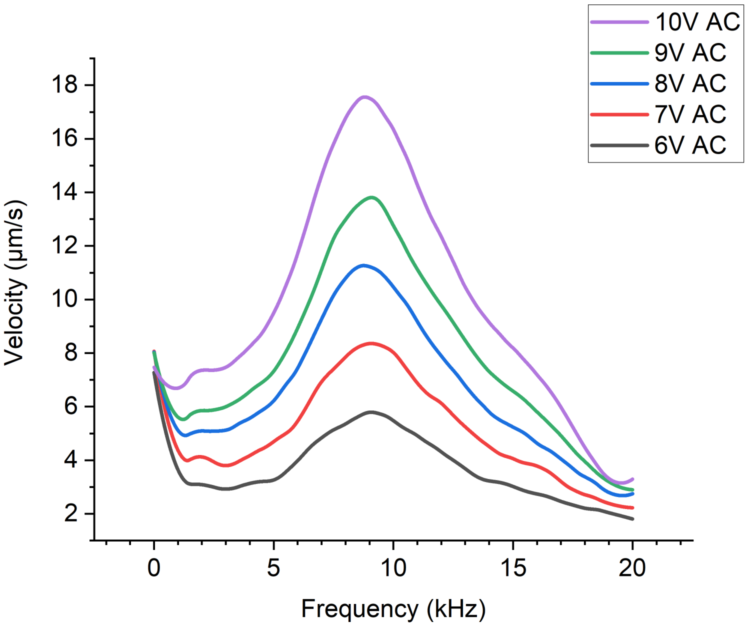

(a)

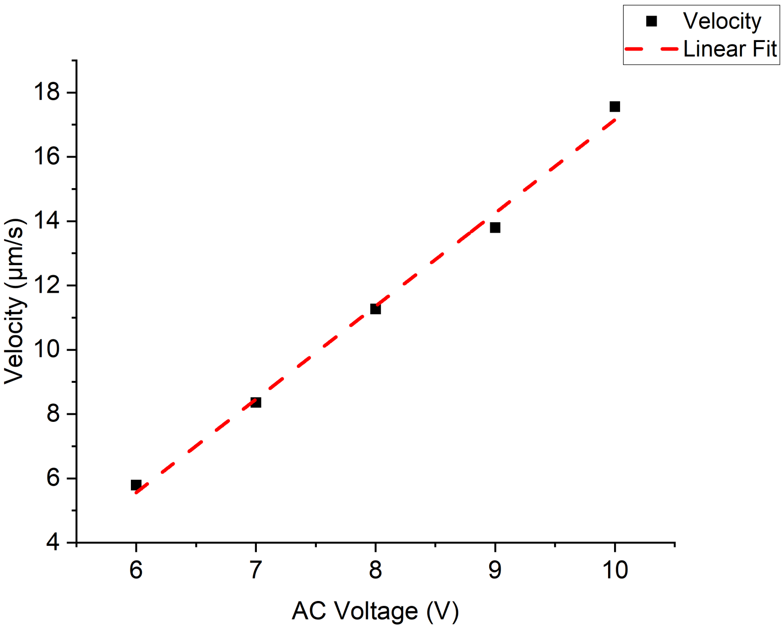

(b)

Figure 5.3: Continued

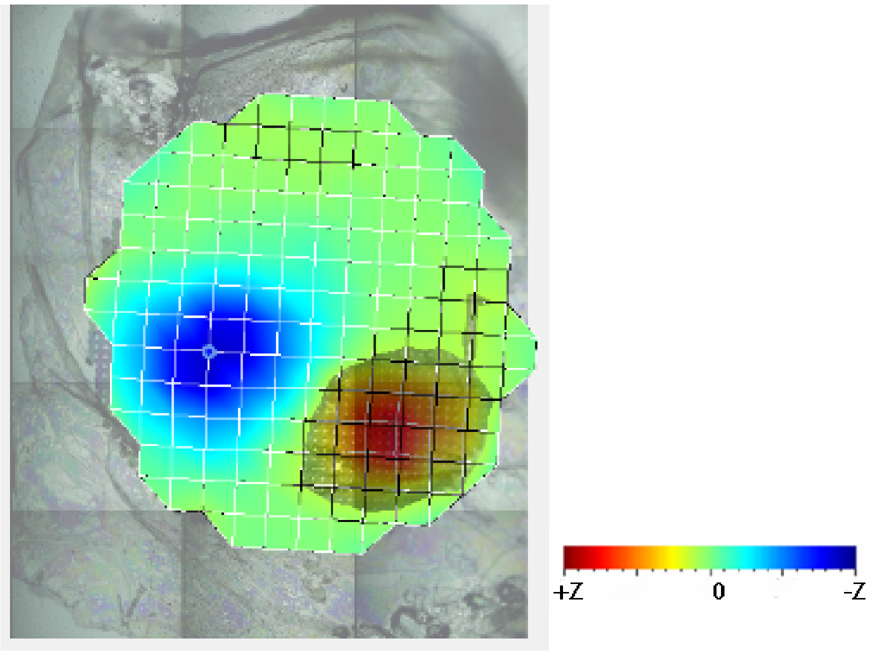

(c) scale bar (mm/s)

Figure 5.3: (a) Frequency response and (b) the velocity sensitivity the device by electro-static actuation varying AC voltage from 6V to 10V; (c) The mode shape for 3.5 mm diameter graphene/PMMA membrane at the frequency of 9.10 kHz actuated by 9V AC.

mode shape, which is shown in Figure 5.3.c, illustrates the membrane has been actuated under (1, 1) mode at the resonant frequency of 8.96 kHz. The absence of the (0, 1) mode also suggests the presence of damping of the sample.

Strain analysis

Table 5.2: Comparison of the tension and strain to the similar designs.

Reference	Actuation method	Actuation voltage	Types of the devices′ substrates	Graphene transfer method	Tension (N/m)	Strain (%)
Our work [105]	Electro-thermal	1V AC 1V DC	Open cavity	Wet transfer	1.89	0.048
Our work [124]	Electro-thermal	1V AC 1V DC	Closed cavity with 220 μm spacing	Dry transfer	1.53	0.041
This work	Electro-static	6V AC 0.01V DC	2.2 μm air gap with multiple vent holes	Released by etching sacrificial silicon dioxide layer	1.26	0.034

The total tension in the graphene/PMMA membrane under electro-static actuation has been calculated with Equation (5.5) and the results are shown in Table 5.2. In our other work [105, 124], the bilayer membranes have been suspended over the same cavity diameter, but the graphene transfer methods are different. In comparison to similar samples actuated electro-thermally by 1V AC and 1 V DC [105, 124], the tension and strain in this work are the minimum.

The increasing DC voltage might increase the electrical stiffness and soften the strain in the membrane and thus, the nonlinear response might be observed [139].

The DC voltage of 0.01V has been applied to this work, which is supposed to minimize the electrical softening, compared to our work [105, 124]. In the suspended graphene/PMMA structure the built-in tension dominates the overall tension [105, 124]. The decrease in the overall tension ($N_\mathrm{i} + N_\mathrm{a}$) in this work, might indicate using the silicon dioxide sacrificial layer compensates the built-in stress generated in the graphene transfer method.

Acoustic actuation

The graphene-based electro-static microphone has been connected to n-channel depletion mode MOSFET in order to measure the electronic signal transduced by the audio signal. The schematic measurement circuit set up has been illustrated in Figure 5.4.a. C_M represents the capacitance of the graphene-based microphone, which is variable when the sound pressure from the loudspeaker changes. The graphene-based microphone (C_M) applied with the bias voltage (V_C) of 2.6 V is connected to the gate of the MOSFET. The gate voltage (V_G) of MOSFET, has been measured to be 0.1 V, which suggests the voltage drop across C_M is 2.5 V when the graphene-based electro-static microphone is without acoustic actuation. The drain supply voltage (V_{DD}) and drain resistor (R_D) have been set to 13 V and 380 Ω respectively. When the graphene-based membrane has been actuated by the sound pressure, V_G varies with change of the voltage drop across C_M. Therefore, the drain current (I_D) of the MOSFET changes. The drain has been connected to a band-pass filter of which the lower and upper cut-off frequencies are designed to be 159 Hz and 16.8 kHz. A low-noise audio amplifier (Zoom F4 Multi-Track Field Recorder) has been connected to the read-out circuit output and giving the output voltage (V_{OUT}) with the voltage gain of 5. The graphene-based electro-static microphone has been actuated by the sound pressure from 0.2 Pa (80 dB) to 2 Pa (100 dB). The measurement has been conducted from 1 kHz to 20 kHz with 1 kHz step. As shown in Figure 5.4.b, V_{OUT} has been measured to vary from 0.5 mV to 13 mV with increasing sound pressure. The output voltage has been observed to ascend with the increasing sound pressure.

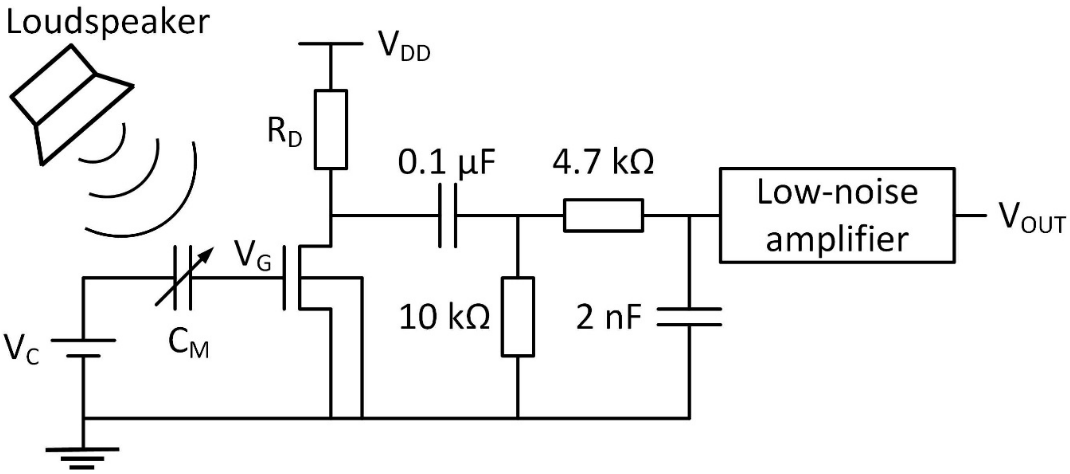

(a)

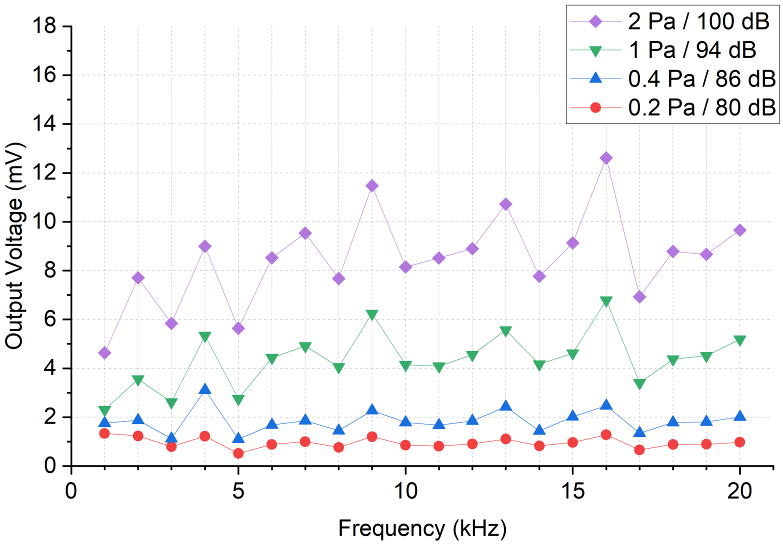

(b)

Figure 5.4: Continued

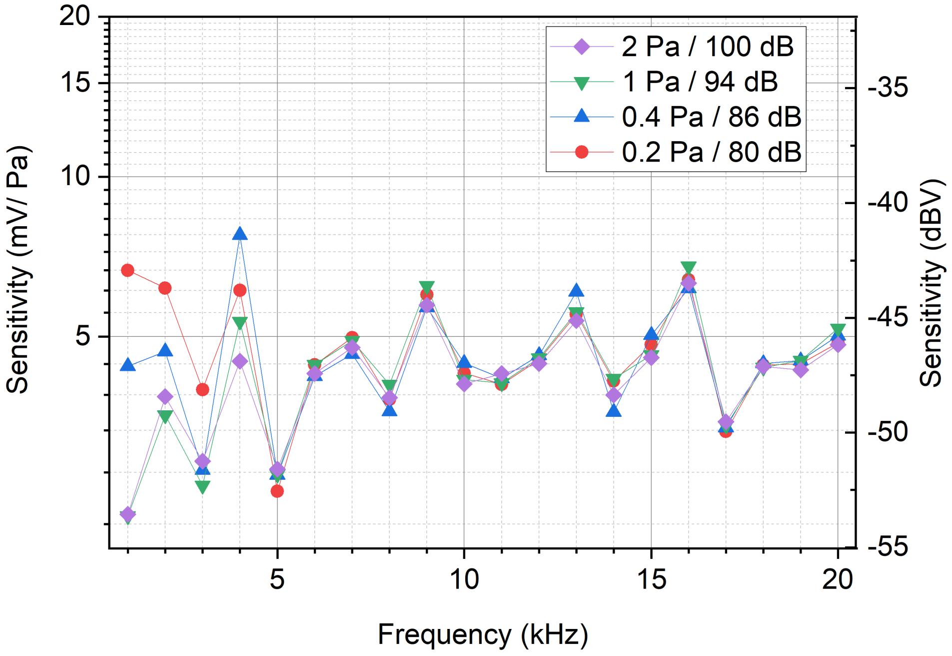

(c)

Figure 5.4: (a) The schematic of the measurement circuit under acoustic actuation; the output voltage response (b) and the output voltage sensitivity (c) of the graphene-based electro-static microphone system.

The output voltage sensitivity has been estimated by the output voltage over the sound pressure. Dividing the sensitivity value relative to 1 V/Pa has been expressed in dBV, which is illustrated in Figure 5.4.c. The sensitivity of the device has been estimated to be around -47.5 dBV (4.22 mV/Pa) ±10%. At frequencies between 1 kHz and 4 kHz, a change in the sensitivity as a function of sound pressure is evident, as shown in Figure 5.4.c. The observation could be related to damping effect [140]and a smaller signal to noise ratio at the lower frequency range. The device's sensitivity as a function of sound pressure is observed to be relatively constant with average variation of 0.02 mV/Pa in the frequency range from 5 kHz to 20 kHz.

5.1.4 Conclusions

The fabrication and characterization of a graphene/PMMA electro-static microphone is reported. A novel process of using silicon dioxide as the sacrificial layer has been developed. It is the first time that an ultra-large graphene-based membrane has been suspended over the substrate with a 2 µm air gap and actuated electro-statically. Using the new processing method, ultra-large graphene-based capacitor has been fabricated controllably to minimize the spacing between the membrane and substrate. From Raman spectra, the strain of the membrane has been estimated to be around 0.034 %. The frequency response of the graphene/PMMA microphone under electro-static actuation shows that the resonant frequency of the device is around 8.96 kHz ±2%. The velocity of graphene/PMMA membrane under resonance has been observed to be linear with input AC voltage. The acoustic response with sensitivity of -47.5 dBV (4.22 mV/Pa) ±10% has been estimated which is comparable with research in similar field, suggesting the potential of commercial microphone development with good performance.

5.1.5 Supporting Information: The Raman spectrum of graphene layer on capacitive microphone

Table 5.3: Positions, full width at half maximum (FWHM) of the D, G and 2D peaks.

D		G		2D	
position (cm^{-1})	FWHM (cm^{-1})	position (cm^{-1})	FWHM (cm^{-1})	position (cm^{-1})	FWHM (cm^{-1})
1342.8	47.8	1600.1	20.6	2703.2	39.3

Raman spectroscopy has been conducted on the center of the membrane suspended over the electro-static microphone using 0.8 mW laser power and with laser excitation of 514.5 nm. The Raman spectrum has been depicted in Figure 5.5 and Lorentz function has been used to fit the peaks. The Raman shift position and width of the D peak, G peak and 2D peak has been illustrated in the Table 5.3. The 6-layer Chemical Vapor Deposition (CVD) graphene has been used for the device. As shown in Figure 5.5.b and c, the sharp shape of 2D peak and G peak suggests the graphene is around 5-10 layers [120]. The intensity ratio between D peak and G peak is estimated to be around 0.23, which indicates the graphene is defected [120]. The defect of graphene layer might be generated by the structural disorder [121, 122]. The peak of PMMA has been detected at around 2995 cm^{-1} [141].The absence of silicon dioxide in the Raman spectra at around 550 cm^{-1}[142], has shown the graphene/PMMA membrane has been released successfully from the sacrificial silicon dioxide layer.

5.2 For ultrasound sensing

5.2.1 Introduction

In this work, an electro-static graphene/PMMA sensor for ultrasound detection with the target frequency between 100 kHz to 200 kHz has been reported. The membrane is consisted of 6-layer graphene and 450 nm PMMA as laminated layer,

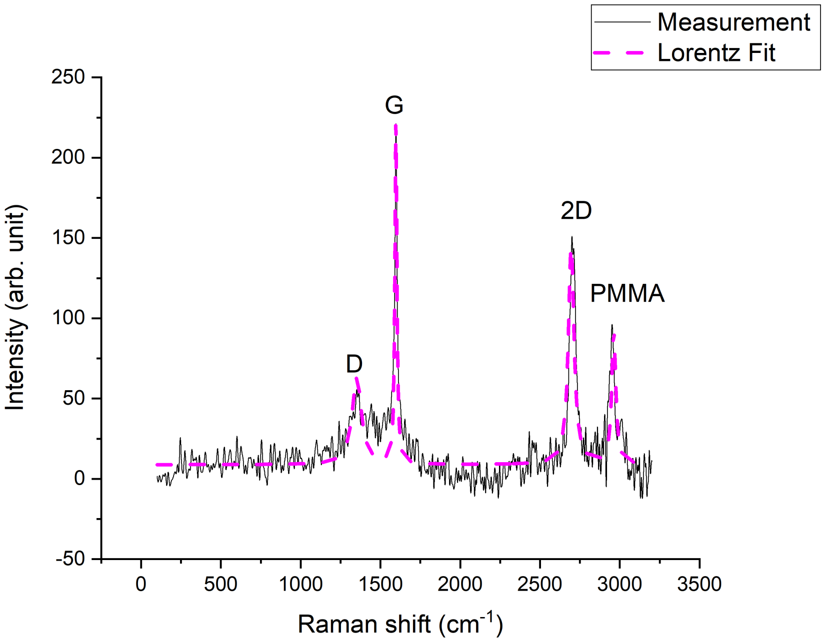

(a)

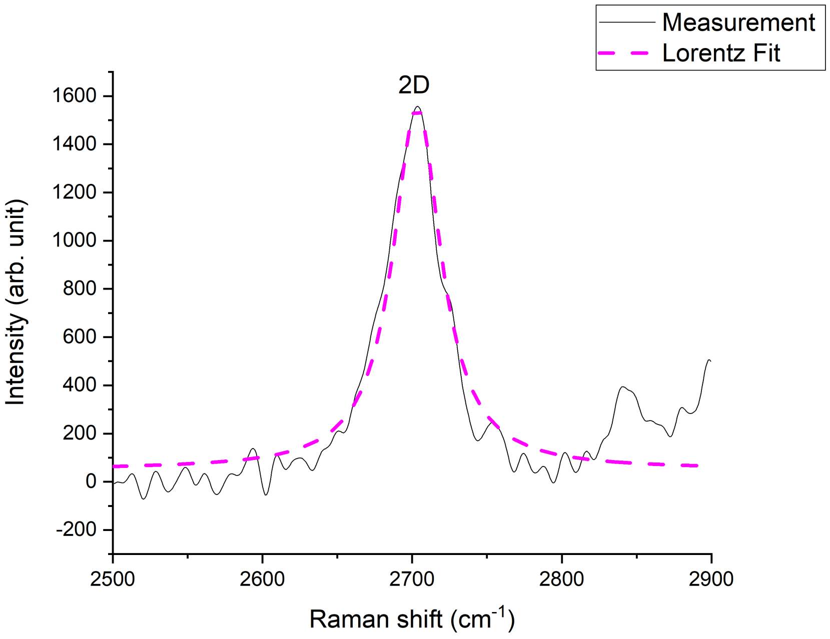

(b)

Figure 5.5: Continued

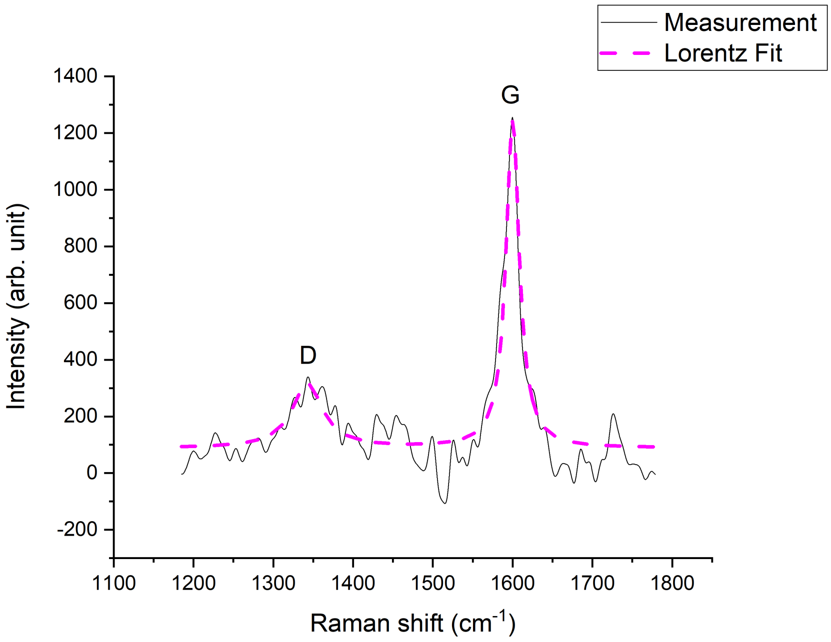

(c)

Figure 5.5: The Raman spectrum of graphene layer on the acoustic capacitive microphone: (a) full scan and PMMA peak at 2955.74 cm^{-1} (b) D peak and G peak (c) 2D peak.

which has been suspended over the partly open cavity with diameter of 0.5 mm. The actuation and measurement has been conducted in atmosphere and at room temperature. The device has been fabricated using the oxide sacrificial layer process developed by our group[143]. The air gap of 2 μm has been achieved by controlling the thickness of silicon dioxide thickness. The characteristics of the ultrasound sensor has been determined by electro-static actuation.

5.2.2 Device design and operating principles

The graphene/PMMA membrane has been fully clamped over substrate with multiple vent holes with the diameter of around 500 μm, as the optical image shown in Figure 5.6.a and Figure 5.6.b. The laminated PMMA layer works as the supporting layer for the graphene to enhance the durability and to protect the graphene. The vent holes have been etched through the silicon substrate for the purpose of etching the silicon oxide sacrificial layer to achieve the small air gap

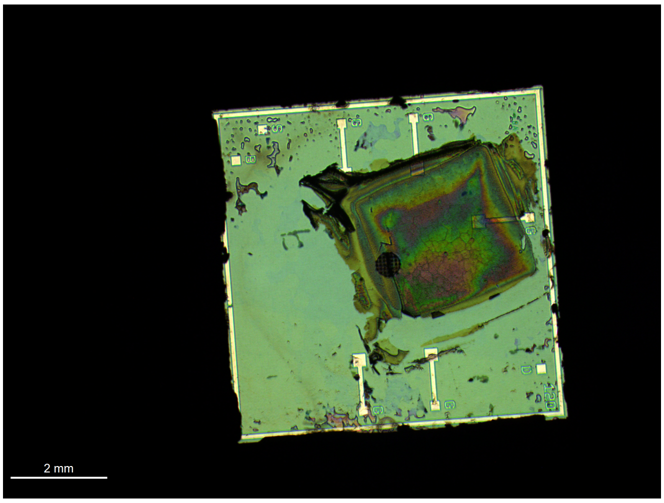

(a)

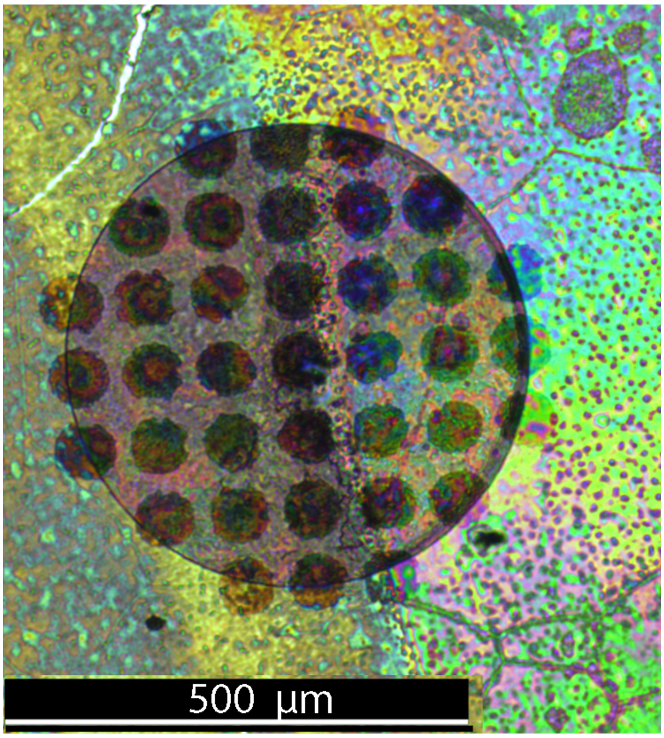

(b)

Figure 5.6: Continued

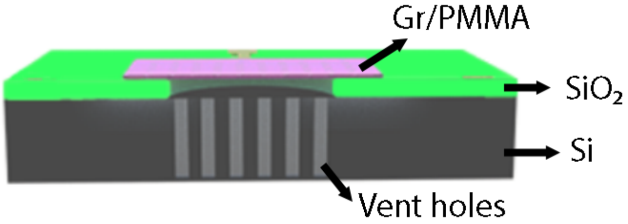

(c)

Figure 5.6: (a) The optical image of the graphene/PMMA ultrasonic sensor; (b) the image of the suspended membrane over the vent holes; (c) the cross-section schematic of the graphene/PMMA ultrasonic sensor.

of 2 μm between the graphene/PMMA membrane and substrate, as the cross-section schematic shown in Figure 5.6.c. The capacitance has been estimated to be 0.46 pF, using equation (5.1):

The electrostatic force (F_{el}) between the suspended graphene/PMMA membrane and the substrate can be determined by Equation (4.4) [99, 144].

5.2.3 Fabrication process

As depicted in Figure 5.7, the fabrication of graphene/PMMA ultrasonic sensor has been formed by four main steps: (a) Substrate preparation: i. the deposition of 2 μm silicon dioxide; ii. the pattern and etch of electrodes; iii. the etch of hole from the back side of the silicon substrate; (b) Graphene/PMMA membrane preparation: iv. cutting the graphene-CVD copper into the square with the side width of 5 mm; v. spin-coated PMMA on the graphene-CVD copper foil; vi. the etch of copper in Iron (III) Chloride ($FeCl_3$); (c) The wet transfer of graphene/PMMA membrane: vii. the graphene/membrane scooped into the Deionized water (DI water) and transferred onto the substrate; viii. The graphene/PMMA ultrasonic sensor dried in the hot plate at the temperature of 80 °C for 5 minutes and 140°C for 10-20 seconds; (d) The release of graphene/PMMA membrane: ix. the etch of silicon dioxide with the Hydrofluoric (HF) vapour; x. the graphene/PMMA membrane suspended over the silicon dioxide and the capacitive ultrasonic sensor formed. One sample of this structure has been

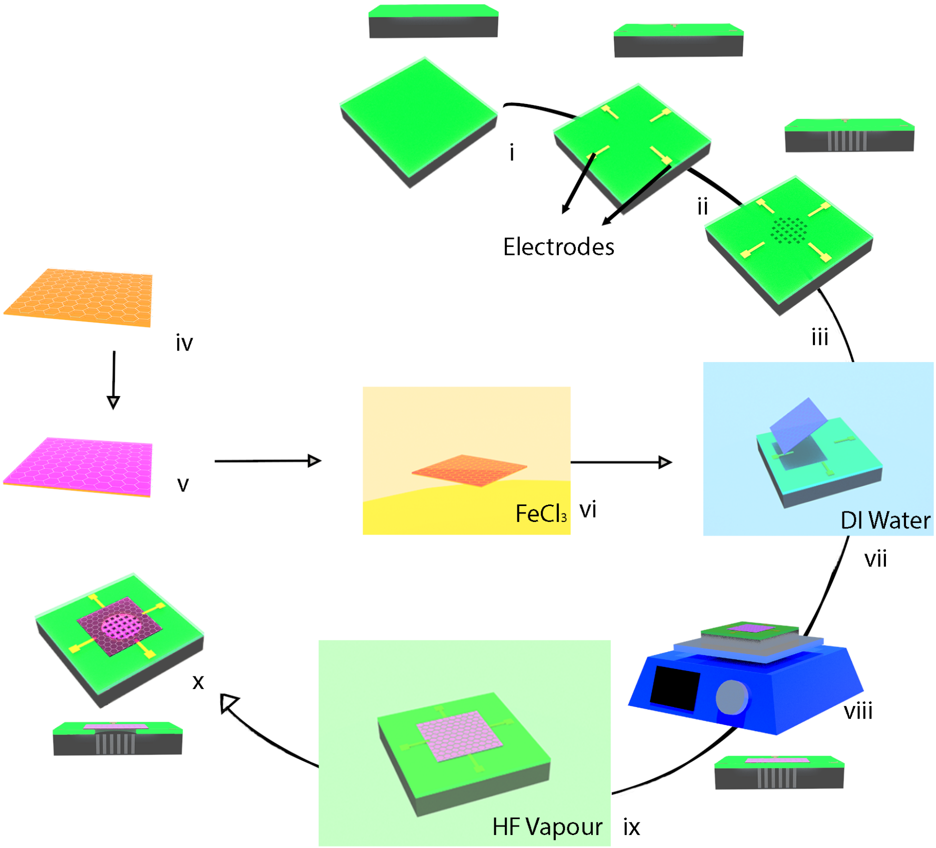

Figure 5.7: The fabrication schematic and cross-section schematic of the ultrasonic sensor formed by silicon oxide sacrificial layer: the preparation of the substrate (i-iii); the preparation of graphene/PMMA membrane (iv-vi); the wet transfer of graphene/PMMA membrane onto the substrate (vii-viii) and the release of the graphene/PMMA by etching the silicon dioxide sacrificial layer with Hydrofluoric (HF) vapour (ix-x).

fabricated with the success rate of 100 %. The repeatability and success rate of the silicon dioxide layer has been over 80 %.

5.2.4 Results and discussion

To investigate the dynamic characteristics of the graphene/PMMA ultrasonic capacitive sensor, the electro-static signal has been applied between the membrane and the substrate. The silicon with the resistivity of 0.001 - 0.005 1 Ωcm, has been used as the bottom electrode. The dynamic behaviour of the graphene/PMMA membrane has been characterised by Polytec Laser Doppler Vibrometer (LDV). The frequency response of the membrane under the electro-static signal of the varying AC voltage from 1 V to 9 V and the constant 1 V DC has been shown in Figure 5.7.a. The displacement has been observed to increase with the rising AC voltage and decrease with growing frequency from 100 kHz and 200 kHz. The resonant peaks have not been observed through the frequency sweep. The absence of the resonant peaks and the decrease of the displacement with the increase actuation frequency suggest the high damping between the membrane and the substrate[145]. The sine-function signal with the frequency of 100 kHz, 125 kHz, 150 kHz, 175 kHz and 200 kHz has been applied between the membrane and the substrate. The voltage of the sine signal has been varying AC voltage from 1 V to 9 V and constant 1 V DC.

As shown in Figure 5.7.b, the displacement has been observed to decrease with the increasing frequency. The linearity has been observed at the amplitude of the membrane under the actuation voltage from 1 V to 8 V. The displacement of the membrane has been measured to be much smaller than the air gap between the membrane and substrate. As equation (4.4) shows, electrostatic force has been determined proportionally by AC voltage applied between the membrane and substrate. A possible explanation of the nonlinearity at the 9 V AC voltage is the nonlinear damping force that is strongly dependent on the amplitude of motion[136]. The displacement and sensitivity of amplitude which has been

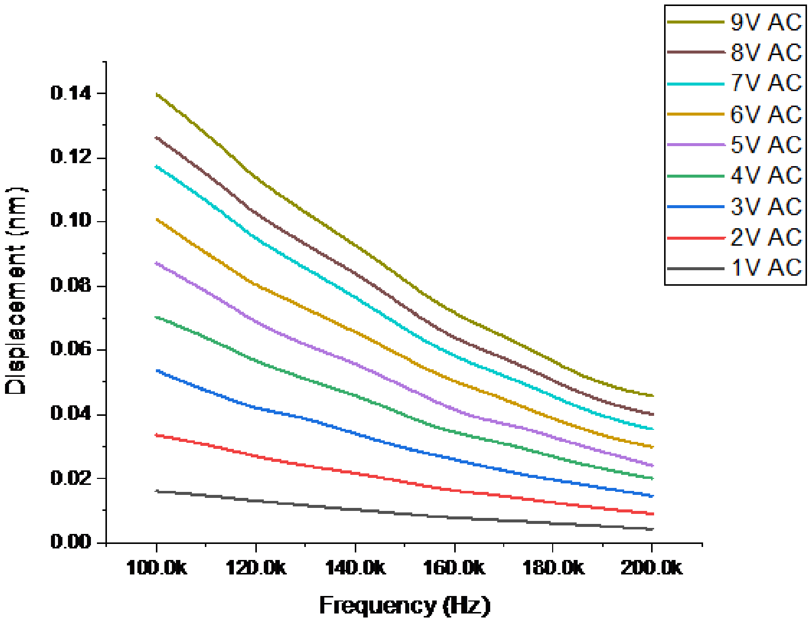

(a)

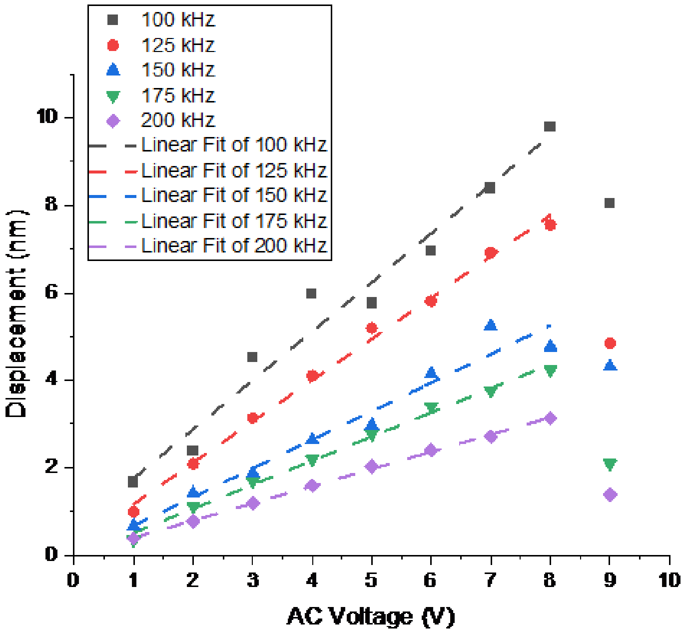

(b)

Figure 5.8: Continued

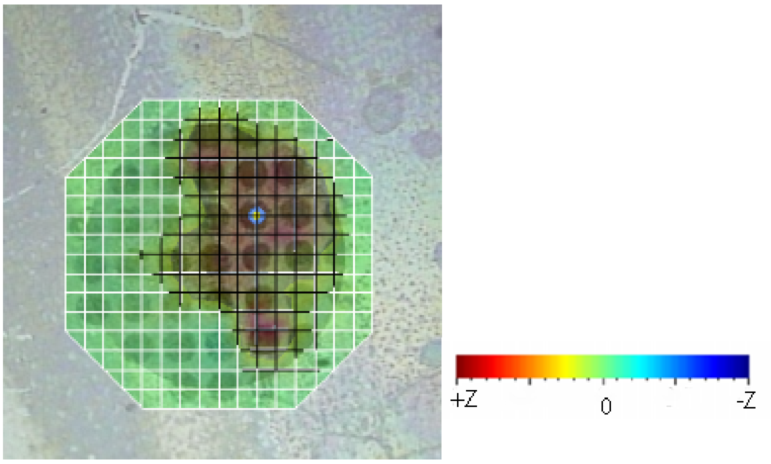

(c) scale bar

Figure 5.8: The frequency response (a) and The sensitivity of amplitude (b) of the sensor under electrostatic atuation from 100 kHz to 200 kHz and the increasing AC voltage from 1 V to 9 V and constant 1 V DC; (c) the mode shape of the sensor under electrostatic actuation with the sinusoidal signal with the frequency of 150 kHz and the voltage of 5 V AC and 1 V DC .

actuated by the sine wave signal have shown in the Table 5.4. The mode shape of the device with the sinusoidal signal with the frequency of 150 kHz and the voltage of 5 V AC and 1 V DC has been shown in Figure 5.7.c.

Table 5.4: The displacement and the sensitivity of amplitude actuated by the sinusoidal signal.

Frequency (kHz)	The range of the displacement from 1V AC to 8V AC (nm)	The sensitivity of amplitude from 1V AC to 8 V AC (nm/V)
100	1.67 to 9.78	1.12
125	0.99 to 7.56	0.94
150	0.67 to 4.77	0.65
175	0.34 to 4.23	0.55
200	0.35 to 3.13	0.39

5.2.5 Conclusions

The graphene/PMMA ultrasound sensor has been investigated under the electro-static actuation scheme. By releasing the silicon dioxide sacrificial layer, the graphene/PMMA ultrasound sensor has achieved an air gap of 2 μm. The displacement and sensitivity of amplitude have been decreased with increasing actuation frequency. The absence of resonance could be due to the effect of air damping. Compared to the 3.5 mm diameter cavity device for audio sensing, the effect of damping might increase due to the smaller area of membrane. The linearity of displacement with increasing AC voltage has been observed from 1 V AC to 8 V AC and the nonlinearity of the displacement has been detected at 9 V AC. The device shows the possibility of applying graphene to ultrasound transducers with target frequency in the order of hundreds kilohertz.

5.3 Summary

Overall, the graphene/PMMA acoustic electro-static sensors for audio and ultrasound detection have been presented in this chapter. Using silicon dioxide as sacrificial layer, the air gap of around 2 μm has been the minimum air gap among millimeter size graphene-based membrane formed capacitive structure so far. As mode shapes of the sensors shown in Figure 5.3 and Figure 5.7, the membranes have not been fully actuated. The effect on partial clamping of the membrane should be further studies in order to improve the performance of the graphene-based electro-static sensors. The possible reasons to the patrial clamping would be: 1) the sacrificial oxide has not been fully etched; 2) the tension applied to membrane during the oxide has been etched; 3) the damping caused by the complex air flow for the multiple vent holes prevents the vibration of the membrane. In addition, the absence of resonance in the ultrasound design is interesting to study further. The performance of graphene/PMMA electro-static microphone path a way to graphene-based audio transducers application.

Chapter 6

Conclusions

6.1 Conclusions and future work

Motivated by the extraordinary electrical and mechanical properties of graphene, graphene/PMMA acoustic transducers for audio and ultrasound detection have been fabricated and characterised in this research. The five transducers illustrated in the thesis are summarized in Table 6.1.

Table 6.1: Comparison of our work to other research on graphene-based acoustic sensors

Illustrated devices	Graphene transfer process	Membrane diameter (mm)	Resonant frequency (kHz)	Air gap (μm)	Actuation methods	Sections of the thesis	Published status
Ultrasonic open cavity resonator	Wet transfer	0.5 (square)	~77	open	Mechanical; Electro-thermal	Chapter 3	Not published
Closed cavity resonator for audio sensing	Modified dry transfer with Kapton tape frame	3.5 (circle)	~11	220	Mechanical; Electro-thermal; Audio	Chapter 4, Section 4.1	Published
Closed cavity resonator for ultrasound sensing	Modified dry transfer with Kapton tape frame	0.5 (circle)	~160	105	Mechanical; Electro-thermal; Electro-static	Chapter 4, Section 4.2	Not published
Electro-static audio microphone	Modified dry transfer with oxide as the sacrificial layer	3.5 (circle)	~160	2.3	Electro-static; Audio	Chapter 5, Section 5.1	Published
Electro-static sensor for ultrasound sensing	Wet transfer with oxide as the sacrificial layer	0.5 (circle)	N/A	2	Electro-static	Chapter 5, Section 5.2	Not published

First of all, the graphene transfer methods are selected based on the structure of devices. For the open cavity design, the wet transfer can be used. To achieve the closed cavity structure, the modified dry transfer with Kapton tape as the supporting frame has been developed for the first time. The modified dry transfer can be easily conducted without extra etching step on the Kapton tape. The laminated PMMA serves as the adhesion layer between the graphene layer and substrate. Furthermore, graphene transfer method using the silicon dioxide sacrificial layer has been developed to decrease the air gap between membrane and substrate and lower the air damping. The air gap has been decreased significantly down to around 2 μm. It is the first time that the silicon dioxide sacrificial layer has been released successfully from the millimetre-size graphene/PMMA membrane.

In addition, the devices have been characterized by mechanical, electro-static, electro-thermal and audio actuation methods. The frequency response and sensitivity of amplitude for the devices have been determined. For the closed cavity design, (1,1) mode has been dominant in the frequency response and thus the resonant frequencies are observed to be approximately twice the response frequency measured in the open cavity structure. For the partly open designs formed by oxide sacrificial layer, the resonant frequency of the graphene/PMMA microphone has been observed to be smaller than the closed cavity resonator with the same membrane size. Moreover, the resonance has been absent in the ultrasonic electrostatic sensor. The damping effect or the vibration of the partly etched substrate plays a role in the membrane's vibration and influence the frequency response of the devices, which is interesting to study further.

To conclude, the illustrated devices open a new gate to graphene-based acoustic sensors for audio and ultrasound sensing. Graphene-based materials shows the potential of achieving ultra-thin, durable devices with good performance, which can be applied to the next generation acoustic products, like microphones, speaker and ultrasound radio.

In terms of future work, the process should be improved for the release of graphene by etching the silicon dioxide layer. The investigation should be conducted to study the partial clamping of the membranes. Additionally, by decreasing the thickness of the silicon dioxide layer increases the capacitance between and membrane and substrate, which would significantly improve the performance of the graphene-based electro-static sensors. The graphene-based resonators or sensors can be integrated with transistors and form graphene-based RGT. The fabrication process using the silicon dioxide sacrificial layer provides a prospect to integrate the sensors and transistor in one chip. Furthermore, the nonlinearity of the displacement has been observed at the AC voltage of 9 V in the graphene/PMMA membrane with 0.5 mm diameter suspended over the closed cavity and partly open cavity. The research of the nonlinearity should be helpful in performance improvement of the graphene-based MEMS devices.

Bibliography

[1] H. Nathanson, W. Newell, R. Wickstrom, and J. Davis, "The resonant gate transistor," *IEEE Transactions on Electron Devices*, vol. 14, no. 3, pp. 117–133, 1967. [Online]. Available: http://ieeexplore.ieee.org/lpdocs/epic03/wrapper.htm?arnumber=1474635

[2] Y. Sun, Y. Dong, R. Gao, Y. Chu, M. Zhang, X. Qian, and X. Wang, "Wearable pulse wave monitoring system based on mems sensors," *Micromachines*, vol. 9, no. 2, p. 90, 2018.

[3] C. Lee, R. Radhakrishnan, C.-C. Chen, J. Li, J. Thillaigovindan, and N. Balasubramanian, "Design and modeling of a nanomechanical sensor using silicon photonic crystals," *Journal of Lightwave Technology*, vol. 26, no. 7, pp. 839–846, 2008.

[4] K.-T. Lam, M. Stephen Leo, C. Lee, and G. Liang, "Design evaluation of graphene nanoribbon nanoelectromechanical devices," *Journal of Applied Physics*, vol. 110, no. 2, p. 024302, 2011.

[5] K. H. Koh, T. Kobayashi, H. Liu, and C. Lee, "Investigation of a piezoelectric driven mems mirror based on single s-shaped pzt actuator," *Procedia Engineering*, vol. 25, pp. 701–704, 2011.

[6] S. Marauska, M. Claus, T. Lisec, and B. Wagner, "Low temperature transient liquid phase bonding of au/sn and cu/sn electroplated material systems for mems wafer-level packaging," *Microsystem technologies*, vol. 19, no. 8, pp. 1119–1130, 2013.

[7] J. Xie, C. Lee, M.-F. Wang, Y. Liu, and H. Feng, "Characterization of heavily doped polysilicon films for cmos-mems thermoelectric power

generators," *Journal of Micromechanics and Microengineering*, vol. 19, no. 12, p. 125029, 2009.

[8] B. Yang, C. Lee, R. K. Kotlanka, J. Xie, and S. P. Lim, "A mems rotary comb mechanism for harvesting the kinetic energy of planar vibrations," *Journal of Micromechanics and Microengineering*, vol. 20, no. 6, p. 065017, 2010.

[9] C. Lee, A. Yu, L. Yan, H. Wang, J. H. He, Q. X. Zhang, and J. H. Lau, "Characterization of intermediate in/ag layers of low temperature fluxless solder based wafer bonding for mems packaging," *Sensors and Actuators A: Physical*, vol. 154, no. 1, pp. 85–91, 2009.

[10] J. Zhu, X. Liu, Q. Shi, T. He, Z. Sun, X. Guo, W. Liu, O. B. Sulaiman, B. Dong, and C. Lee, "Development trends and perspectives of future sensors and mems/nems," *Micromachines*, vol. 11, no. 1, p. 7, 2020.

[11] H. C. Lee, W.-W. Liu, S.-P. Chai, A. R. Mohamed, C. W. Lai, C.-S. Khe, C. Voon, U. Hashim, and N. Hidayah, "Synthesis of single-layer graphene: A review of recent development," *Procedia Chemistry*, vol. 19, pp. 916–921, 2016.

[12] J. H. Warner, F. Schaffel, M. Rummeli, and A. Bachmatiuk, *Graphene: Fundamentals and emergent applications.* Newnes, 2012.

[13] E. Stolyarova, K. T. Rim, S. Ryu, J. Maultzsch, P. Kim, L. E. Brus, T. F. Heinz, M. S. Hybertsen, and G. W. Flynn, "High-resolution scanning tunneling microscopy imaging of mesoscopic graphene sheets on an insulating surface," *Proceedings of the National Academy of Sciences*, vol. 104, no. 22, pp. 9209–9212, 2007.

[14] O. V. Sinitsyna and I. V. Yaminsky, "Atomic resolution probe microscopy of the graphite surface," *Russian chemical reviews*, vol. 75, no. 1, p. 23, 2006.

[15] C. A. C. A. Coulson, *Coulson's Valence / edited by Roy McWeeny.*, [third edition]. ed. Oxford ;: Oxford University Press, 1979.

[16] W. S. Lee and S. S. Lee, "Piezoelectric microphone built on circular diaphragm," *Sensors and Actuators A: Physical*, vol. 144, no. 2, pp. 367–373, 2008.

[17] I. Frank, D. M. Tanenbaum, A. M. van der Zande, and P. L. McEuen, "Mechanical properties of suspended graphene sheets," *Journal of Vacuum Science & Technology B: Microelectronics and Nanometer Structures Processing, Measurement, and Phenomena*, vol. 25, no. 6, pp. 2558–2561, 2007.

[18] A. Castellanos-Gomez, V. Singh, H. S. van der Zant, and G. A. Steele, "Mechanics of freely-suspended ultrathin layered materials," *Annalen der Physik*, vol. 527, no. 1-2, pp. 27–44, 2015.

[19] C. N. Lau, W. Bao, and J. Velasco Jr, "Properties of suspended graphene membranes," *Materials Today*, vol. 15, no. 6, pp. 238–245, 2012.

[20] A. A. Balandin, S. Ghosh, W. Bao, I. Calizo, D. Teweldebrhan, F. Miao, and C. N. Lau, "Superior thermal conductivity of single-layer graphene," *Nano letters*, vol. 8, no. 3, pp. 902–907, 2008.

[21] S.-E. Zhu, R. Shabani, J. Rho, Y. Kim, B. H. Hong, J.-H. Ahn, and H. J. Cho, "Graphene-based bimorph microactuators," *Nano letters*, vol. 11, no. 3, pp. 977–981, 2011.

[22] F. Ye, J. Lee, and P. X.-L. Feng, "Electrothermally tunable graphene resonators operating at very high temperature up to 1200 k," *Nano letters*, vol. 18, no. 3, pp. 1678–1685, 2018.

[23] A. C. Neto, F. Guinea, N. M. Peres, K. S. Novoselov, and A. K. Geim, "The electronic properties of graphene," *Reviews of modern physics*, vol. 81, no. 1, p. 109, 2009.

[24] P. R. Wallace, "The band theory of graphite," *Physical review*, vol. 71, no. 9, p. 622, 1947.

[25] J.-C. Charlier, X. Blase, and S. Roche, "Electronic and transport properties of nanotubes," *Reviews of modern physics*, vol. 79, no. 2, p. 677, 2007.

[26] S. Reich, J. Maultzsch, C. Thomsen, and P. Ordejon, "Tight-binding description of graphene," *Physical Review B*, vol. 66, no. 3, p. 035412, 2002.

[27] C. Martín, K. Kostarelos, M. Prato, and A. Bianco, "Biocompatibility and biodegradability of 2d materials: graphene and beyond," *Chemical Communications*, vol. 55, no. 39, pp. 5540–5546, 2019.

[28] A. M. Pinto, I. C. Goncalves, and F. D. Magalhaes, "Graphene-based materials biocompatibility: A review," *Colloids and Surfaces B: Biointerfaces*, vol. 111, pp. 188–202, 2013.

[29] A. Sasidharan, L. S. Panchakarla, A. R. Sadanandan, A. Ashokan, P. Chandran, C. M. Girish, D. Menon, S. V. Nair, C. Rao, and M. Koyakutty, "Hemocompatibility and macrophage response of pristine and functionalized graphene," *Small*, vol. 8, no. 8, pp. 1251–1263, 2012.

[30] N. P. Pampaloni, M. Lottner, M. Giugliano, A. Matruglio, F. D'Amico, M. Prato, J. A. Garrido, L. Ballerini, and D. Scaini, "Single-layer graphene modulates neuronal communication and augments membrane ion currents," *Nature nanotechnology*, vol. 13, no. 8, pp. 755–764, 2018.

[31] J. Park, S. Park, S. Ryu, S. H. Bhang, J. Kim, J.-K. Yoon, Y. H. Park, S.-P. Cho, S. Lee, B. H. Hong *et al.*, "Graphene–regulated cardiomyogenic differentiation process of mesenchymal stem cells by enhancing the expression of extracellular matrix proteins and cell signaling molecules," *Advanced healthcare materials*, vol. 3, no. 2, pp. 176–181, 2014.

[32] L. Fusco, M. Garrido, C. Martín, S. Sosa, C. Ponti, A. Centeno, B. Alonso, A. Zurutuza, E. Vázquez, A. Tubaro *et al.*, "Skin irritation potential of

graphene-based materials using a non-animal test," *Nanoscale*, vol. 12, no. 2, pp. 610–622, 2020.

[33] M. Xu, J. Zhu, F. Wang, Y. Xiong, Y. Wu, Q. Wang, J. Weng, Z. Zhang, W. Chen, and S. Liu, "Improved in vitro and in vivo biocompatibility of graphene oxide through surface modification: poly (acrylic acid)-functionalization is superior to pegylation," *Acs Nano*, vol. 10, no. 3, pp. 3267–3281, 2016.

[34] J. P. Mutschlecner and R. W. Whitaker, "Infrasound from earthquakes," *Journal of Geophysical Research: Atmospheres*, vol. 110, no. D1, 2005.

[35] J. B. Johnson and M. Ripepe, "Volcano infrasound: A review," *Journal of Volcanology and Geothermal Research*, vol. 206, no. 3-4, pp. 61–69, 2011.

[36] D. O. ReVelle, "On meteor-generated infrasound," *Journal of Geophysical Research*, vol. 81, no. 7, pp. 1217–1230, 1976.

[37] Y. Ning, A. Mitchell, and R. Tait, "Fabrication of a silicon micromachined capacitive microphone using a dry-etch process," *Sensors and Actuators A: Physical*, vol. 53, no. 1-3, pp. 237–242, 1996.

[38] A. Torkkeli, O. Rusanen, J. Saarilahti, H. Seppä, H. Sipola, and J. Hietanen, "Capacitive microphone with low-stress polysilicon membrane and high-stress polysilicon backplate," *Sensors and Actuators A: Physical*, vol. 85, no. 1-3, pp. 116–123, 2000.

[39] B. A. Ganji and B. Y. Majlis, "Design and fabrication of a new mems capacitive microphone using a perforated aluminum diaphragm," *Sensors and Actuators A: Physical*, vol. 149, no. 1, pp. 29–37, 2009.

[40] F. Stoppel, A. Männchen, F. Niekiel, D. Beer, T. Giese, and B. Wagner, "New integrated full-range mems speaker for in-ear applications," in *2018 IEEE Micro Electro Mechanical Systems (MEMS)*. IEEE, 2018, pp. 1068–1071.

[41] I.-J. Cho, S. Jang, and H.-J. Nam, "A piezoelectrically actuated mems speaker with polyimide membrane and thin film pb (zr, ti) o3 (pzt) actuator," *Integrated Ferroelectrics*, vol. 105, no. 1, pp. 27–36, 2009.

[42] M. J. Wittbrodt, C. R. Steele, and S. Puria, "Developing a physical model of the human cochlea using microfabrication methods," *Audiology and Neurotology*, vol. 11, no. 2, pp. 104–112, 2006.

[43] W. Si, C. Fu, D. Li, H. Li, P. Yuan, and Y. Yu, "Directional sensitivity of a mems-based fiber-optic extrinsic fabry–perot ultrasonic sensor for partial discharge detection," *Sensors*, vol. 18, no. 6, p. 1975, 2018.

[44] I. G. Mina, H. Kim, I. Kim, S. K. Park, K. Choi, T. N. Jackson, R. L. Tutwiler, and S. Trolier-McKinstry, "High frequency piezoelectric mems ultrasound transducers," *IEEE Transactions on Ultrasonics, Ferroelectrics, and Frequency Control*, vol. 54, no. 12, pp. 2422–2430, 2007.

[45] M. A. Shah, I. A. Shah, D.-G. Lee, and S. Hur, "Design approaches of mems microphones for enhanced performance," *Journal of Sensors*, vol. 2019, 2019.

[46] S.-C. Lo, W.-C. Lai, C.-I. Chang, Y.-Y. Lo, C. Wang, M. R. Bai, and W. Fang, "Development of a no-back-plate soi mems condenser microphone," in *2015 Transducers-2015 18th International Conference on Solid-State Sensors, Actuators and Microsystems (Transducers)*. IEEE, 2015, pp. 1085–1088.

[47] A. Rahaman, A. Ishfaque, H. Jung, and B. Kim, "Bio-inspired rectangular shaped piezoelectric mems directional microphone," *IEEE Sensors Journal*, vol. 19, no. 1, pp. 88–96, 2018.

[48] Y. Zhang, R. Bauer, J. C. Jackson, W. M. Whitmer, J. F. Windmill, and D. Uttamchandani, "A low-frequency dual-band operational microphone

mimicking the hearing property of ormia ochracea," *Journal of Microelectromechanical Systems*, vol. 27, no. 4, pp. 667–676, 2018.

[49] Y. Wu, C. Yu, F. Wu, C. Li, J. Zhou, Y. Gong, Y. Rao, and Y. Chen, "A highly sensitive fiber-optic microphone based on graphene oxide membrane," *Journal of Lightwave Technology*, vol. 35, no. 19, pp. 4344–4349, 2017.

[50] W. Kronast, B. Müller, W. Siedel, and A. Stoffel, "Single-chip condenser microphone using porous silicon as sacrificial layer for the air gap," *Sensors and Actuators A: Physical*, vol. 87, no. 3, pp. 188–193, 2001.

[51] P. Rombach, M. Müllenborn, U. Klein, and K. Rasmussen, "The first low voltage, low noise differential silicon microphone, technology development and measurement results," *Sensors and actuators A: Physical*, vol. 95, no. 2-3, pp. 196–201, 2002.

[52] N. A. Hall, *Electrostatic MEMS Microphones.* Dordrecht: Springer Netherlands, 2016, pp. 1108–1117. [Online]. Available: https://doi.org/10.1007/978-94-017-9780-1_317

[53] S. Mallik, D. Chowdhury, and M. Chttopadhyay, "Development and performance analysis of a low-cost mems microphone-based hearing aid with three different audio amplifiers," *Innovations in Systems and Software Engineering*, vol. 15, no. 1, pp. 17–25, 2019.

[54] L. Sant, R. Gaggl, E. Bach, C. Buffa, N. De Milleri, D. Sträussnigg, and A. Wiesbauer, "Mems microphones: Concept and design for mobile applications," in *Low-Power Analog Techniques, Sensors for Mobile Devices, and Energy Efficient Amplifiers.* Cham: Springer International Publishing, 2019, pp. 155–174.

[55] A. Dehé, "Silicon microphone development and application," *Sensors and Actuators A: Physical*, vol. 133, no. 2, pp. 283–287, 2007, selected Papers from the 9th International Conference on Materials for Advanced

Technologies. [Online]. Available: https://www.sciencedirect.com/science/article/pii/S0924424706004171

[56] K. S. Novoselov, A. K. Geim, S. V. Morozov, D. Jiang, Y. Zhang, S. V. Dubonos, I. V. Grigorieva, and A. A. Firsov, "Electric field effect in atomically thin carbon films," *science*, vol. 306, no. 5696, pp. 666–669, 2004.

[57] P. Avouris and C. Dimitrakopoulos, "Graphene: synthesis and applications," *Materials today*, vol. 15, no. 3, pp. 86–97, 2012.

[58] P. N. First, W. A. de Heer, T. Seyller, C. Berger, J. A. Stroscio, and J.-S. Moon, "Epitaxial graphenes on silicon carbide," *MRS bulletin*, vol. 35, no. 4, pp. 296–305, 2010.

[59] K. S. Kim, Y. Zhao, H. Jang, S. Y. Lee, J. M. Kim, K. S. Kim, J.-H. Ahn, P. Kim, J.-Y. Choi, and B. H. Hong, "Large-scale pattern growth of graphene films for stretchable transparent electrodes," *nature*, vol. 457, no. 7230, pp. 706–710, 2009.

[60] A. Reina, X. Jia, J. Ho, D. Nezich, H. Son, V. Bulovic, M. S. Dresselhaus, and J. Kong, "Large area, few-layer graphene films on arbitrary substrates by chemical vapor deposition," *Nano letters*, vol. 9, no. 1, pp. 30–35, 2009.

[61] X. Li, W. Cai, J. An, S. Kim, J. Nah, D. Yang, R. Piner, A. Velamakanni, I. Jung, E. Tutuc *et al.*, "Large-area synthesis of high-quality and uniform graphene films on copper foils," *science*, vol. 324, no. 5932, pp. 1312–1314, 2009.

[62] J. Kang, D. Shin, S. Bae, and B. H. Hong, "Graphene transfer: Key for applications," *Nanoscale*, vol. 4, no. 18, pp. 5527–5537, 2012.

[63] S. Unarunotai, Y. Murata, C. E. Chialvo, H.-s. Kim, S. MacLaren, N. Mason, I. Petrov, and J. A. Rogers, "Transfer of graphene layers grown on sic wafers to other substrates and their integration into field effect transistors," *Applied Physics Letters*, vol. 95, no. 20, p. 202101, 2009.

[64] S. Unarunotai, J. C. Koepke, C.-L. Tsai, F. Du, C. E. Chialvo, Y. Murata, R. Haasch, I. Petrov, N. Mason, M. Shim *et al.*, “Layer-by-layer transfer of multiple, large area sheets of graphene grown in multilayer stacks on a single sic wafer,” *ACS nano*, vol. 4, no. 10, pp. 5591–5598, 2010.

[65] J. D. Caldwell, T. J. Anderson, J. C. Culbertson, G. G. Jernigan, K. D. Hobart, F. J. Kub, M. J. Tadjer, J. L. Tedesco, J. K. Hite, M. A. Mastro *et al.*, “Technique for the dry transfer of epitaxial graphene onto arbitrary substrates,” *ACS nano*, vol. 4, no. 2, pp. 1108–1114, 2010.

[66] J. W. Suk, A. Kitt, C. W. Magnuson, Y. Hao, S. Ahmed, J. An, A. K. Swan, B. B. Goldberg, and R. S. Ruoff, “Transfer of cvd-grown monolayer graphene onto arbitrary substrates,” *ACS nano*, vol. 5, no. 9, pp. 6916–6924, 2011.

[67] K. Takahashi, H. Ishida, and K. Sawada, “Vacuum-sealed microcavity formed from suspended graphene by using a low-pressure dry-transfer technique,” *Applied Physics Letters*, vol. 112, no. 4, p. 041901, 2018.

[68] P. Vandenabeele, *Practical Raman spectroscopy : an introduction*, ser. Analytical techniques in the sciences. Chichester, West Sussex, United Kingdom: Wiley, 2013.

[69] A. C. Ferrari, J. C. Meyer, V. Scardaci, C. Casiraghi, M. Lazzeri, F. Mauri, S. Piscanec, D. Jiang, K. S. Novoselov, S. Roth, and A. K. Geim, “Raman Spectrum of Graphene and Graphene Layers,” vol. 187401, no. NOVEMBER, pp. 1–4, 2006.

[70] F. Tuinstra and J. L. Koenig, “Raman spectrum of graphite,” *The Journal of chemical physics*, vol. 53, no. 3, pp. 1126–1130, 1970.

[71] M. Wall, “The raman spectroscopy of graphene and the determination of layer thickness. thermo scientific application note: 52252,” 2011.

[72] S. Rolt, “Optical engineering science,” 2020.

[73] W. Bauer, M. Weber, and S. Chanbai, “White light interferometry,” in *Encyclopedia of Tribology.* Boston, MA: Springer US, pp. 4115–4127.

[74] J. C. Wyant, “White light interferometry,” in *Holography: A Tribute to Yuri Denisyuk and Emmett Leith*, vol. 4737. International Society for Optics and Photonics, 2002, pp. 98–107.

[75] R. W. Johnson, *Handbook of fluid dynamics.* Crc Press, 2016.

[76] A. Boutier, *Laser velocimetry in fluid mechanics.* John Wiley & Sons, 2013.

[77] P. M. Doran, “Chapter 7 - fluid flow,” in *Bioprocess Engineering Principles (Second Edition)*, second edition ed., P. M. Doran, Ed. London: Academic Press, 2013, pp. 201–254. [Online]. Available: https://www.sciencedirect.com/science/article/pii/B9780122208515000071

[78] L. E. Drain, “The laser doppler techniques,” *Chichester*, 1980.

[79] D. L. Logan, *A first course in the finite element method.* Cengage Learning, 2016.

[80] Z. Bi, “Chapter 8 - applications—solid mechanics problems,” in *Finite Element Analysis Applications*, Z. Bi, Ed. Academic Press, 2018, pp. 281–339. [Online]. Available: https://www.sciencedirect.com/science/article/pii/B978012809952000008X

[81] U. Ali, K. J. B. A. Karim, and N. A. Buang, “A review of the properties and applications of poly (methyl methacrylate)(pmma),” *Polymer Reviews*, vol. 55, no. 4, pp. 678–705, 2015.

[82] G. Gui, J. Li, and J. Zhong, “Band structure engineering of graphene by strain: First-principles calculations,” *Physical Review B*, vol. 78, no. 7, p. 075435, 2008.

[83] A. K. Al-Mashaal, G. S. Wood, A. Torin, E. Mastropaolo, M. J. Newton, and R. Cheung, "Tunable graphene-polymer resonators for audio frequency sensing applications," *IEEE Sensors Journal*, vol. 19, no. 2, pp. 465–473, 2019.

[84] K. S. Novoselov, A. K. Geim, S. V. Morozov, D. Jiang, Y. Zhang, S. V. Dubonos, I. V. Grigorieva, and A. A. Firsov, "Electric field effect in atomically thin carbon films," *Science*, vol. 306, no. 5696, pp. 666–9, 2004. [Online]. Available: https://www.ncbi.nlm.nih.gov/pubmed/15499015

[85] C. Changyao and J. Hone, "Graphene nanoelectromechanical systems," *Proceedings of the IEEE*, vol. 101, no. 7, pp. 1766–1779, 2013.

[86] R. De Alba, F. Massel, I. R. Storch, T. S. Abhilash, A. Hui, P. L. McEuen, H. G. Craighead, and J. M. Parpia, "Tunable phonon-cavity coupling in graphene membranes," *Nat Nanotechnol*, vol. 11, no. 9, pp. 741–6, 2016. [Online]. Available: https://www.ncbi.nlm.nih.gov/pubmed/27294504

[87] D. Todorović, A. Matković, M. Milićević, D. Jovanović, R. Gajić, I. Salom, and M. Spasenović, "Multilayer graphene condenser microphone," *2D Materials*, vol. 2, no. 4, p. 045013, 2015.

[88] S. Woo, J. H. Han, J. H. Lee, S. Cho, K. W. Seong, M. Choi, and J. H. Cho, "Realization of a high sensitivity microphone for a hearing aid using a graphene-pmma laminated diaphragm," *ACS Appl Mater Interfaces*, vol. 9, no. 2, pp. 1237–1246, 2017. [Online]. Available: https://www.ncbi.nlm.nih.gov/pubmed/28055184

[89] G. S. Wood, A. Torin, A. K. Al-mashaal, L. S. Smith, E. Mastropaolo, M. J. Newton, and R. Cheung, "Design and characterization of a micro-fabricated graphene-based mems microphone," *IEEE Sensors Journal*, 2019.

[90] Q. Zhou, J. Zheng, S. Onishi, M. Crommie, and A. K. Zettl, "Graphene electrostatic microphone and ultrasonic radio," *Proceedings of the National*

Academy of Sciences, vol. 112, no. 29, pp. 8942–8946, 2015.

[91] C. Lee, X. Wei, J. W. Kysar, and J. Hone, "Measurement of the elastic properties and intrinsic strength of monolayer graphene," *Science*, vol. 321, no. 5887, pp. 385–8, 2008. [Online]. Available: https://www.ncbi.nlm.nih.gov/pubmed/18635798

[92] K. I. Bolotin, K. J. Sikes, Z. Jiang, M. Klima, G. Fudenberg, J. Hone, P. Kim, and H. L. Stormer, "Ultrahigh electron mobility in suspended graphene," *Solid State Communications*, vol. 146, no. 9-10, pp. 351–355, 2008.

[93] G. J. Verbiest, J. N. Kirchhof, J. Sonntag, M. Goldsche, T. Khodkov, and C. Stampfer, "Detecting ultrasound vibrations with graphene resonators," *Nano Lett*, vol. 18, no. 8, pp. 5132–5137, 2018. [Online]. Available: https://www.ncbi.nlm.nih.gov/pubmed/29989827

[94] J. Ophir and N. F. Maklad, "Digital scan converters in diagnostic ultrasound imaging," *Proceedings of the IEEE*, vol. 67, no. 4, pp. 654–664, 1979. [Online]. Available: https://dx.doi.org/10.1109/proc.1979.11289

[95] B. W. Drinkwater and P. D. Wilcox, "Ultrasonic arrays for non-destructive evaluation: A review," *NDT & E International*, vol. 39, no. 7, pp. 525–541, 2006.

[96] J. Green, R. E., "Non-contact ultrasonic techniques," *Ultrasonics*, vol. 42, no. 1-9, pp. 9–16, 2004. [Online]. Available: https://www.ncbi.nlm.nih.gov/pubmed/15047255

[97] H. Hong, W. Yongtian, and Y. Dayuan, "A low-cost dynamic range-finding device based on amplitude-modulated continuous ultrasonic wave," *IEEE Transactions on Instrumentation and Measurement*, vol. 51, no. 2, pp. 362–367, 2002. [Online]. Available: https://dx.doi.org/10.1109/19.997838

[98] A. V. Alexandrov, "Ultrasound identification and lysis of clots," *Stroke*, vol. 35, no. 11 Suppl 1, pp. 2722–5, 2004. [Online]. Available: https://www.ncbi.nlm.nih.gov/pubmed/15375301

[99] J. S. Bunch, A. M. Van Der Zande, S. S. Verbridge, I. W. Frank, D. M. Tanenbaum, J. M. Parpia, H. G. Craighead, and P. L. McEuen, "Electromechanical resonators from graphene sheets," *Science*, vol. 315, no. 5811, pp. 490–493, 2007.

[100] T. Chen, E. Mastropaolo, A. Bunting, and R. Cheung, "Observation of second flexural mode enhancement in graphene resonators," *Electronics Letters*, vol. 51, no. 13, pp. 1014–1016, 2015.

[101] D. Davidovikj, M. Poot, S. J. Cartamil-Bueno, H. S. J. Van Der Zant, and P. G. Steeneken, "On-chip heaters for tension tuning of graphene nanodrums," *Nano Letters*, vol. 18, no. 5, pp. 2852–2858, 2018.

[102] D. Garcia-Sanchez, A. M. van der Zande, A. S. Paulo, B. Lassagne, P. L. McEuen, and A. Bachtold, "Imaging mechanical vibrations in suspended graphene sheets," *Nano Lett*, vol. 8, no. 5, pp. 1399–403, 2008. [Online]. Available: https://www.ncbi.nlm.nih.gov/pubmed/18402478

[103] S. Lee, C. Chen, V. V. Deshpande, G.-H. Lee, I. Lee, M. Lekas, A. Gondarenko, Y.-J. Yu, K. Shepard, P. Kim *et al.*, "Electrically integrated su-8 clamped graphene drum resonators for strain engineering," *Applied Physics Letters*, vol. 102, no. 15, p. 153101, 2013.

[104] R. Singh, R. J. Nicholl, K. I. Bolotin, and S. Ghosh, "Motion transduction with thermo-mechanically squeezed graphene resonator modes," *Nano letters*, vol. 18, no. 11, pp. 6719–6724, 2018.

[105] A. Al-mashaal, G. Wood, A. Torin, E. Mastropaolo, M. Newton, and R. Cheung, "Dynamic behavior of ultra large graphene-based membranes

using electrothermal transduction," *Applied Physics Letters*, vol. 111, no. 24, p. 243503, 2017.

[106] L. E. Kinsler, A. R. Frey, A. B. Coppens, and J. V. Sanders, *Fundamentals of acoustics*. John wiley & sons, 2000.

[107] M. Karnezos, "Effects of stress on the stability of x-ray masks," *Journal of Vacuum Science & Technology B: Microelectronics and Nanometer Structures*, vol. 4, no. 1, p. 226, 1986. [Online]. Available: https://dx.doi.org/10.1116/1.583444

[108] D. Yoon, Y. W. Son, and H. Cheong, "Negative thermal expansion coefficient of graphene measured by raman spectroscopy," *Nano Lett*, vol. 11, no. 8, pp. 3227–31, 2011. [Online]. Available: https://www.ncbi.nlm.nih.gov/pubmed/21728349

[109] S. Schmid, L. G. Villanueva, and M. L. Roukes, *Quality Factor*, 2016, book section Chapter 2, pp. 57–90.

[110] C. Wong, M. Annamalai, Z. Wang, and M. Palaniapan, "Characterization of nanomechanical graphene drum structures," *Journal of Micromechanics and Microengineering*, vol. 20, no. 11, p. 115029, 2010.

[111] P. Weber, J. Guttinger, I. Tsioutsios, D. E. Chang, and A. Bachtold, "Coupling graphene mechanical resonators to superconducting microwave cavities," *Nano letters*, vol. 14, no. 5, pp. 2854–2860, 2014.

[112] J. P. Mathew, R. N. Patel, A. Borah, R. Vijay, and M. M. Deshmukh, "Dynamical strong coupling and parametric amplification of mechanical modes of graphene drums," *Nature nanotechnology*, vol. 11, no. 9, p. 747, 2016.

[113] R. J. Dolleman, D. Davidovikj, S. J. Cartamil-Bueno, H. S. van der Zant, and P. G. Steeneken, "Graphene squeeze-film pressure sensors," *Nano letters*, vol. 16, no. 1, pp. 568–571, 2016.

[114] S. Woo, J.-H. Han, J. H. Lee, S. Cho, K.-W. Seong, M. Choi, and J.-H. Cho, “Realization of a high sensitivity microphone for a hearing aid using a graphene–pmma laminated diaphragm,” *ACS applied materials & interfaces*, vol. 9, no. 2, pp. 1237–1246, 2017.

[115] Q. Zhou and A. Zettl, “Electrostatic graphene loudspeaker,” *Applied Physics Letters*, vol. 102, no. 22, p. 223109, 2013.

[116] L. Que, J.-S. Park, and Y. Gianchandani, “Bent-beam electro-thermal actuators for high force applications,” in *Technical Digest. IEEE International MEMS 99 Conference. Twelfth IEEE International Conference on Micro Electro Mechanical Systems (Cat. No. 99CH36291).* IEEE, 1999, pp. 31–36.

[117] N.-T. Nguyen, S.-S. Ho, and C. L.-N. Low, “A polymeric microgripper with integrated thermal actuators,” *Journal of Micromechanics and Microengineering*, vol. 14, no. 7, p. 969, 2004.

[118] J. S. Bunch, S. S. Verbridge, J. S. Alden, A. M. Van Der Zande, J. M. Parpia, H. G. Craighead, and P. L. McEuen, “Impermeable atomic membranes from graphene sheets,” *Nano letters*, vol. 8, no. 8, pp. 2458–2462, 2008.

[119] Y. Zhou and F. Amirouche, “Study of fluid damping effects on resonant frequency of an electromagnetically actuated valveless micropump,” *The International Journal of Advanced Manufacturing Technology*, vol. 45, no. 11-12, p. 1187, 2009.

[120] A. C. Ferrari, J. Meyer, V. Scardaci, C. Casiraghi, M. Lazzeri, F. Mauri, S. Piscanec, D. Jiang, K. Novoselov, S. Roth *et al.*, “Raman spectrum of graphene and graphene layers,” *Physical review letters*, vol. 97, no. 18, p. 187401, 2006.

[121] A. C. Ferrari, “Raman spectroscopy of graphene and graphite: disorder,

electron–phonon coupling, doping and nonadiabatic effects," *Solid state communications*, vol. 143, no. 1-2, pp. 47–57, 2007.

[122] A. C. Ferrari and J. Robertson, "Interpretation of raman spectra of disordered and amorphous carbon," *Physical review B*, vol. 61, no. 20, p. 14095, 2000.

[123] C. Metzger, S. Rémi, M. Liu, S. V. Kusminskiy, A. H. Castro Neto, A. K. Swan, and B. B. Goldberg, "Biaxial strain in graphene adhered to shallow depressions," *Nano letters*, vol. 10, no. 1, pp. 6–10, 2009.

[124] J. Xu, G. S. Wood, A. K. Al-mashaal, E. Mastropaolo, M. J. Newton, and R. Cheung, "Realization of closed cavity resonator formed by graphene-pmma membrane for sensing audio frequency," *IEEE Sensors Journal*, vol. 20, no. 9, pp. 4618–4627, 2020.

[125] W. Y. Fung, E. N. Dattoli, and W. Lu, "Radio frequency nanowire resonators and in situ frequency tuning," *Applied Physics Letters*, vol. 94, no. 20, 2009.

[126] I. Kozinsky, H. W. C. Postma, I. Bargatin, and M. L. Roukes, "Tuning nonlinearity, dynamic range, and frequency of nanomechanical resonators," *Applied Physics Letters*, vol. 88, no. 25, 2006.

[127] C. C. Wu and Z. Zhong, "Capacitive spring softening in single-walled carbon nanotube nanoelectromechanical resonators," *Nano Lett*, vol. 11, no. 4, pp. 1448–51, 2011. [Online]. Available: https://www.ncbi.nlm.nih.gov/pubmed/21428322

[128] K. Chen and K. S. Schweizer, "Theory of yielding, strain softening, and steady plastic flow in polymer glasses under constant strain rate deformation," *Macromolecules*, vol. 44, no. 10, pp. 3988–4000, 2011.

[129] C. N. Lau, W. Bao, and J. Velasco, "Properties of suspended graphene membranes," *Materials Today*, vol. 15, no. 6, pp. 238–245, 2012.

[130] J. Lee, Z. Wang, K. He, J. Shan, and P. X.-L. Feng, "High frequency mos2 nanomechanical resonators," *ACS Nano*, vol. 7, no. 7, pp. 6086–6091, 2013, pMID: 23738924. [Online]. Available: https://doi.org/10.1021/nn4018872

[131] Y. Jinling, T. Ono, and M. Esashi, "Energy dissipation in submicrometer thick single-crystal silicon cantilevers," *Journal of Microelectromechanical Systems*, vol. 11, no. 6, pp. 775–783, 2002.

[132] J. S. Bunch, S. S. Verbridge, J. S. Alden, A. M. van der Zande, J. M. Parpia, H. G. Craighead, and P. L. McEuen, "Impermeable atomic membranes from graphene sheets," *Nano Lett*, vol. 8, no. 8, pp. 2458–62, 2008. [Online]. Available: https://www.ncbi.nlm.nih.gov/pubmed/18630972

[133] A. F. Carvalho, A. J. Fernandes, M. B. Hassine, P. Ferreira, E. Fortunato, and F. M. Costa, "Millimeter-sized few-layer suspended graphene membranes," *Applied Materials Today*, vol. 21, p. 100879, 2020.

[134] J. Bergqvist and J. Gobet, "Capacitive microphone with a surface micromachined backplate using electroplating technology," *Journal of Microelectromechanical Systems*, vol. 3, no. 2, pp. 69–75, 1994.

[135] P. Li, Z. You, and T. Cui, "Graphene cantilever beams for nano switches," *Applied Physics Letters*, vol. 101, no. 9, p. 093111, 2012.

[136] A. Eichler, J. Moser, J. Chaste, M. Zdrojek, I. Wilson-Rae, and A. Bachtold, "Nonlinear damping in mechanical resonators made from carbon nanotubes and graphene," *Nature nanotechnology*, vol. 6, no. 6, pp. 339–342, 2011.

[137] C. Chen, S. Rosenblatt, K. I. Bolotin, W. Kalb, P. Kim, I. Kymissis, H. L. Stormer, T. F. Heinz, and J. Hone, "Performance of monolayer graphene nanomechanical resonators with electrical readout," *Nature nanotechnology*, vol. 4, no. 12, pp. 861–867, 2009.

[138] V. Singh, S. Sengupta, H. S. Solanki, R. Dhall, A. Allain, S. Dhara, P. Pant, and M. M. Deshmukh, "Probing thermal expansion of graphene and

modal dispersion at low-temperature using graphene nanoelectromechanical systems resonators," *Nanotechnology*, vol. 21, no. 16, p. 165204, 2010.

[139] K. Chen, E. Saltzman, and K. S. Schweizer, "Segmental dynamics in polymers: from cold melts to ageing and stressed glasses," *Journal of Physics: Condensed Matter*, vol. 21, no. 50, p. 503101, 2009.

[140] K. Ogata, *Modern control engineering.* Prentice hall, 2010.

[141] H. Willis, V. Zichy, and P. Hendra, "The laser-raman and infra-red spectra of poly (methyl methacrylate)," *Polymer*, vol. 10, pp. 737–746, 1969.

[142] P. McMillan, "Structural Studies of Silicate Glasses and Melts - Applications and Limitations of Raman Spectroscopy." *American Mineralogist*, vol. 69, no. 6-8, pp. 622–644, 1984.

[143] J. Xu, G. S. Wood, E. Mastropaolo, M. J. Newton, and R. Cheung, "Realization of a graphene/pmma acoustic capacitive sensor released by silicon dioxide sacrificial layer," *ACS Appl Mater Interfaces*, vol. 13, no. 32, pp. 38 792–38 798, 2021. [Online]. Available: https://www.ncbi.nlm.nih.gov/pubmed/34337933

[144] V. Sazonova, Y. Yaish, H. Üstünel, D. Roundy, T. A. Arias, and P. L. McEuen, "A tunable carbon nanotube electromechanical oscillator," *Nature*, vol. 431, no. 7006, pp. 284–287, 2004. [Online]. Available: https://dx.doi.org/10.1038/nature02905

[145] C. W. De Silva, *Vibration damping, control, and design.* CRC Press, 2007.

rolt2020optical

Appendix A

Graphene/PMMA open cavity ultrasonic resonator

The frequency response of the substrate on the open cavity resonator mechanically actuated by 1 V AC and 1 V DC has been illustrated in Figure A.1. The absence of resonant frequency response on the substrate shows the frequency response observed in Figure 3.3.a has been corresponded to the graphene/PMMA membrane.

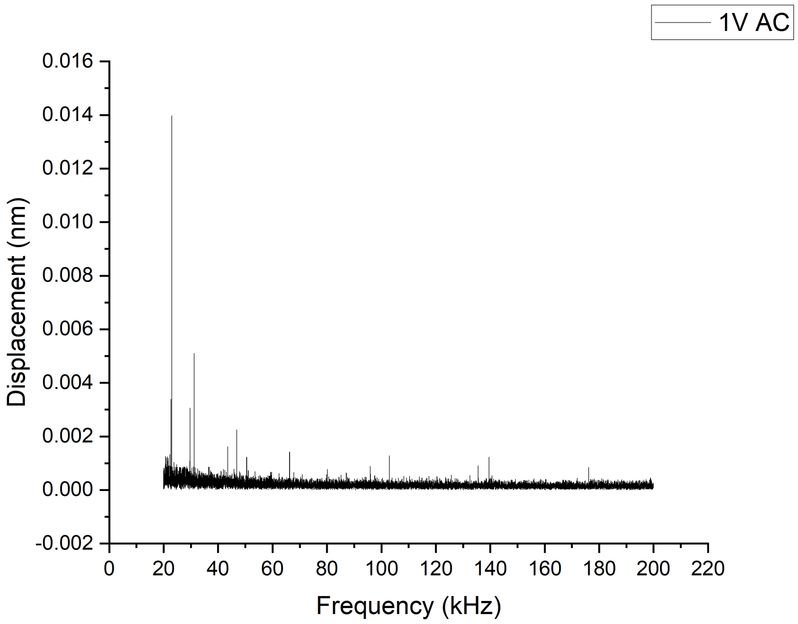

(a)

Figure A.1: The frequency response of the substrate under the mechanical actuation (1 V AC, 1 V DC).

Appendix B

Graphene/PMMA closed cavity resonator for ultrasound sensing

By applying 1 V AC and 1 V DC to the piezo-disk, the vibration has been observed at the substrate where the graphene/PMMA membrane has been attached, as shown in Figure S 1.1. The resonant frequency has been measured to be 169.877 kHz. The displacement has been observed to be around 0.061 nm. The vibration amplitude measured at suspended graphene/PMMA membrane has been 0.486 nm at the frequency of around 169.446 kHz (Figure 3.a). At the side band frequency (around 169 kHz), the displacement measured at the substrate has been estimated to be around 12.6 % of the vibration amplitude measured at the suspended membrane.

As the mode shape shown in Figure S 1.2, transition between the (1,1) the (0,2) has been observed at the frequency of 189.162 kHz, which could be the reason for the side band shown in around 188 kHz at Figure 3.c.

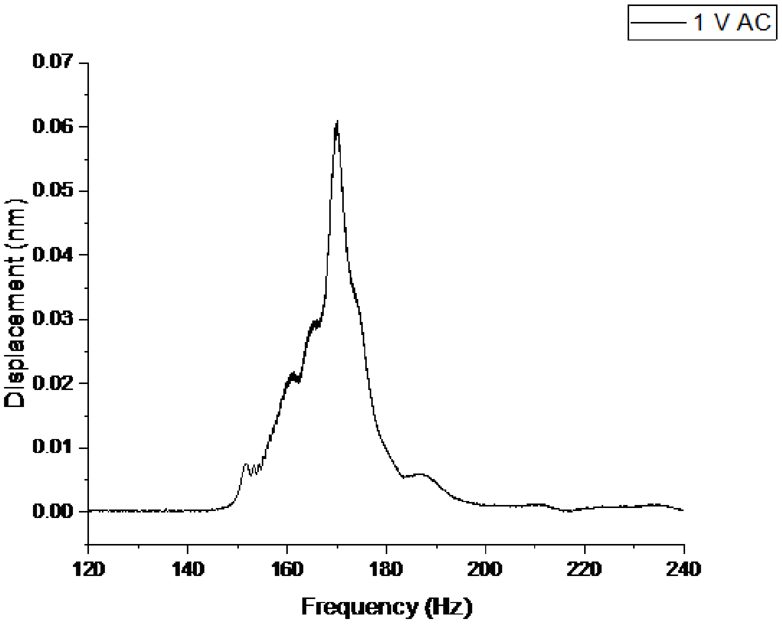

(a)

Figure B.1: The frequency response of the resonator$'s$ substrate under the mechanical actuation with the 1 V AC and 1 V DC.

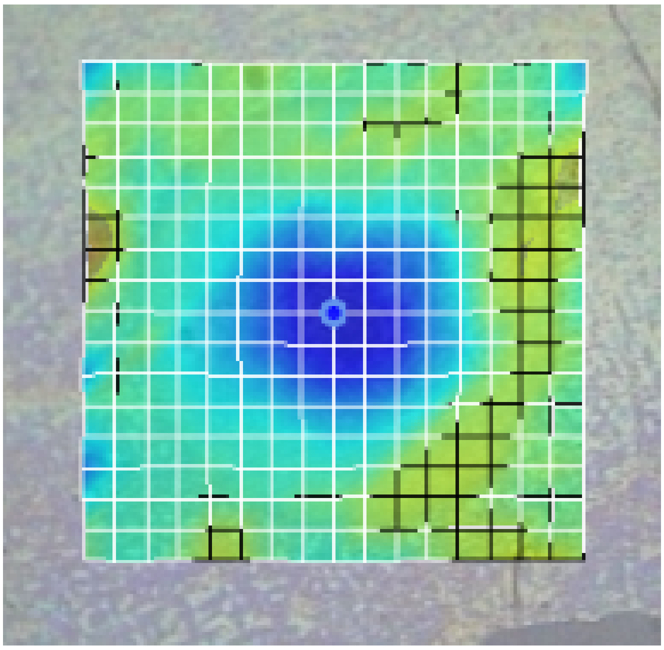

(a)

Figure B.2: The mode shape of the graphene/PMMA ultrasonic resonator at the frequency of 189.162 kHz and with the electro-thermal actuation at the 3 V AC and 1V DC.

Appendix C

Publications

Jing Xu, Graham S. Wood, Asaad, K Al-Mashaal, Enrico Mastropaolo, Michael Newton and Rebecca Cheung ”Realization of Closed Cavity Resonator Formed by Graphene-PMMA Membrane for Sensing Audio Frequency”, IEEE Sensors Journal, 13th Jan., 2020. (DOI:10.1109/JSEN.2020.2966415)

Jing Xu, Graham. S. Wood, Enrico Mastropaolo, Michael. J. Newton, and Rebecca Cheung ACS Applied Materials & Interfaces 2021 13 (32), 38792-3879 (DOI: 10.1021/acsami.1c05424)